
Brightness characterization of single core
and core/shell $\text{Yb}^{3+}, \text{Er}^{3+}$ -doped NaYF_4
upconversion nanoparticles

&

Design and realization of a CW-STED
super-resolution microscope setup

MASTER'S THESIS APPLIED PHYSICS

Author:

Remko R. M. Dijkstra

Supervisors

Niels Zijlstra, MSc
Dr. Christian Blum

OCTOBER 11, 2012

Nanobiophysics Group
Faculty of Science Technology

UNIVERSITY OF TWENTE.

Graduation committee:

prof. dr. Vinod Subramaniam (NBP)

prof. dr. Klaus Boller (LPNO)

dr. Christian Blum (NBP)

Niels Zijlstra, MSc (NBP)

Corresponding address:

Nanobiophysics Group

University of Twente

PO Box 217

7500AE Enschede

The Netherlands

**Part of the research was in
collaboration with:**

Anorganische Chemie I

Universität Osnabrück

Barbarastraße 7

D-49069, Osnabrück

Germany

*“I don’t know anything, but I do know that everything
is interesting if you go into it deeply enough.”*

RICHARD P. FEYNMAN (1918-1988)

Abstract

Part I: Upconversion Nanoparticles

$\text{NaYF}_4:\text{Yb}^{3+}, \text{Er}^{3+}$ upconversion nanoparticles are luminescent particles that are promising in a wide range of applications such as: biomarkers, solar-cells, displays and microbarcodes [1]. However, due to their small size, these particles are typically not very bright. Coating the particles with a uniform NaYF_4 shell increases the brightness significantly. Interestingly, the brightness continues to increase even after applying very thick shells, but never reaches the brightness of the bulk counterpart. The reason for this is still unknown. The objective of this study is to characterize the brightness of core-only and core/shell particles with different shell thickness on a single particle scale. This study, being the first of its kind, aims for new insights on the reasoning behind the inability of core/shell particles to reach the brightness of the bulk counterpart.

The results of the single particle characterization confirmed an increasing particle brightness with increasing shell thickness. A key observation is the broadening of the single-particle brightness distribution with increasing shell thickness. We attribute this broadening to the presence of dopants in the shell, which are incorporated into the shell during synthesis. This is contrary to the idea of a completely passive shell, which was always assumed. This new insight is important feedback for the materials group that synthesizes the particles. Alternative methods for creating dopant-free shells should be considered.

Additional first experiments on the dependence of excitation power-*vs*-emission intensity showed a significant difference between core-only and core/shell particles, indicating that the shell does play a significant role in the particle brightness enhancement. Preliminary results on the particle emission spectrum showed an interesting additional peak at 700 nm in addition to the spectrum that is typically reported in literature.

Part II: STED Setup Design

The objective of the second part of the assignment was to design and realize an easy-to-use and robust single molecule sensitive microscope setup with additional Stimulated Emission Depletion (STED) super-resolution capability. In this report, the design and initial characterization of this setup is presented.

By imaging single quantum dots it is shown that the realized setup is single-emitter sensitive. Furthermore, we present that a diffraction limited resolution of ~ 280 nm FWHM can be obtained in confocal-mode. For the STED functionality we chose to implement continuous-wave based STED, since this does not require tight laser pulse synchronization. A doughnut-shaped point-spread function (PSF) for the STED beam can be easily obtained in the realized setup. Optimization of the doughnut quality can be efficiently realized with the setup through polarization fine-tuning and spatial phase-adjustment of the STED beam. Furthermore, the realized setup allows easy initial alignment of the excitation PSF maximum with the intensity-null of the STED doughnut PSF to within an accuracy of ~ 100 nm, which can be further improved by fine-tuning. These initial results demonstrate the possibility to obtain STED based super-resolution with the realized microscope setup.

Acknowledgments

Without the help of my colleagues at the Nanobiophysics group, this project would not have been possible. Therefore I would like to thank some people in special that have helped to make this thesis project possible. I will start by thanking prof. dr. Vinod Subramaniam for giving me the possibility to work on these very unique and interesting projects. Many thanks and appreciation goes out to Christian Blum and Niels Zijlstra for their excellent supervision over the two projects I have been working on in the past year. I could always walk in your office to discuss results and problems and you were always glad to help in any way. Also special thanks for the critical reading of this thesis report.

Niels: all the hours we spend on looking into new equipment for the STED setup was very instructive. When I started these projects, I had very little knowledge on experimental optics, but with your help I definitely learned a great deal. I not only learned about the advanced equipment needed and which company has the best mirrors, filters or optomechanical devices, but also how to use them in the lab.

Furthermore I would like to thank my colleague Martijn Stopel in special. Martijn: many thanks for useful discussions in the lab and help with the experimental setup. I learned a great deal about the equipment and experimental optics in general. I have gained much new knowledge about the level of accuracy that is needed for single nanoparticle characterization and thereby gained even more respect for optical studies on this nanoscopic level.

Without critics and discussions, science is not able to progress. Luckily, there were many useful discussions during the weekly meetings and even during coffee breaks in the hallways. Therefore in addition to the already mentioned colleagues I would also like to thank Jord Prangma, Ron Gills, Niek Molenkamp and Robert Molenaar in special for their interesting insights, discussions and help.

To all my housemates at Huize Cornetto: thanks for all the good times! Additionally, a very big thank you goes to study association and fellow students of S.V. Arago and the BACO for all the interactive 'borrels' and activities that were organized and for giving me the opportunity to develop myself besides my study as the BACOning and as president of the Sang Kancil Study Tour 2010 Committee.

Lastly, but not less important, I would like to thank the group of prof. dr. Markus Haase at the University of Osnabrück and Athira Raj in special for synthesizing the upconversion nanoparticles. I hope on the upconversion nanoparticles my work was useful feedback and that you will gain new insights from this work.

Remko Dijkstra
Enschede, October 2012

Thesis outline

This Master's thesis presents the work on two separate projects. For this reason, the report is split up in two separate parts:

Part I: Brightness characterization of single core and core/shell Yb^{3+} , Er^{3+} -doped NaYF_4 upconversion nanoparticles

This part starts with an introduction on upconversion nanoparticles. Next it presents the theoretical background of upconversion, the experimental methods used to characterize the particles, followed by characterization results and discussion. This part ends with the drawn conclusions and recommendations.

Part II: Design and realization of a CW-STED super-resolution microscope setup

This part starts with an introduction on super-resolution microscopy in general and the motivation for stimulated emission depletion (STED) microscopy. The theoretical background for the STED principle is presented followed by the design of a custom built CW-STED which is discussed in detail. Also the main practical difficulties in building a STED setup and initial characterization is presented. This part of the report ends with some conclusions and a future outlook on the realized setup.

The appendices for both Part I and Part II can be found in **Part III: Appendices**.

Contents

I	Upconversion Nanoparticles	1
1	Introduction	3
2	Theory	6
2.1	Upconversion dopants	6
2.2	Host lattice	7
2.3	Power dependence	8
2.4	Core/shell construction	8
3	Experimental section	10
3.1	Sample preparation	10
3.2	Microscope setup	12
4	Results	14
4.1	Single particle brightness characterization	14
4.2	Power dependence	20
4.2.1	Bulk power dependence	21
4.2.2	Single-particle power dependence	22
4.3	Emission spectrum	25
4.3.1	Bulk sample spectra	25
4.3.2	Single-particle spectra	26
5	Conclusions	29
6	Recommendations	31

II	STED Setup Design	33
7	Introduction	34
8	Theory	36
8.1	Fluorescence and stimulated emission	36
8.2	Diffraction limit	38
8.3	Super-resolution imaging with Stimulated Emission Depletion	39
8.3.1	STED beam shaping	40
8.3.2	Obtainable resolution	42
9	Setup design	44
9.1	Fluorescence confocal microscopy	44
9.2	Pulsed STED vs. CW-STED	45
9.3	Design	49
9.3.1	Laser source motivation	50
9.3.2	Fiber coupling and collimation	50
9.3.3	Beam adjustment	51
9.3.4	Microscope body	52
9.3.5	Emission path and detection	52
9.4	Practical difficulties	53
9.4.1	Dichroic flatness	53
9.4.2	Polarization problems	54
9.4.3	Phase plate hit off-center	56
10	Setup characterization	58
11	Conclusions	63
12	Future outlook	64
III	Appendices	65
A	Symbols and abbreviations	66
B	Upconversion nanoparticles synthesis procedure	68
C	Additional figures	70
D	STED resolution	74
E	Detailed overview of STED setup	76
F	MATLAB code for focal spot simulation	78

Part I

**Brightness characterization of single core and
core/shell Yb³⁺,Er³⁺-doped NaYF₄ upconversion
nanoparticles**

Chapter 1

Introduction

Fluorescent markers have been widely used in biological and biophysical research to study complex biological processes. These markers result in high imaging contrast between different types of biological tissue. Single proteins can be labeled with fluorescent markers to perform single-molecule studies which is required to investigate the complex biological processes on the smallest scale. However, most of the conventional markers suffer from some major drawbacks such as photobleaching and photoblinking. The property of photobleaching can in fact be useful when it is used in techniques like Fluorescence Recovery After Photobleaching (FRAP) and Fluorescence Loss In Photobleaching (FLIP), but for general imaging purposes and single-molecule experiments this property is considered detrimental. Furthermore, conventional markers are typically excited in the visible or UV-range of the optical spectrum, which is not ideal for biological labeling because of the low penetration depth of visible/UV light in tissue and the autofluorescent background signal resulting from fluorescent biomolecules.

Upconversion nanoparticles are a group of promising luminescent particles that have come to the attention in the last decade. These particles consist of a nanocrystal host lattice doped with transition metal ions or in most cases trivalent lanthanide ions. In a suitable host lattice and a well-chosen excitation wavelength, the lanthanide ions can show efficient energy transfer upconversion. Upconversion is a non-linear optical process in which two or more photons are sequentially absorbed followed by the emission of light at a lower wavelength.

$\text{NaYF}_4: \text{Er}^{3+}, \text{Yb}^{3+}$ is one of the most efficient upconversion materials known to date and is therefore considered to be the most promising material for creating luminescent upconversion nanoparticles. Recent studies on these particles show no photoblinking behavior and do not show any form of photobleaching even after hours of continuous high power illumination [2]. These particles are efficiently excited by near-infrared (near-IR) wavelengths and emit in the visible wavelength range, which is in clear contrast to conventional fluorophore luminescence where the emission profile is red-shifted in reference to the excitation profile (see figure 1.1). Excitation in the near-IR brings along some experimental difficulties since it is not visible for the human eye. However, near-IR also has a great advantage over visible wavelength excitation since the autofluorescence background signal in biological samples is known to be much lower for near-IR excitation as compared to visible wavelengths [2, 3] thereby gaining higher imaging contrast. Near-IR also has a larger tissue penetration depth compared to visible wavelengths, which makes upconversion particles also promising for use as an optical contrast agent for example in tumor marking. Because of these advantageous properties, upconversion particles are promising alternatives for conventional fluorophores and quantum dots to be used as a biological imaging label.

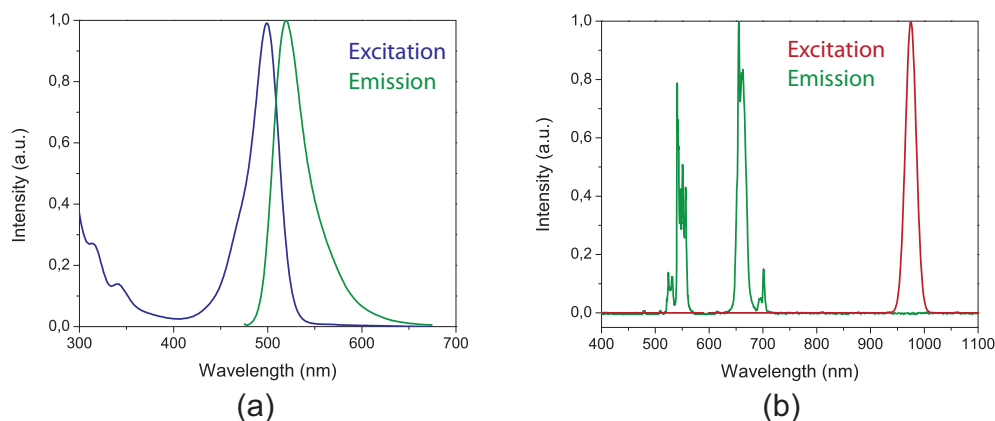


Figure 1.1: (a) The excitation and emission profile of a commonly used fluorescent dye (Alexa 488). The emission profile is red-shifted compared to the excitation profile. (b) The excitation and emission profile of $\text{NaYF}_4: \text{Er}^{3+}, \text{Yb}^{3+}$ upconversion nanoparticles. The particles are efficiently excited in the near-IR (975 nm), and their emission profile is blue-shifted to the visible wavelength range.

Despite their advantages over conventional markers, the synthesis of efficiently luminescing upconversion particles with sizes of around 10 nm still results in insufficient quality [4]. This small size is required for the replacement of conventional molecular fluorescent markers which allow estimation of the position of single molecules within cellular structures with nanometer precision. The small particle size generally leads to a significant decrease in brightness as compared to the same quantity of bulk material. The main focus of research on these particles is therefore on the synthesis of reproducible and efficiently luminescing particles. Some studies have indicated that by applying an outer passive shell around an active doped core the brightness can be increased significantly [3, 5, 6, 7]. Since the sole purpose for the surrounding shell is to shield the ions in the core from the quenching outer environment, the addition of a passive shell should lead to efficiencies comparable to the bulk material. However, in these studies it is observed that the luminescent efficiency of the particles are still orders of magnitudes less than the bulk material and moreover the brightness of the particles is observed to increase with increasing shell thickness. One study indicated that by applying a 3 nm thick shell around the core, the particle brightness was increased by a factor of 15 [5]. However, the efficiency of the bulk counterpart is never reached. This behavior is still not well understood. Most studies on upconversion nanoparticles are focused on ensemble measurements, while optical characterization on a single particle level is important to exclude ensemble effects and study heterogeneity differences between single particles. To our knowledge there is no study on a statistically relevant number of single upconversion nanoparticles. Optical characterization on a single particle level might therefore lead to new insights that can be used to optimize the synthesis process with the ultimate goal to maximize the particle quantum efficiency. Additionally, for reliable single-molecule tracking experiments the optical behavior of individual markers needs to be addressed.

In this study, the brightness of single upconversion particles is characterized with a single-photon counting scanning confocal microscope setup. The brightness is characterized for core-only and three different core/shell structures. All structures consisted

of a NaYF_4 nanocrystal core doped with Er^{3+} and Yb^{3+} ions, surrounded by a passive NaYF_4 shell of varying thickness.

Furthermore, this report gives insight in the power dependence and emission spectrum of both ensembles of particles and single particles. The feedback of this study can be used to optimize the synthesis process to ultimately produce small and bright upconversion nanoparticles that can be used as biological markers.

Chapter 2

Theory

Upconversion materials have interesting optical properties that make them very suitable as luminescent nanoparticles. In this chapter the energy transfer process leading to upconversion in the dopant ions will be introduced. Next, the choice for dopants and host lattice used in this study is argued, followed by a theoretical description of the power dependence of upconversion materials. The core/shell concept for upconversion nanoparticles plays a central role in this study and is presented at the end of the chapter.

2.1 Upconversion dopants

Lanthanide ions are often used as dopants in upconversion materials due to their characteristic long lifetime of the intermediate excited states. These long lifetimes, typically in the order of μs to ms [8, 9], allow efficient excitation to an even higher energy state by absorption of a sequential photon. This sequential absorption of photon energy is prominently efficient when the energy gaps between subsequent levels are similar spaced in a ladder-like fashion. This type of energy-level structures can be found for lanthanide ions such as Er^{3+} , Tm^{3+} and Ho^{3+} which are therefore the most commonly used ions in upconversion materials. The repeating occurrence of an energy gap of about 10350 cm^{-1} in its energy scheme makes Er^{3+} a very efficient upconverting ion [4, 7]. This re-occurring energy gap occurs multiple times in the energy level structure of Er^{3+} , which makes two, three or even higher photon upconversion processes possible with the use of a single monochromatic light source, as is illustrated in figure 2.1. The energy-level structure of these ions is a result of the spin-orbit splitting of electrons in the partially filled 4f electron sub-shell. Because 4f-4f transitions are Laporte-forbidden, direct absorption of excitation light is very inefficient [4]. To overcome this problem, upconversion materials are often doped with an additional strong absorbing lanthanide ion with an energy gap that matches the gaps in the energy-level scheme of the emitting ion. This results in very efficient (quasi-)resonant energy transfer between both ions. This co-doped ion is often referred to as sensitizer, whereas the emitter is called activator. For Er^{3+} the most suitable and most used sensitizer is Yb^{3+} , which has an energy gap of about 10000 cm^{-1} thereby matching multiple energy transitions in the Er^{3+} ion. This energy gap is efficiently bridged by absorption of a 980 nm photon, which is in the near-IR-range.

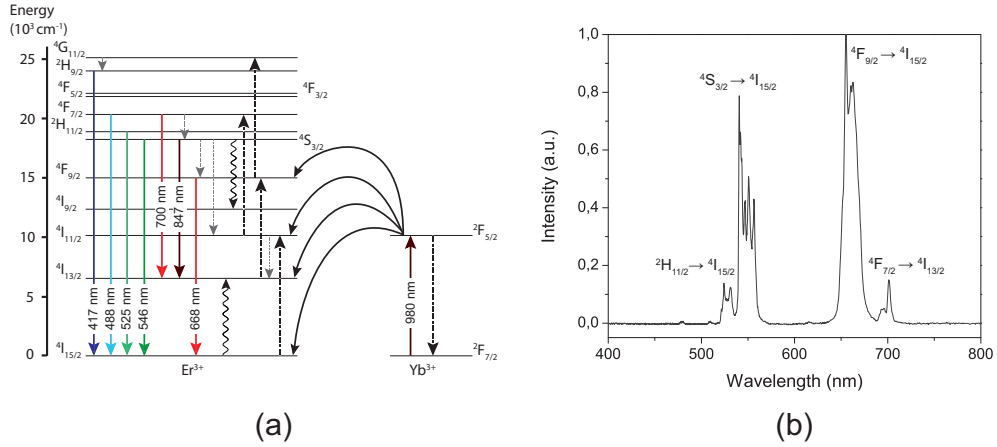


Figure 2.1: (a) The energy diagram of NaYF₄:Er³⁺, Yb³⁺ sensitized upconversion representing the upconversion processing leading to emissions in the visible range, (b) Measured emission spectrum of a high concentration upconversion nanoparticles on a coverslip. The transitions matching the emission band are indicated.

2.2 Host lattice

The host lattice for the doped ions has a large influence on the efficiency of the upconversion process. The crystal structure of the host lattice determines the relative spatial positions of the dopants and the type of anions surrounding the dopant [4]. Furthermore, the composition of the host lattice determines the phonon energies of the crystal lattice. The efficiency of the upconversion process depends on the lifetime of the intermediate excited states which is related to the phonon energies. This lifetime will increase with lower phonon energies since this is directly related to the number of phonons needed to bridge the energy gap as follows from the following equations. The multiphonon relaxation rate is given by [10]:

$$R_{\text{MPR}} = C \exp(-p\beta), \quad (2.1)$$

where C and β are positive constants characteristic for the host material. p is the number of highest energy phonons needed to bridge the energy gap and is given by

$$p = \frac{\Delta E}{\hbar\omega_{\text{max}}}, \quad (2.2)$$

where ΔE is the energy gap and $\hbar\omega_{\text{max}}$ represents the unit for the effective vibrational mode. Equation 2.1 shows that the probability of multiphonon relaxation decreases exponentially with the number of phonons needed to bridge the energy gap. Hence, to obtain long lifetimes for the intermediate energy states it is important to keep the multiphonon relaxation rate low. This can be realized by using a host material with low maximum phonon energy. Fluoride materials, such as NaYF₄, are therefore often used since these materials have low phonon energies ($\sim 350 \text{ cm}^{-1}$ [4]). The Na⁺ and Y³⁺ ions in a NaYF₄ lattice have an atomic radius very similar to the typical dopant ions, preventing the formation of defects and lattice stress. NaYF₄ has therefore proven to be a very suitable host for efficient lanthanide upconversion. NaYF₄ can be

synthesized in two crystal forms: cubic (α -NaYF₄) and hexagonal (β -NaYF₄). The hexagonal form is known to result in higher upconversion efficiency [4, 11].

2.3 Power dependence

Upconversion is a nonlinear optical process, i.e., the optical response (luminescence) is not directly linear dependent on the excitation power. The actual power dependence in upconversion, especially for lanthanide doped materials, is not trivial since their typically long intermediate state lifetime can lead to population saturation of these energy states [12, 13, 14].

Two satisfying theoretical models have been developed describing the power dependence of upconversion materials. The first model by Pollnau *et al.* [12] describes the power dependence of non-sensitized upconversion, while the second model by Suyver *et al.* [13] takes sensitized upconversion into account. Both models showed good agreement in experiments for multiple (bulk) upconversion materials. Also both models show that in the low power density regime the power dependence scales as $I \propto P^i$ where I denotes the emission intensity, P the laser power density and i the number of photons needed in the specific upconversion process.

The difference between the two models becomes relevant in the high power density regime. For non-sensitized upconversion, the power dependence scales as $I \propto P^{m/n}$, where m denotes the number of upconversion steps needed to populate the energy level, n denotes the number of steps needed for the highest upconversion process possible. Suyver *et al.* showed that for sensitized upconversion the power dependence at high power density is very different from non-sensitized upconversion. In this case, the power dependence will be reduced to $I \propto P^1$, i.e., the emission will be independent of the number of upconversion steps needed to populate the different energy levels. This behavior results from the assumption that at high power densities the upconversion process is the main depopulation process for the intermediate energy levels. Or in other words: the upconversion rate from a certain state to a higher energy state is much larger than the relaxation rate to the lower lying levels. This results in population saturation of intermediate energy levels. The upconversion process from these saturated levels now scales linear with the laser pump power. A more rigorous description of this model can be found in [13], where also experimental results on the power dependence of bulk NaYF₄: 18% Yb³⁺, 2% Er³⁺ are presented. These results on bulk material showed that the crossover point to saturation was obtained at ~ 10 W/cm². Because the Suyver model does not take into account effects such as sample heating, cross relaxation or additional non-linear optical processes that can occur at very high power densities, the power dependence behavior for upconversion materials in the 'very high power density' regime is not predicted by this model. However, it is very likely that at very high power densities the highest energy levels will reach complete population saturation, i.e., increasing the laser power in this regime will not lead to any increase in luminescence.

2.4 Core/shell construction

Because of the large surface-to-volume ratio, upconversion nanoparticles have a much lower efficiency than their bulk counterpart. In order to create particles with higher efficiency, researchers have created particles with different types of shells. The main

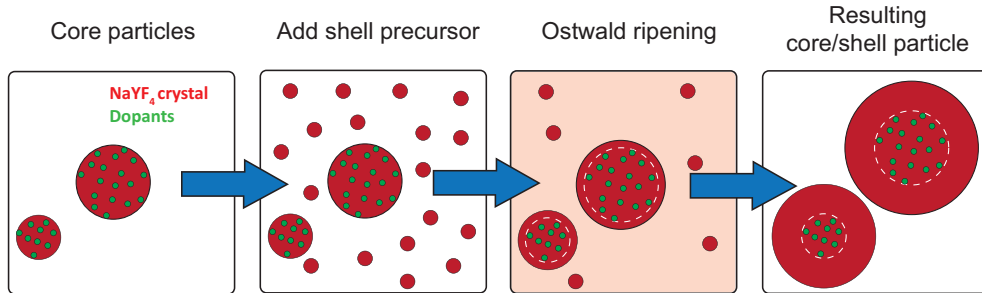


Figure 2.2: Cartoon illustrating shell synthesis by Ostwald ripening. Small crystals of the shell material (red dots) are formed by adding shell precursors to core particles (large red circle), which are doped with lanthanide ions (green dots). The small shell particles dissolve (light red) and re-crystallize on the core particles. This ripening process leads to a shell around the doped core (right image).

function of the shell is to shield the lanthanide ions from the quenching sites on the surface. When a passive shell is applied around the core, the doped ions in the core of the core/shell particles are effectively shielded from quenching by the outer environment, especially from the ligands on the shell surface. This shielding reduces the electron-phonon coupling which is the main cause for non-radiative decay to the ground state. Because the non-radiative decay rate is decreased by the surrounding shell, the upconversion process (excitation to higher energy states) becomes more efficient compared to core-only particles. The most straightforward choice for shell material is to use the pure (undoped) host-material of the core as this gives the smallest possible lattice mismatch between the core and the shell [4]. Yi and Chow [15] already showed in 2007 that a NaYF_4 shell around a $\text{NaYF}_4:\text{Yb}^{3+},\text{Er}^{3+}$ core greatly enhances the particle brightness.

It is known that during both particle and shell synthesis, that the shell precursors form intermediate small particles before creating the end product. These small particles are energetically less stable than larger particles due to their smaller surface-to-volume ratio. This leads to a process called Ostwald ripening: the small particles will dissolve and recrystallize on the larger particles [16]. This process is illustrated in figure 2.2. Johnson *et al.* [17] recently showed that controllable shell growth is also possible by using small sacrificial nanocrystals directly as shell precursor.

The strength of dipole-dipole interaction scales with r^{-6} , where r is the distance between two ions or between an ion and a quenching site. As a result, the interaction strength will decrease very fast with increasing distance. Thus when the shell is sufficiently thick, there should be neglectable interaction between the active core and the quenching outer surface and therefore if the shell thickness would be increased even further, the particle brightness would remain constant. However, in all core/shell nanoparticle studies so far, it has been observed that the efficiency of core/shell particles keeps increasing with increasing shell thickness. This observation indicates that there are some fundamental aspects missing in our understanding of the core/shell concept. The aim of this study is not to look into the brightness of an ensemble of particles, but rather to obtain a single-particle brightness distribution. This single-particle brightness characterization might give new insights on the understanding of the core/shell concept.

Experimental section

3.1 Sample preparation

$\text{NaYF}_4:\text{Er}^{3+}, \text{Yb}^{3+}$ particles with constant core volume and varying shell volume were synthesized at the University of Osnabrück (Appendix B). Transmission Electron Microscopy (TEM) images of the different samples are shown in figure 3.1. The average particle size was determined from multiple TEM images. The properties of the samples used can be found in Table 3.1.

Samples for optical characterization were created by spin-coating 30 μl of a low concentration of particles in hexane (Sigma Aldrich) on a glass coverslip at 6000 rpm for 30 seconds. The glass coverslip was cleaned in nitric-acid (65%) and extensively rinsed with HPLC grade water and subsequently with HPLC grade methanol and passively dried before spin-coating. The optimal particle concentration at which the single particles were spatially separated and homogeneously distributed over the sample was determined via a dilution series, minimizing the probability of having multiple particles per diffraction limited spot. Typically the stock solution was diluted around 5000 \times to obtain the optimal particle concentration for single particle characterization.

To exclude the presence of particle clusters in the stock solution, Dynamic Light Scattering (DLS) measurements were performed with a commercially available Malvern Zetasiser S. For each sample three measurements (10 runs of 10 seconds for each measurement) were performed. The results of these measurements are shown in figure 3.2 and the results are quite similar to the sizes obtained from TEM images, which indicates that the stock solutions contain single particles and no particle clusters.

Sample name	core:shell ratio	Average particle size
ANR 10	1:0	11 nm
ANR 71	1:2	15 nm
ANR 73	1:3	17 nm
ANR 116	1:7	21.5 nm

Table 3.1: The properties of the samples. The sample name is related to the synthesis batch. The core:shell ratio states the core:shell volume ratio. Particle sizes were determined from TEM measurements.

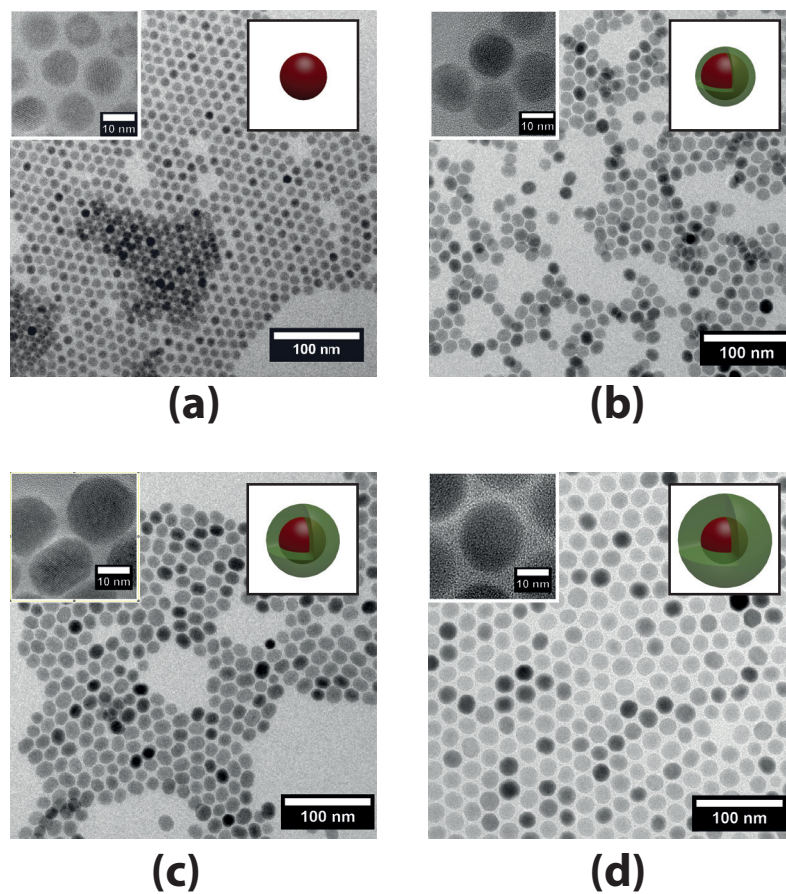


Figure 3.1: TEM measurements of the samples. The insets located on the right-hand side in each figure show the cartoon of the core:shell structure corresponding with the sample core:shell design. (a) Core-only particles, (b) core:shell 1:2 particles, (c) core:shell 1:3 particles, (d) core:shell 1:7 particles. The TEM images are courtesy of the Anorganische Chemie I group at the University of Osnabrück (also see Appendix B)

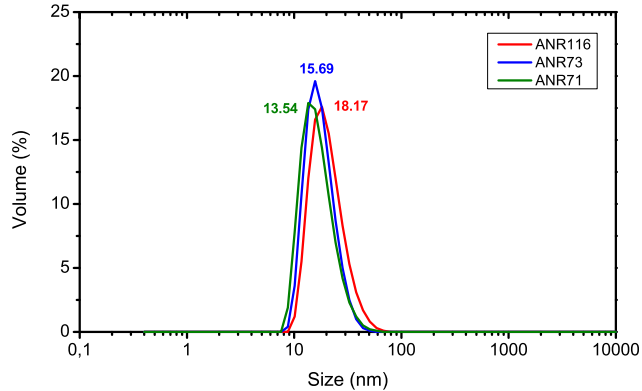


Figure 3.2: Results of Dynamic Light Scattering (DLS) measurements on the samples. For each core/shell structure three measurements were performed. Each measurement resulted in a similar peak value. The results shown here are from one measurement (10 runs of 10 seconds).

3.2 Microscope setup

A schematic of the setup is presented in figure 3.3. A 975 nm excitation line was selected by placing a 975 nm clean-up filter (D975/50M, Chroma) in the reflection path of a dichroic beamsplitter (FF670-SDi01, Semrock) positioned in the output beam of a Fianium SC-400-2PP supercontinuum laser source operating at a 20 MHz repetition rate. The light was then coupled into a single-mode IR fiber with a 10 \times microscope objective (10 \times Olympus Plan Achromat Objective, 0.25 NA, Olympus) to obtain a clean single-mode Gaussian beam. A 4 \times microscope objective (4 \times Olympus Plan Achromat Objective, 0.10 NA, Olympus) was used to collimate the light exiting the fiber. The collimated light passed through a long-pass filter (FF01-776/LP-25, Semrock) to suppress any remaining short wavelength light. The collimated beam was then directed into an Olympus IX71 inverted microscope via a wedge-beamsplitter. The power going into the back aperture of the objective was either 107 μ W (non-saturating regime) or 585 μ W (saturating regime). The excitation light reflected by the wedge-beamsplitter was focused on the sample with a 60 \times water-immersion objective (UplanSAPO, NA 1.2, Olympus). The sample was positioned on a XY piezo scanning stage (P-527.3 CD, PI) controlled by a PI E-710 piezo controller. The excitation light was focused onto the surface of the coverslip that could be observed by visualizing the reflection with a Zeiss AxioCam HRC connected to the camera port on the microscope. The emitted light from the upconversion particles passes through the wedge-beamsplitter. A short-pass filter (FF01-770/SP-25, Semrock) in combination with a dichroic mirror (FF746-SDi01, Semrock) were used to suppress the remaining excitation light. The emitted light is focused onto the active area (50 μ m) of a Single Photon Avalanche Diode (SPAD, MPD-5CTC, PicoQuant) by a 50 mm achromat lens. The signal from the SPAD was analyzed with a single-photon counting computer card (Becker-Hickl SPC-830). Raster scans and time traces were obtained using a custom written LabView program and were further analyzed with MATLAB software.

The optical power going into the microscope was measured during characterization measurements to ensure constant power. This was realized by directing the reflected light from an additional beamsplitter (92% transmission, 8% reflection) on an optical power meter (Newport, 1830-C).

Power densities were calculated by calibrating the power measured at the the power meter with the power going into the back aperture of the objective. The following equation was used to calculate the approximate spot size in the focus of the objective:

$$2w_0 = \frac{4\lambda}{2\pi\text{NA}} \quad (3.1)$$

where $2w_0$ is the focal spot diameter, λ is the wavelength used (975 nm) and NA is the numerical aperture of the microscope objective (NA = 1.2). This leads to a spot diameter of $2w_0 = 517$ nm. The power density was then calculated with $I = P/(\pi w_0^2)$, where P is the power in the back aperture of the objective.

Emission spectra measurements were performed by coupling the emission light into a multi-mode fiber and connecting the fiber to a custom built prism based spectrometer with a sensitive spectroscopy detector (Andor Newton DU971P BV EMCCD) with the sensor cooled to -60° C to minimize dark counts. The spectra were wavelength calibrated using a Mercury-Argon light source (CAL-2000, Ocean Optics) and captured with Andor Solis software. All experiments were performed at room temperature.

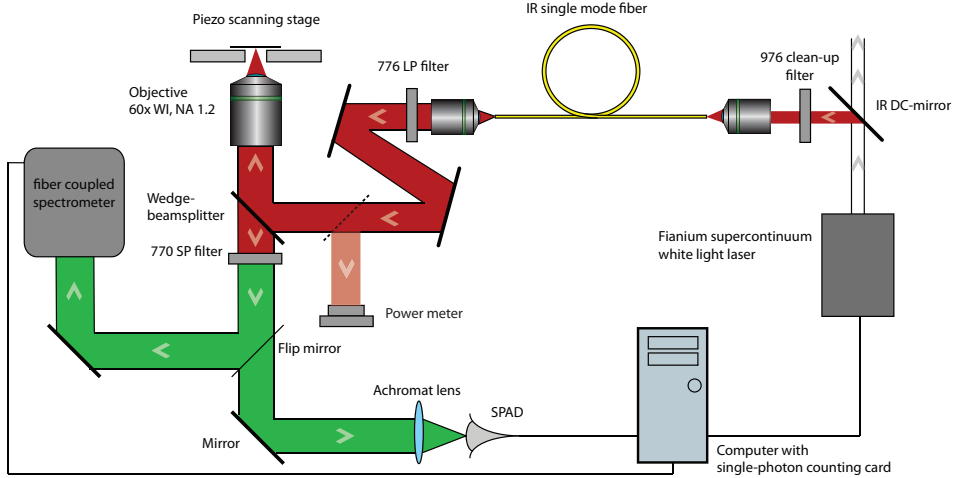


Figure 3.3: A schematic overview of the scanning confocal microscope setup. A 975 nm wavelength band from a supercontinuum laser source is coupled into a single mode fiber, coupled out, collimated and directed into a microscope adjusted with a piezo scanning stage. The luminescent light is collected by the objective and directed to an Single Photon Avalanche Diode (SPAD) or coupled into a multi-mode fiber and directed to a custom built prims-based spectrometer.

Results

The brightness of upconversion nanoparticles have been characterized for core-only particles and three core/shell structures with varying shell thickness. All structures consisted of a NaYF_4 nanocrystal core doped with Er^{3+} and Yb^{3+} ions, surrounded by a passive NaYF_4 shell of varying thickness. In this chapter, the results of the brightness characterization are presented and discussed. Furthermore, the results on the power dependence and emission spectrum of both ensembles of particles and single particles are presented and discussed.

4.1 Single particle brightness characterization

Samples containing spatially separated particles were created using the protocol described in the experimental section. Raster scan images of the prepared samples for optical characterization (see section 3.1) were obtained by scanning the piezo stage of the microscope setup in x and y direction. A scan showing a single diffraction limited spot is illustrated in figure 4.1 where the Gaussian fit of the intensity profile along the dotted line gives a FWHM of ~ 580 nm, which is slightly larger than the calculated spot size in the focus of the objective (~ 520 nm). Figure 4.2 (a) shows a scan of a typical sample, whereas the 3D intensity representation (b) of the same scan illustrates that the diffraction limited spots in the scanned region vary in brightness. The absence of very bright spots indicates that no particle clusters are present after the spin-coating process. Furthermore, the diffraction limited spots do not show blinking behavior which is typically present in scans of single quantum dots, single dyes or single VFP's. Additionally, it is interesting to note that scans of old spin-coated samples which had been in contact with air for months, still had comparable brightness to new spin-coated samples. Although this was not investigated quantitatively, this observation indicates the high chemical- and photostability of the particles.

Some more typical scan images are shown in figure 4.3. The intensity of single particles was determined by performing time trace at the center location of single diffraction limited spots. Figure 4.4 present a time trace recording of 200 seconds on a single particle. The photon counting histogram on the right indicates that the detected counts are shot noise limited (Poisson distribution) with a well-defined mean. Furthermore, this long time trace shows no signs of blinking or photobleaching thereby illustrating the high photostability of these particles. Here it must be noted that an individual upconversion particle is not a single emitter, since there are many emitting ions present in a single particle. A particle doped with very few or even a single ion might therefore still be prone to blinking, but this is beyond the scope of this study.

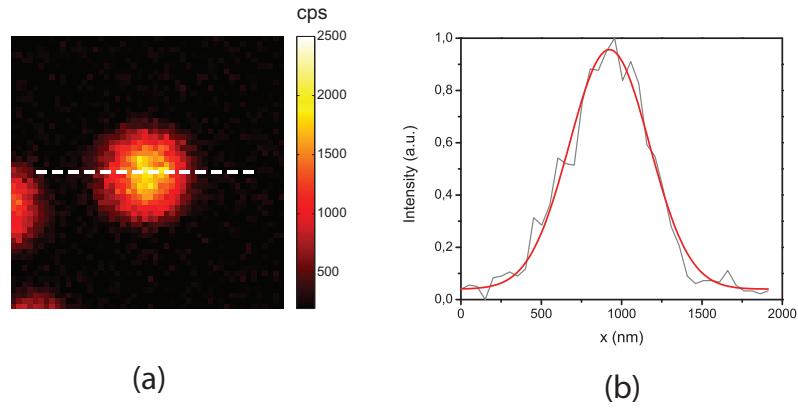


Figure 4.1: (a) Scan image showing a single diffraction limited spot, (b) intensity profile along the dotted line with a Gaussian fit (FWHM of ~ 580 nm).

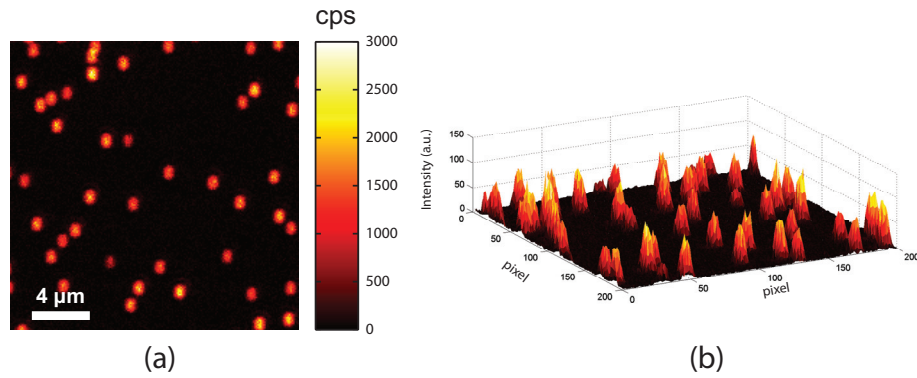


Figure 4.2: A scan obtained for a core:shell (1:3 volume ratio) sample. (a) Image obtained by scanning a $20 \times 20 \mu\text{m}^2$ area with a resolution of $0.1 \mu\text{m}$ per pixel and 40 ms integration time per pixel, (b) 3D representation of (a) illustrating that particles from a single sample have varying brightness. The absence of extremely bright spots indicate that that there are no clusters present. Excitation power density is $\sim 3.2 \times 10^5 \text{ W/cm}^2$.

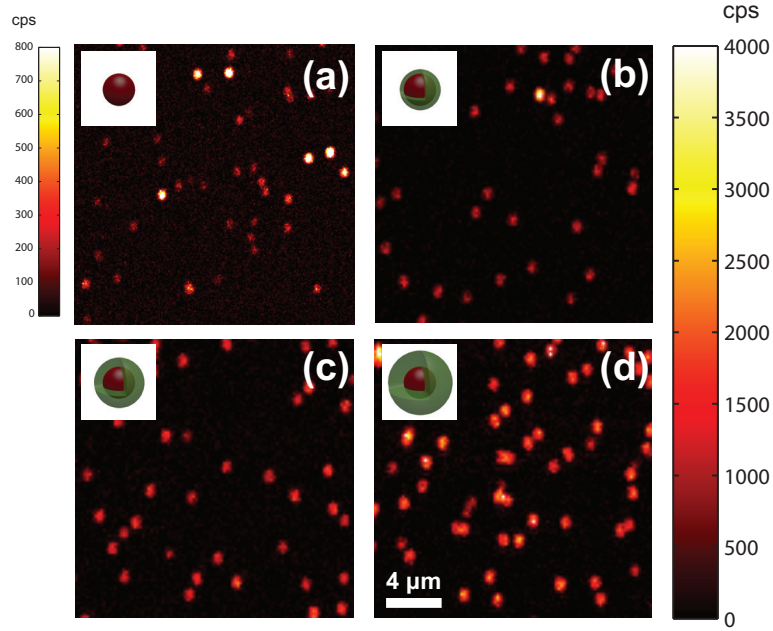


Figure 4.3: Typical raster scanned images obtained with the scanning confocal microscope setup (a) core-only particles, (b) core:shell (1:2 volume ratio) particles, (c) core:shell (1:3 volume ratio) particles, (d) core:shell (1:7 volume ratio) particles. The images are obtained by scanning a $20 \times 20 \mu\text{m}^2$ region with a resolution of $0.2 \mu\text{m}$ per pixel and 20 ms integration time per pixel. The colorbar on the right denotes the intensity scale (counts/second) used for figures (b),(c) and (d), whereas the small colorbar on the left denotes the scale for (a). Excitation power density was $\sim 3.2 \times 10^5 \text{ W/cm}^2$.

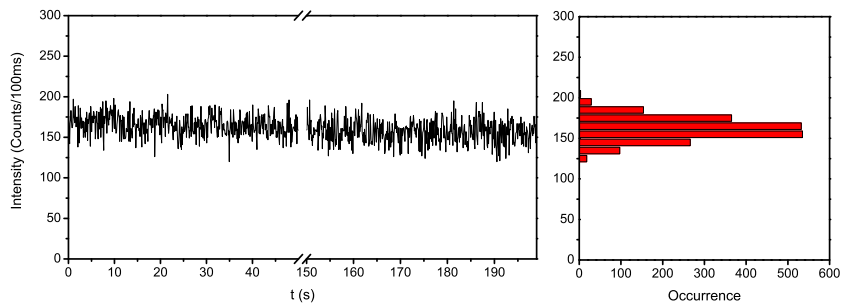


Figure 4.4: A 200 second time trace of a single diffraction limited spot. The time trace does not show any form of blinking or bleaching. The figure on the right shows the photon counts histogram of the intensity time trace. The distribution shows a Poissonian distribution indicating a shot noise limited signal as is expected.

Time traces can be obtained for many individual spots. For each spot, the mean intensity can be determined and from these values a brightness distribution can be produced. This analysis method is also illustrated in figure 4.5. In this method, the diffraction limited spots that are in the near vicinity of a neighboring spot and clearly elongated or enlarged spots were excluded to minimize the probability that multiple particles are excited and detected during a single time trace.

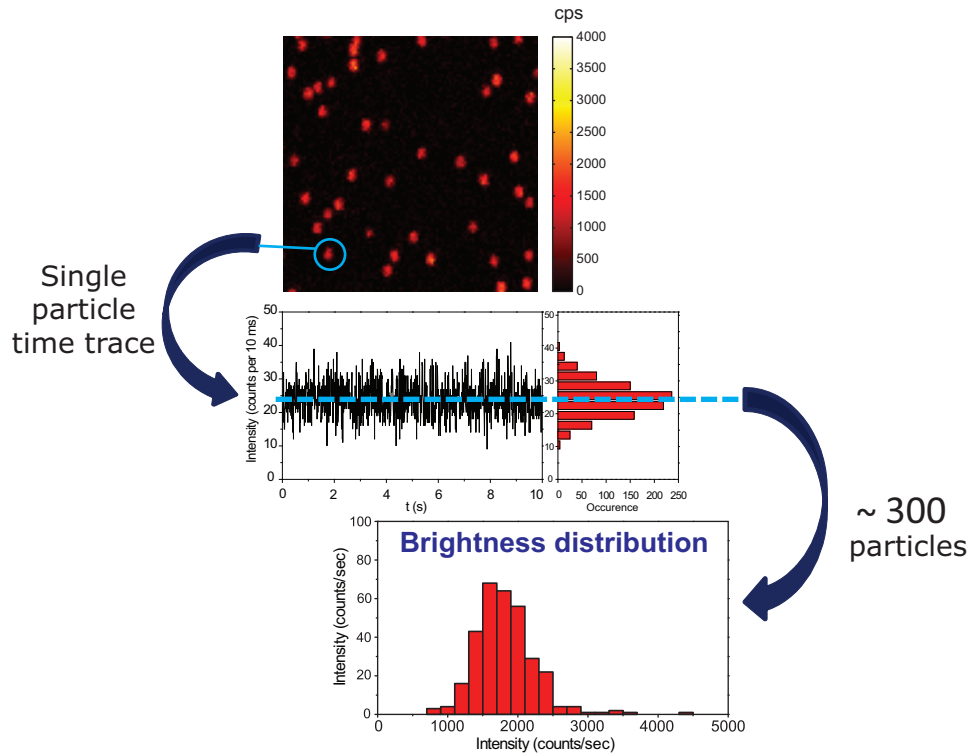


Figure 4.5: Method for obtaining the brightness distribution of single particles. Scan images are obtained at $20 \times 20 \mu\text{m}^2$, $0.2 \mu\text{m}$ per pixel, with 20 ms integration time per pixel. At each location of a diffraction limited spot a 10 second intensity time trace is recorded (10 ms bin size). The mean value of the time trace is obtained. This is repeated for many single particles to obtain a brightness distribution histogram of single particles.

Figure 4.6 shows the brightness distributions obtained from time traces of ~ 300 particles for each sample measured at two different power densities. The distributions are normalized to the total number of particles measured for each sample. For an overlay representation of the two different power density distributions, the reader is referred to the Appendix C of this report. Two main things can be observed from figure 4.6. The first observation is the distribution shift towards higher intensities with increasing shell thickness. This has also been observed in earlier ensemble studies, and is here also confirmed on a single particle level. The second observation is quite interesting: the distribution is broadening with increasing shell thickness. These two main observations will be discussed separately.

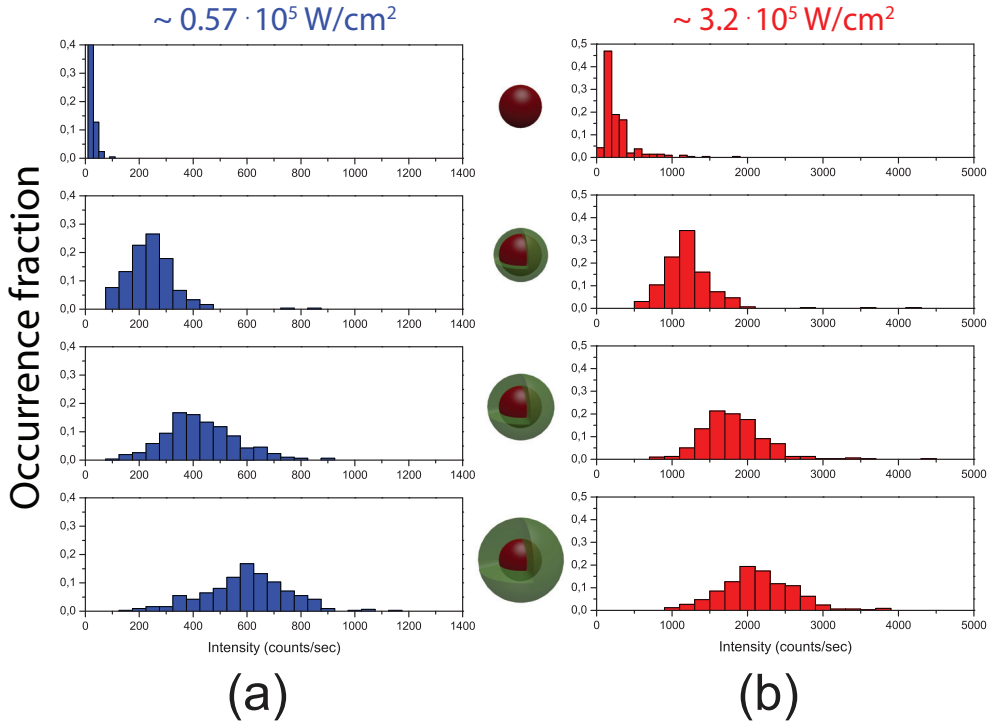


Figure 4.6: Brightness distributions obtained from the average intensity of single upconversion nanoparticles at two power densities. The distributions were obtained from ~ 300 particles (10 second time trace per particle) for each core/shell structure. The intensity increase and distribution broadening for increasing shell thickness can be observed for both power densities.

Sample name	core:shell ratio	$\sim 0.57 \times 10^5 \text{ W/cm}^2$ Peak intensity (counts/second)	$\sim 3.2 \times 10^5 \text{ W/cm}^2$ Peak intensity (counts/second)
ANR 10	1:0	20 ± 20	150 ± 100
ANR 71	1:2	250 ± 50	1200 ± 200
ANR 73	1:3	400 ± 50	1800 ± 200
ANR 116	1:7	600 ± 50	2000 ± 200

Table 4.1: Peak values obtained from the brightness distributions in figure 4.6. The error margin is taken equal to the bin size.

In order to quantify the particle brightness for each core/shell structure, a peak brightness value (center of distribution) was obtained (see table 4.1). This value is considered to be a better quantitative representation than the mean intensity, since a few bright spots as a result of multiple particles in one diffraction limited spot could lead to an overestimation of the mean intensity. From this table it is clear that core/shell particles are much brighter than the core-only particles. We observe an intensity increase of approximately 8, 12 and 13 times the intensity of core-only particles for respectively 1:2, 1:3 and 1:7 core:shell volume ratio at a power density of $\sim 3.2 \times 10^5$ W/cm². For a power density of $\sim 0.57 \times 10^5$ W/cm² the core-only particles are dark noise limited (~ 20 counts/second); the core-only particles are so dim that they cannot be distinguished from the noise. When the dark-noise limit is used as the core-only intensity, the core/shell show an intensity increase of approximately 12.5, 20 and 30 times the intensity of the core-only particles at a power density of $\sim 0.57 \times 10^5$ W/cm². The low brightness of the core-only particles is also clearly observed in the scan images, in which these particles (figure 4.3 (a)) are much dimmer as compared to core/shell particles (figure 4.3 (b),(c) and (d)). The lower brightness of core-only particles compared to core/shell particles was already known from previous studies, but to our knowledge this was never quantitatively investigated on a single particle level. The intensity increase for thicker shells indicates that the shell indeed has a significant influence on the particle brightness. The general idea behind this difference is based on shielding as was introduced in the theory section of this report. The brightness distributions also show a few small peaks at higher intensities, which could indicate multiple individual particles were located inside a single diffraction limited spot in a few of the measurements.

Besides the observation of a distribution shift towards higher intensities with increasing shell thickness, a key observation in figure 4.6 is the apparent broadening of the distribution for increasing shell thickness. This broadening is observed for the distributions obtained at both power densities. This broadening can be explained by the presence of dopant ions in the shell. It was always assumed that the shell is completely passive (no ions present), but we argue that during the chemical synthesis of the shell, an additional form of Ostwald ripening occurs (figure 4.7). During this additional Ostwald ripening process, a fraction of the small core particles also dissolve and mix with the dissolved shell material. The dissolved mixture of core and shell monomers re-crystallizes on the core to form the shell, but since the solvent contains a mixture of shell material and dopants, the re-crystallization process results in the presence of dopants in the shell crystal. For longer incubation time with shell precursors, the shell grows thicker but the longer incubation time also results in stronger additional Ostwald ripening, leading to additional dopants in the shell. These shell-dopants create additional energy-migration pathways from the core-dopants to the outer surface of the shell, resulting in additional quenching sites. Because the uptake of dopants during the mixed Ostwald ripening is a random process, the thick shells will have a wider distribution of the number of ions in the shell. This process is a good explanation for the observation that upconversion nanoparticles in general still show very low quantum efficiency as compared the bulk material despite growing large shells around the doped core. In order to increase the efficiency of core/shell particles it would be important to focus on other shell synthesis methods that minimize or exclude the presence of dopants in the shell.

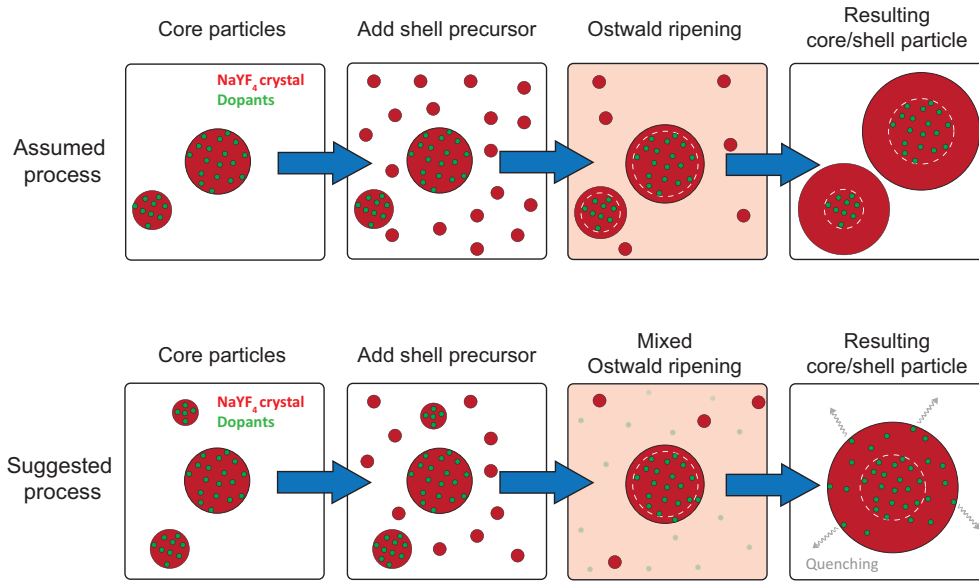


Figure 4.7: Cartoon illustrating the generally assumed process in shell synthesis (top) and the suggested mixed-Ostwald ripening process (bottom). In the assumed process the core dopants are well shielded from the outer environment by the passive shell. In the suggested process, the additional dopants in the shell lead to energy migration pathways from the core-dopants to the outer surface of the shell, resulting in additional quenching sites.

4.2 Power dependence

It might be argued that the additional dopants in the shell also attribute to the brightness increase, and that the shell has become redundant as a result of these shell-dopants. If the shell still has a shielding function, the core/shell particles must have a lower quenching rate than core-only particles. As a result, the power dependence of core/shell particles must differ from the power dependence of core-only particles. Therefore, it makes sense to investigate the power dependence of our different core/shell structures.

Since upconversion is a non-linear optical process, the optical response in terms of emission intensity of the particles does in general not scale linearly with the excitation power density. In section 2.3 it was already shown that in upconversion materials the intensity scales as $I \propto P^i$ where I is the emission intensity, P is the power density of the excitation laser and i is the number of photons needed for the upconversion process. For sensitized upconversion this relation holds only for low power densities, for high power densities the relation reduces to $I \propto P$ as a result of saturation of the intermediate excited states. Since the emission intensity of upconversion materials is highly dependent on the the excitation power and power regime, the comparison of the brightness of upconversion nanoparticles with different core/shell structures may not be straightforward. The power dependence of different core/shell nanoparticles have been scarcely studied in ensemble measurements, but never on a single particle scale. This section presents our power dependence measurements on different core/shell structures in both ensemble (here noted as 'bulk') and on a single particle scale.

4.2.1 Bulk power dependence

The power dependence of bulk samples was experimentally investigated. The bulk samples were created by spin-coating a high concentration of particles in hexane on a coverslip. The laser power was varied with ND-filters positioned in the excitation path and by manually adjusting the power of the laser source. The average emission intensities were obtained from a ten second time trace and each measurement was performed at the same sample location. The results are presented in a double-log graph in figure 4.8. The solid lines show the apparent linear fits with slopes as determined by direct error weighing (OriginPro).

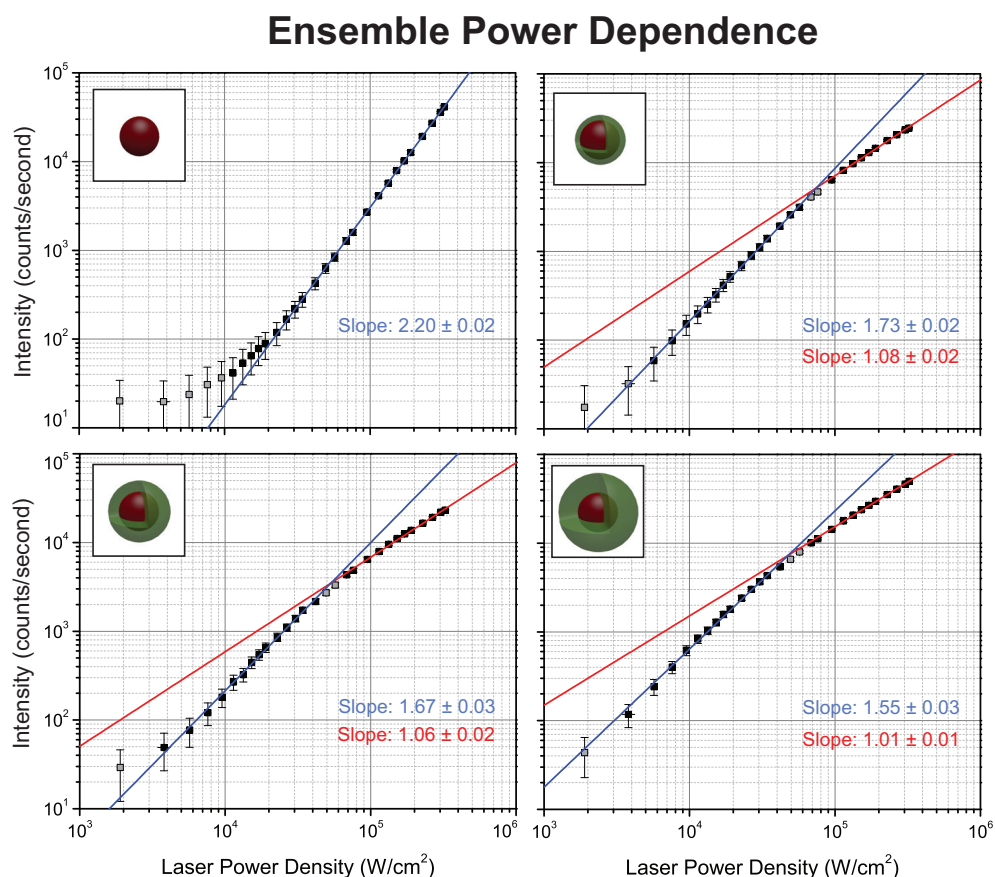


Figure 4.8: A double-log representation of power dependence measurements on samples with high concentration of particles. The solid lines represent the linear fits based on direct error weighing. The error bars are based on the standard deviation from Poisson statistics: $\sigma = \sqrt{\mu}$, where μ is the total number of counts in the time trace. The fitted slopes are also presented with their standard error. The measurement points with error bars that cross the dark noise mean intensity (~ 20 counts/second) and the points located at the 'bending point' are excluded from the fitting (gray points). The inset shows the corresponding core/shell structure for each measurement: ANR10(1:0), ANR71(1:2), ANR73(1:3), ANR116(1:7) in order of increasing shell thickness.

The first thing that comes to notice after observing the results in figure 4.8 is the difference between the power dependence of the core-only sample and all core/shell samples. The core-only shows just a single power dependence regime, whereas all core/shell particles show two regimes. This difference indicates that the shell is actually doing something.

For the core-only sample a best fit slope of 2.20 was obtained, rather close to two which is expected in the low power regime for a two-photon process. The result of a slope with a value larger than two arises from the presence of three photon upconversion processes which is known to occur for blue emission [18], part of the green emission [18] and part of the red emission [2].

The core/shell samples show two power density regimes, the values of the fitted slopes are also shown in figure 4.8. The presence of the two distinctive power density regimes can be explained from the saturation of the intermediate energy states as was discussed in section 2.3: when the power density is high enough, the upconversion rate is much larger than the decay rate to lower levels, this leads to saturation of the intermediate levels. For the core/shell particles a slope very close to one was found at power densities $> 0.7 \times 10^5 \text{ W/cm}^2$. This slope of one is also predicted by the theory based on saturation of the intermediate states. The fitted slope in the low power regime is ~ 1.7 for all core/shell samples, which is clearly lower than in the case of the core-only particles. This might be due to the experimental details: most of the particles in the center of the excitation focus are saturated, whereas particles/ions in the outer region of the focus are not saturated since they feel a lower effective power density due to the intensity gradient of the Gaussian focus. This mixture of saturated and non-saturated particles/ions could lead to a slope smaller than two in the double-log plot at the the low power density regime.

In present literature not many results are presented on the power dependence of upconversion nanoparticles. Most papers have only studied the power dependence of core only particles in solution and at relative low power densities ($< 1 \text{ kW/cm}^2$). Table 4.2 presents an overview of the fitted slopes and power densities found in literature. It can be observed that for low power densities, typically a slope of around two or higher than two are found for both the green and red emission band indicating the presence of both two- and three-photon processes for red and green emission. The only paper that uses similar power densities to our measurements is [14] (last two entries in Table 4.2) where a clear saturation (leveling from a slope of 2 to a slope of 1) was observed. This is surprising since we did not observe saturation for core-only particles in this power density range. However here it must be noted that the core-only particles in [14] had an average size of $\sim 20 \text{ nm}$, whereas our core-only particles were $\sim 11 \text{ nm}$. The larger particle size leads to a decrease in the surface-to-volume ratio, thereby reducing the surface quenching rate and enabling saturation at lower power density.

The fact that we observe saturation behavior for core/shell particles in our power regime and no saturation for core-only particles clearly indicates that the shell does have a significant shielding effect: the core/shell particles have a reduced quenching rate as compared to the core-only particles.

4.2.2 Single-particle power dependence

The power dependence of single particles has also been investigated. The experimental data and their apparent linear fits are shown in figure 4.9. These results again show a difference in power dependence between the core-only and core/shell particles. The core-only particles show a single power density regime in the investigated power range,

Reference	Green emission	Red emission	Power density (W/cm ²)	Particle type
[19]	1.65	1.9	< 3	UC-powder
[20]	1.91 (525 nm) 1.9 (546 nm)	1.9 (668 nm)	< 8	α -NaYF ₄ core-only
[2]	2	2.4	0.1 – 10	core-only
[3]	2.27 (core-only) 2.25 (core/shell)	2.45 (core-only) 2.22 (core/shell)	< 150	core-only core/shell
[1]	2	2.4	0.1 – 1000	core-only
[21]	2.11 (552 nm) 2.19 (526 nm)	2.4 (663.5 nm)	-	nanocrystal
[22]	1.68	1.31	< 2.5×10^3	core-only
[23]	1.89 (521 nm)	1.72 (655 nm)	-	core-only
[14]	2	2	$1 - 60 \times 10^3$	core-only
[14]	1	1	$0.8 - 10 \times 10^5$	core-only

Table 4.2: Power dependence slopes in double-log representations from bulk upconversion nanoparticles in literature. The entries are organized based on increasing power density. Only the last two entries have used similar power densities as in our study and also in this paper the authors observed similar saturation behavior, i.e., a decrease in the fitted slope from 2 to 1.

whereas the core/shell particles show two distinct regimes as was also the case for the bulk samples. The measurement points with error bars that cross the dark noise mean intensity (~ 20 counts/second) are excluded from the fitting. All slopes are significantly lower as compared to the slopes found in the bulk samples which is an interesting finding as this implies that the optical response of single particles in a tightly focused excitation spot differs significantly from the ensemble counterpart. The lower slopes might be the result of heterogeneity of the power dependence of single particles within one sample which cannot be excluded due to the small number of particles investigated in this power dependence study. Additional effects such as extreme saturation, cross-relaxation and sample heating could also lead to this difference.

The observation that the core-only particles only show a single regime in the investigated power region whereas the core/shell particles clearly show an additional (saturated) regime, is similar to the results on the bulk samples (figure 4.8). The slopes of the fitted lines however are much lower as compared to the bulk (high concentration) samples, which holds for all investigated particles. In the high power density regime, the slope of the fit (shown in red) is even lower than one, possibly indicating the presence of non-sensitized upconversion [12]. However, at the high power densities used here a more likely scenario is extreme population saturation of the excited intermediate states since there are only a limited amount of ions present in a single particle. Furthermore at very high power densities the absorption cross section of the Yb³⁺ ions might change and rate constants could become power dependent as a result of sample heating. Also at high power densities the effect of cross-relaxation can have a large influence on the population and upconversion processes. These effects are not included in the models. The power density at which these effects are dominant are not stated in the literature. To our knowledge these are the first results

Single-Particle Power Dependence

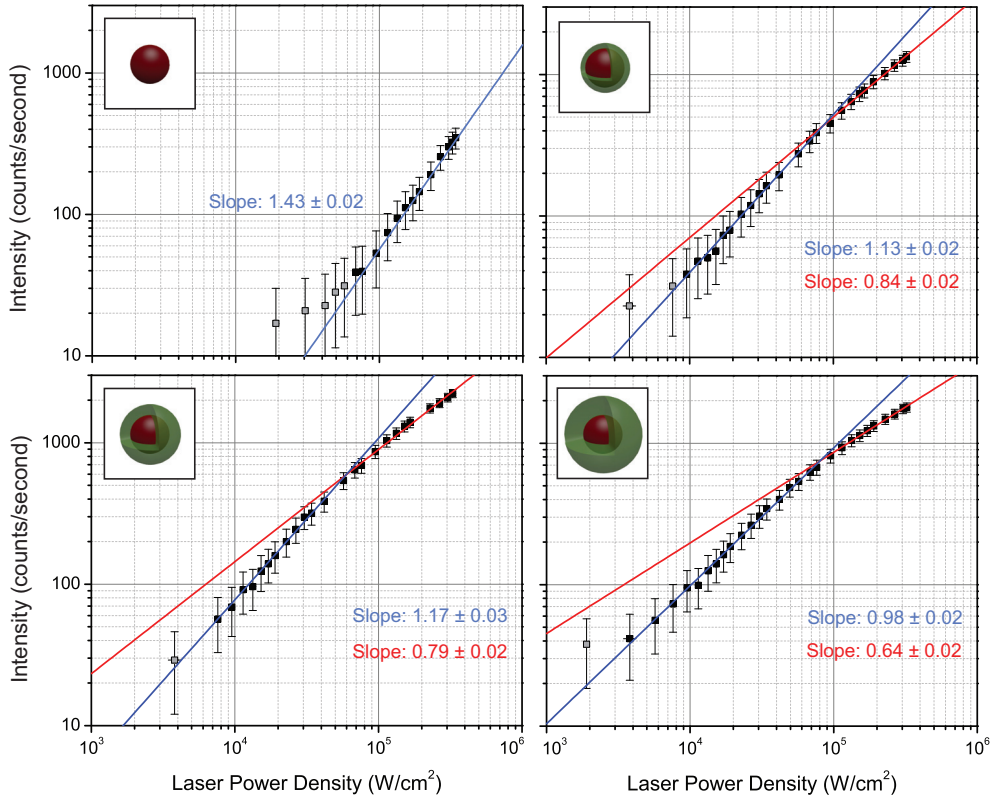


Figure 4.9: A double-log representation of power dependence measurements on a single particle from each core/shell construction. The solid lines represent the linear fit based on direct error weighing. The error bars are based on the standard deviation from Poisson statistics: $\sigma = \sqrt{\mu}$, where μ is the total number of counts in the time trace. The fitted slopes are also presented with their standard error. The measurement points with error bars that cross the dark noise mean intensity (~ 20 counts/second) are excluded (gray points). The inset shows the corresponding core/shell structure for each measurement: ANR10(1:0), ANR71(1:2), ANR73(1:3), ANR116(1:7) in order of increasing shell thickness.

on power dependence measurements on both core-only and core/shell upconversion nanoparticles on a single particle level. Wu *et al.* [2] have presented some brief results on power dependence measurements on single core-only upconversion particles in their supplementary info. The authors found a slope of ~ 1 for both the red and green emission bands in the low power density regime ($\sim 4 \times 10^5 - 1 \times 10^6$ W/cm²) and a slope of ~ 0.5 in the high power density regime ($\sim 1 - 7 \times 10^6$ W/cm²). Note that their low power density regime is even higher than the maximal power density used in our study, which explains their observation of a saturation regime for single core-only particles while we were confined to the lower power density regime without saturation. The results shown by Wu *et al.* also showed a significant decrease of the slope as compared to the bulk measurements, which agrees with our observation.

The initial results shown in this section indicate a clear difference in power dependence of core-only and core/shell particles, which is definitely worth looking into in future research since this would imply that comparison between the brightness of core-only and core/shell particles is not straightforward: it highly depends on the power density at which the brightness of the particles are compared. Moreover, Li *et al.* [24] recently observed a turnover in the power dependence of cubic-phase NaYF₄ (α -NaYF₄) nanoparticle powder, where the emission intensity was found to decrease with increasing laser power when the laser intensity was increased above ~ 6 kW/cm². They attribute this observation to radiative quantum efficiency decrease caused by thermal heating. This reversal point must be much higher for the much more efficient hexagonal-phase NaYF₄ (β -NaYF₄) nanoparticles since to our knowledge this reversal has not yet been observed for these type of nanoparticles. Nevertheless, this reversal point is important for practical considerations, since a high emission intensity is desired while keeping the excitation power as low as possible.

4.3 Emission spectrum

The scanning confocal microscope setup was adjusted with a flip-mirror in the emission path to switch from intensity to spectral measurements. With this setup scheme (Chapter 3.2) it was possible to obtain scan images and subsequently record the local spectrum at any location in the scanned region. Spectra from samples with a high concentration of particles ('bulk') were first obtained, followed by spectral measurements on single particles.

The typical emission profile for NaYF₄: Er³⁺, Yb³⁺ contains peaks centered around ~ 520 nm, ~ 550 nm, and ~ 670 nm. A small blue peak at (~ 410 nm) [5, 13, 18, 25] arises from a three photon process, but is not consistently observed in literature. Furthermore, not all studies show the spectrum below 500 nm, thereby making it difficult to argue whether this peak is consistently present.

4.3.1 Bulk sample spectra

Spectral measurements on bulk samples were performed at two different power densities with an integration time of 20 seconds. The result is shown in figure 4.10. This spectrum agrees with the typical emission profile for NaYF₄: Er³⁺, Yb³⁺ with peaks centered around ~ 520 nm, ~ 550 nm, and ~ 670 nm. The small blue peak (~ 410 nm) is clearly absent in our measurements for all core/shell structures. It might be argued that the power density used in our measurements is not high enough to popu-

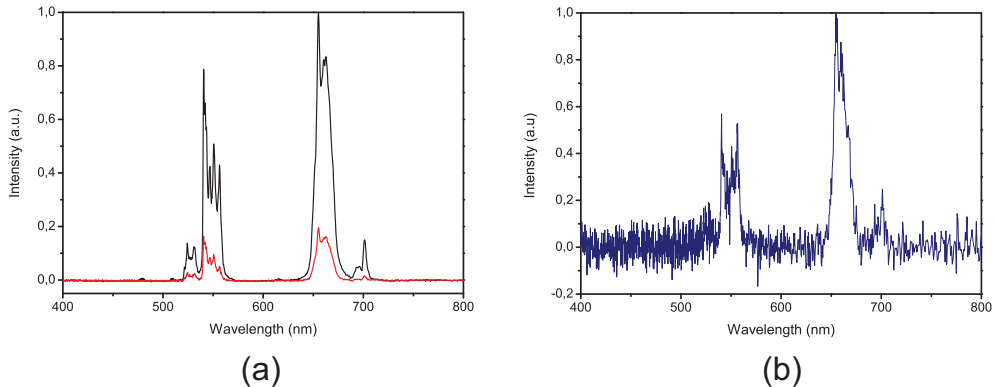


Figure 4.10: (a) Typical background subtracted emission profile of a high concentration spin-coated sample (ANR116) at a power density of $\sim 3.2 \times 10^5$ W/cm² (black) and $\sim 0.57 \times 10^5$ W/cm² (red), (b) A typical background subtracted emission profile of a single particle (ANR73) at a power density of $\sim 3.2 \times 10^5$ W/cm². Integration time for all measurements was 20 seconds.

late the high ${}^2H_{9/2}$ energy level that leads to this transition, for example: the ~ 410 nm peak was also absent in the spectra obtained by Yi *et al.* [26] where they excited samples with an unfocused 980 nm CW laser beam with power densities in the order of 10 W/cm², which is orders of magnitude lower than the power densities used in our study. However, in the studies where this peak was present, the power densities were also typically lower than or comparable to ours, hence the reasoning of insufficient power density seems invalid.

In contrast to the absent peak at ~ 410 nm, an additional peak centered at ~ 700 nm is clearly present in our measurements. This peak is scarcely reported in other studies. In one paper this peak is attributed to the ${}^4F_{7/2} \rightarrow {}^4I_{13/2}$ transition [18], i.e., a transition to another intermediate state instead of the ground state. In Appendix C the spectral measurements on all bulk samples are presented, and it can be observed that at lower power density ($\sim 0.57 \times 10^5$ W/cm²), the ~ 700 nm peak is suppressed or even absent.

4.3.2 Single-particle spectra

Single-particle spectra were already studied by Schietinger *et al.* [18]. In their work, the spectrum of core-only particles of different sizes were characterized and it was concluded that the red/green ratio mainly depends on phonon confinement. Gainer *et al.* [20] recently showed that the red/green ratio can be tuned for ~ 14 nm α -NaYF₄ nanoparticles by changing the repetition rate of the excitation laser. Some other parameters that can influence the emission spectrum include the dopant concentration, possible dopants present in the passive shell, defects in the crystal lattice, and quenching by surface ligands. Since we cannot strictly exclude the influence of any of these parameters on our results, the possible effect of the shell thickness on the emission spectrum of single particles cannot be investigated in a controlled way. The results shown in this section are pilot results that might give new insights on the effect of the shell on the emission profile.

We have obtained single-particle spectra on all core/shell structures (figure 4.10 (b)). These spectra were obtained at a power density of $\sim 3.2 \times 10^5 \text{ W/cm}^2$ with an integration time of 20 seconds. In order to average out possible influences of the mentioned parameters, the spectra of ~ 50 particles were obtained for each core/shell structure. The spectra were background subtracted and averaged to obtain a representation of the overall single particle spectrum (figure 4.11). From these averaged spectra no difference in the red/green ratio was observed for varying shell thickness. However, from this figure the overall spectral intensity increase with increasing shell thickness is clearly visible, which is in line with the results based on the brightness distributions. In order to quantify this, the total spectral intensity in the detected wavelength range was divided by 20 seconds to obtain an indication of the average counts per second per particle detected by the spectrograph. These values are also shown in figure 4.11. Within the suggested error range these values agree quite well with the brightness values obtained from the distribution peaks.

Interesting to note is the increase of the peak intensity around 700 nm with increasing shell-thickness. This peak was also observed in the bulk spectra and is attributed to the ${}^4F_{7/2} \rightarrow {}^4I_{13/2}$ transition [18]. We suggest that the ${}^4F_{7/2}$ level is either directly populated through a two-photon upconversion process without a relaxation step, or indirectly through a three-photon upconversion process with an additional multiphonon relaxation step. The transition from ${}^4F_{7/2}$ to another intermediate state (${}^4I_{13/2}$) is probably less favorable compared to a direct transition to the ground state. This would explain the observation that the peak around 700 nm is much more prominent in high power density (figure 4.10) spectra and that this peak appears only in our emission spectrum of single core/shell particles and not in the spectrum of single core-only particles (black). Saturating the energy levels in core-only particles takes much higher power densities as a result of the higher non-emission relaxation rates. Since our power density regime is in the non-saturating range, three-photon upconversion processes are less efficient for core-only particles (recall the slope of 2.20 in figure 4.8) in comparison with core/shell particles (slope of ~ 1.7 in figure 4.8). Transitions that require direct population without an additional relaxation step are very inefficient, but for core/shell particles, three-photon processes and direct population are suggested to be more efficient, leading to a probability increase for inefficient transitions such as ${}^4F_{7/2} \rightarrow {}^4I_{13/2}$.

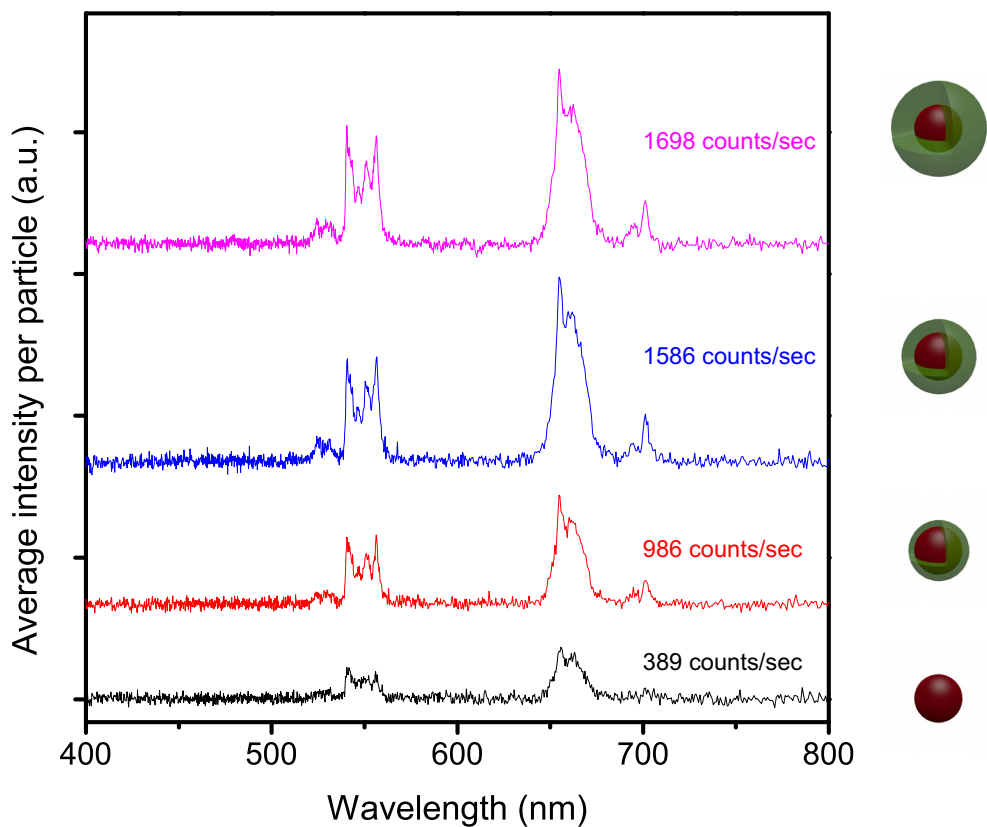


Figure 4.11: The average emission profile per particle, obtained by averaging the background subtracted emission spectrum for ~ 50 particles for each core/shell structure. An artificial offset is introduced to allow easy comparison. Integration time for each individual measurement is 20 seconds. An overlay representation of this graph can be found in Appendix C. The cartoons on the right correspond to the different core/shell structures: ANR10(1:0) (black), ANR71(1:2) (red), ANR73(1:3) (blue), ANR116(1:7) (magenta) in order of increasing shell thickness.

Chapter 5

Conclusions

The brightness of single core-only and single core/shell NaYF₄: Er³⁺, Yb³⁺ upconversion nanoparticles have been characterized. Long time trace recordings (200 seconds) on the emission of single particles showed no signs of photoblinking or photobleaching.

Many individual core-only and core/shell particles were characterized and showed a brightness increase for increasing shell thickness. Furthermore, a broadening was observed in the brightness distribution with increasing shell thickness. The higher brightness for core/shell particles as compared to core-only particles agrees with the results from other ensemble studies and is attributed to the efficient shielding of the active core by the passive shell, leading to lower phonon-electron coupling and thereby reducing the multiphonon relaxation rate. The broadening of the single particle brightness distribution with increasing shell thickness was observed for the distributions obtained at two different power densities. We conclude that this broadening is the result of dopants in the shell.

It was always assumed that the shell is completely passive (no ions present), but during the chemical synthesis of the shell, an additional form of Ostwald ripening might occur. During this additional Ostwald ripening process, a fraction of the small core particles also dissolve and mix with the dissolved shell material. The dissolved mixture of core and shell monomers re-crystallizes on the core to form the shell, but since the shell material is now mixed with dopants, this process results in the presence of dopants in the shell crystal. For longer incubation time with shell precursors, the shell grows thicker but the longer incubation time also results in stronger additional Ostwald ripening, leading to the presence of dopants in the shell. As a result, additional energy-migration pathways from the active core ions to the outer surface of the shell are formed. The uptake of dopants in the shell is a random process; a thicker shell leads to a broader distribution of dopants and broadens the single particle brightness distribution. This suggested mechanism would also be a reasonable explanation for the fact that upconversion nanoparticles in general still show very low quantum efficiency as compared to the bulk material despite growing large shells around the doped core.

It might be argued that the additional dopants in the shell also contribute to the brightness increase. However, the initial results on the power dependence of both ensemble samples and single particles showed a significant difference in power dependence between the core-only and core/shell particles in the investigated power range which indicates that the shell does in fact have a shielding effect. The power dependence can be described by $I \propto P^a$ where the value of a was determined from the slope of a double log representation of emission intensity I vs. excitation power density P .

The core-only particles showed a single power regime (single slope) in the investigated power range, whereas the core/shell particles showed two distinct regimes (two slopes). The presence of two slopes for core/shell particles is well explained in theory by intermediate energy level saturation. The fact that we observe saturation behavior for core/shell particles in our power regime and no saturation for core-only particles clearly indicates that the shell does have a significant shielding effect: the core/shell particles have a reduced quenching rate as compared to the core-only particles which results in a more efficient upconversion process in core/shell particles compared to core-only particles.

Emission spectra of ensemble and single particles were obtained. The typical high intensity peaks centered around ~ 520 nm, ~ 550 nm, and ~ 670 nm are clearly present in all measurements. However, the small peak around ~ 410 nm which is typically present in spectra of these type of particles was absent in all our measurements. The reason for the absence of this peak in our spectra is not very clear.

A peak around ~ 700 nm (attributed to the ${}^4F_{7/2} \rightarrow {}^4I_{13/2}$ transition [18]) was observed for high power density measurements and in spectra of single core/shell particles. For single core-only particles and low power density measurements on ensemble samples, this peak was very weak or even absent. Moreover, this peak is not consistently reported in studies on $\text{NaYF}_4: \text{Er}^{3+}, \text{Yb}^{3+}$ nanoparticles. Based on the observations from this study, the surrounding shell and power density appears to influence the efficiency of this transition. We suggest that the ${}^4F_{7/2}$ level is either directly populated through a two photon upconversion process without a relaxation step, or indirectly through a three photon upconversion process with an additional multiphonon relaxation step. Additional experiments are needed to further investigate the underlying process.

Chapter 6

Recommendations

The experiments presented in this report have shown the power of optically characterizing single upconversion nanoparticles with our setup and could lead to many new insights on the effectiveness of the core/shell structure.

The materials group that synthesizes the upconversion particles should look into the results and discussion of this report. These results show some new insights in the reasoning for the low brightness of the particles. We advise the materials group to look into alternative shell-synthesis methods that minimize the presence of dopants in the shell. This feedback is important for optimization of the synthesis process to ultimately produce small and bright upconversion nanoparticles that can be used as biological markers. Synthesizing efficient upconversion nanoparticles that are soluble in water is the ultimate goal. Therefore it is important to also characterize water soluble particles, since their optical behavior might vary from the oleic-acid based particles as a result of the different surface ligands.

Further investigating the emission spectra of individual particle could give new insights. An earlier study already indicated that the size of upconversion particles affects the green/red emission ratio as a result of phonon confinement, but the effect of the shell thickness has not been studied on a single particle level. The pilot experiments presented in this report show the rise of a peak at 700 nm in the emission spectrum with increasing shell thickness, which in itself is interesting enough to be studied further. It could be easily investigated to check if this transition is the result of either a two- or three-photon process by looking at the power dependence of a small emission band around 700 nm. Also the possible influence of the laser power density on the different peaks in the emission spectrum is interesting to look into.

We conclude that the broadening of the brightness distribution is caused by additional energy migration pathways caused by dopants present in the shell. This reasoning could be further validated by studying the lifetime behavior of single particles as this might lead to further insights in the quenching rates of the particles. In the current setup lifetimes of max 50 ns can be studied, which is multiple orders of magnitude too low to gain insight in the long lifetimes of the intermediate states in the energy scheme ($\sim \mu\text{s}$ to ms). A pulse picker could be used to gain more insight in these long lifetimes. An alternative option is using a diode laser in combination with a pulsed diode laser driver, which would be a more suitable option in terms of average power. If the broadening of the brightness distribution is really a result of additional non-relaxation pathways in the shell, then for increasing shell thickness there must be some correlation with the lifetime distribution.

Further experiments are needed to investigate heterogeneity of the power dependence behavior of single particles. The current method to determine the power dependence however is very time-consuming. A few adjustments to the setup and software could make these measurements much more time efficient. Furthermore it would be interesting to investigate the power dependence of the different energy transitions separately with additional emission filters.

The excitation in the current setup is 975 nm (50 nm width). By using a CW 976 nm diode laser with a clean up filter, a much narrower high power excitation line can be created, this might lead to more efficient upconversion and increase the experimental power density range. This adjustment would require setup and software adjustments, but it could be worth looking into if it results in more efficient upconversion. Additionally, power density comparison with other studies will be more straightforward since in most other studies a CW 975-980 nm diode laser is used.

Part II

Design and realization of a CW-STED super-resolution microscope setup

Introduction

Ever since the invention of the microscope, researchers have extensively studied biological structures and molecules on a microscopic level. With an increasing knowledge about these systems, we also learned that these microscopic systems are highly complex and therefore many biological processes are still poorly understood.

Over the last few decades fluorescence microscopy/spectroscopy techniques have become an increasingly popular choice for imaging, identifying and characterizing the microscopic mechanisms behind these biological processes. By labeling molecules under investigation with a suitable fluorophore, or by using fluorescent proteins, specificity and moreover high contrast can be obtained which allows non-invasive high quality microscopic imaging and single-molecule tracking. Although fluorescence microscopy allows high contrast imaging, its spatial resolution is, like all optical techniques, limited to the optical diffraction limit as theoretically stated by Abbe [27]. This limit is roughly equal to half of the excitation wavelength, which is about 200 nm for the smallest visible wavelength that can be used. This limit is still about one to two orders of magnitude larger than the size of single proteins, thereby making it very difficult to resolve very small structures or visualizing small scale processes like synaptic vesicle fusion [28, 29]. Basically, the diffraction limit makes it impossible to distinguish details in optically obtained images that are spatially separated within this limit. The Abbe equation shows that the use of a shorter wavelength or an increase in numerical aperture will decrease the spot size. In modern optics the numerical aperture is limited ($NA < 1.6$) as a result of the limited practical angular aperture and currently available immersion media. Decreasing the wavelength into the UV-range or even X-ray-range requires expensive materials. Moreover these short wavelength radiation techniques suffer from low contrast in biological samples and can cause damage to biological samples due to the high photon energy.

Alternative nanoscopic techniques such as Scanning Electron Microscopy (SEM) and Transmission Electron Microscopy (TEM) allow high resolution imaging with nanometer accuracy. However, these high resolution techniques are in general not suitable for living and dynamic samples. Atomic Force Microscopy (AFM) can be used for living samples, but is also limited to surface imaging. Therefore, biophysical researchers have focused on new nanoscopic techniques that are minimally invasive and are suited for studies in living cells and other dynamic systems while still allowing high spatial resolution imaging.

In order to profit from the advantages of optical microscopy, researchers have developed techniques to circumvent the diffraction limit. Some of these super resolution techniques, such as Photo-Activation Localization Microscopy (PALM) [30] and Stochastic Optical Reconstruction Microscopy (STORM) [31] make use of mathematical methods to localize the emitting center of single fluorophores and reconstruct

an image afterwards with a resolution far exceeding that of conventional fluorescence microscopy. Other techniques circumvent the diffraction limit in a physical manner. Some examples are Near-Field Scanning Optical Microscopy (NSOM) [32], 4- π Microscopy [33] and Stimulated Emission Depletion (STED) [34]. A combination of both physical and mathematical methods as in Structural Illumination Microscopy (SIM) [35] is also used. In 1994 Stefan Hell developed the theory of STED microscopy in which he showed that the diffraction limit in microscopy could be circumvented in a purely physical manner [34]. The technique Hell presented was based on effectively switching off (deplete) fluorophores in the outer region of the diffraction limited spot with the process of stimulated emission. Because of the characteristics of both fluorescence and stimulated emission, STED typically requires high laser intensities ($> 100 \text{ MW/cm}^2$), ps pulsed laser sources [34] and very precise spatial alignment of the STED and excitation focus. It was not until 1999 when Hell's group managed to successfully put the STED technique into practice for the first time [36]. Over the last decade much progress has been made and resolutions of up to 15 – 30 nm have been reported [37, 38] and have even resulted in an unprecedented all-physics optical resolution of 5.8 nm in crystal color centers [39]. Because of its high obtainable and tunable spatial resolution and relatively fast image acquisition, STED has shown to be one of the most promising optical super-resolution techniques. Furthermore, STED is not limited to specialized photoswitchable fluorophores and fluorophore labeling density in contrast to other high super-resolution techniques like STORM and PALM, which makes STED applicable to a wide range of dyes. The development of high power CW-laser sources have also lead to the development of CW-STED [40, 41], which does not require the tight pulse synchronization as was previously needed for pulsed-STED, thereby making the experimental realization of STED less complex. Additionally, since STED is an all-physics optical super-resolution technique, it can be applied in combination with other powerful fluorescent techniques such as fluorescent correlation spectroscopy (FCS) [42], which is impossible for super-resolution techniques based on computational reconstruction.

In this report the theory behind confocal fluorescence microscopy and STED microscopy will be introduced. Furthermore, the design of a custom built STED microscope setup and the practical difficulties of this setup will be described in detail. As there are many different ways to realize a STED setup, the choices made for the design of this specific setup are discussed in detail. Initial testing results and characterization of the setup are presented and discussed. The report concludes with some remarks and a future outlook on the realized setup.

Theory

This chapter presents some theoretical background on Stimulated Emission Depletion (STED) Microscopy. The first part of this chapter will introduce the basic principles of fluorescence, stimulated emission and the diffraction limit. The second part describes the basics of STED and how this principle can be used for super-resolution imaging.

8.1 Fluorescence and stimulated emission

The basic principle of fluorescence can be illustrated using a Jablonski diagram (Figure 8.1 (a)). A fluorescent molecule can be excited to a higher vibrational energy state (S_1^{vib} in Figure 8.1 (a)) with a light source. This excitation is most efficient at the optimal excitation wavelength of the fluorophore, which most often also corresponds to the absorption maximum. After this process of photon absorption, which happens almost instantly, the molecule quickly relaxes without radiation to the lowest vibrational energy level of S_1 . This state has a much longer lifetime (\sim ns) as compared to a vibrational state (\sim ps), which leads to the following transition to originate only from this state. During the next transition, the molecule falls back into the ground state (S_0) either by non-radiative decay or by spontaneous emission. In the first case

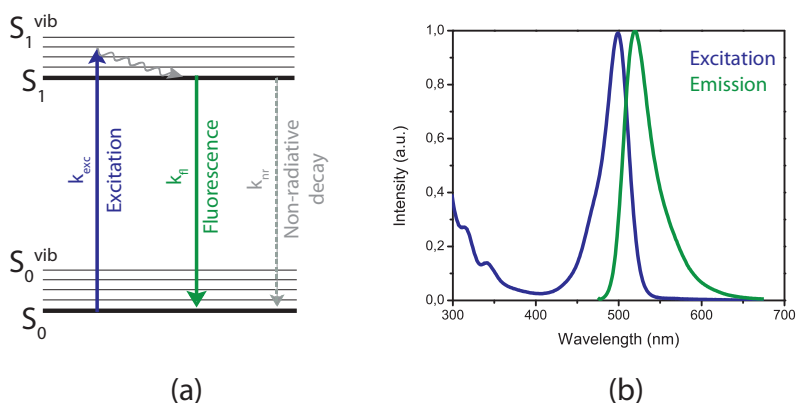


Figure 8.1: (a) Jablonski diagram illustrating the energy state transitions leading to fluorescence and non-radiative decay to the ground state. (b) Excitation and the red shifted emission profile of Alexa 488. Here it is clearly visible that the emission profile is red shifted and is similar to a mirrored version of the excitation profile.

energy is released in the form of heat, in the second by releasing energy in the form of a photon. Since energy has been lost during the process due to the vibrational relaxation step, the emitted fluorescent photon has a lower energy than the excitation photon which leads to a red shift of the emission profile relative to the excitation profile. Quantum mechanically the exact transition leading to fluorescence are not clearly defined, but is described by a transition probability. Together with various inhomogeneous and homogeneous broadening effects, the emission profile will have a broad continuous appearance and typically resembles a shifted mirrored version of the absorption profile (Figure 8.1 (b)).

Stimulated emission is an additional photon emission process and was theoretically discovered by Albert Einstein in 1917 [43]. In this case the atom or molecule in an excited energy state with energy gap $\Delta E = E_1 - E_0$ is stimulated to emit a photon with the same phase, frequency and polarization as an incident photon with an energy equal to the energy gap $\Delta E = h\nu$, where h is the Planck constant and ν is the frequency of the photon. The process of stimulated emission is also illustrated in figure 8.2. The rate of stimulated emission is given by $k_{st} = \sigma\Phi$, where Φ is the number of photons per area per time unit and σ is the stimulated emission cross section for the related transition. Since σ for fluorescent dyes are typically very small (in the order of 10^{-17} cm^2), this process is not very efficient. Relatively high intensities ($> 40 \text{ MW} \cdot \text{cm}^{-2}$) are needed to make the stimulated emission rate comparable to the spontaneous emission rate of $\sim 10^9 \text{ s}^{-1}$.

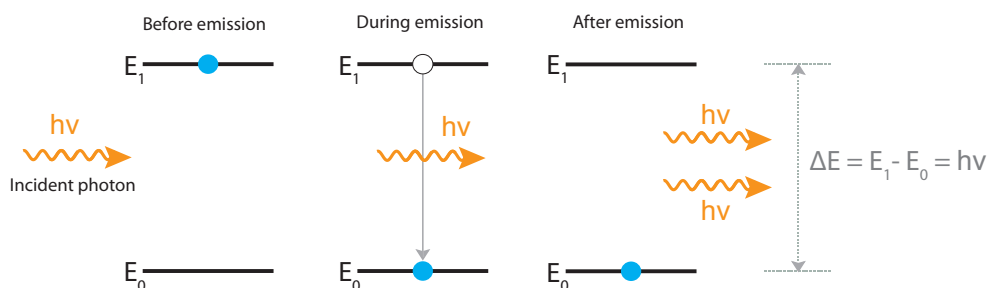


Figure 8.2: Diagram illustrating the process of stimulated emission from left to right. An atom in an excited state is stimulated to emit a photon by an incident photon. The stimulated emitted photon has the same phase, frequency and polarization as the incident photon. For simplification, non-radiative processes and vibrational energy states are not shown in this figure.

8.2 Diffraction limit

The resolution of optical microscopy is physically limited. This fundamental limit was first described by Ernst Karl Abbe in 1873 [27] and although no equations were mentioned in his paper, Abbe reported that the smallest resolvable distance between two points using a conventional microscope may never be smaller than half the wavelength of the imaging light. In some of his later papers he derived that as a result of diffraction, the imaging resolution was limited to half the wavelength λ modified by the refractive index n of the medium and the angle θ of the cone of focused light:

$$d = \frac{\lambda}{2n \sin \theta} = \frac{\lambda}{2NA} \quad (8.1)$$

The numerical aperture (NA) and the resolution limit is schematically illustrated in figure 8.3. The limit is basically a result of diffraction processes and the wave nature of light. The high frequency components that give an image its sharpness are lost by the finite numerical aperture of the lens that collects the light. This results in a blurry appearance of the captured image. In more mathematical sense it can also be said that the resulting image is a convolution of the actual object with the so-called point spread function (PSF) of the optical system. The PSF is the response of an optical system to a point emitter due to the diffraction limit and imperfections in the optical system. In a perfect optical system without any aberrations, the PSF is well-described by the so called Airy function. As a result of the diffraction limit, two emitting points cannot be optically resolved if the distance between them is smaller than the diffraction limit, which is illustrated in figure 8.3 (b).

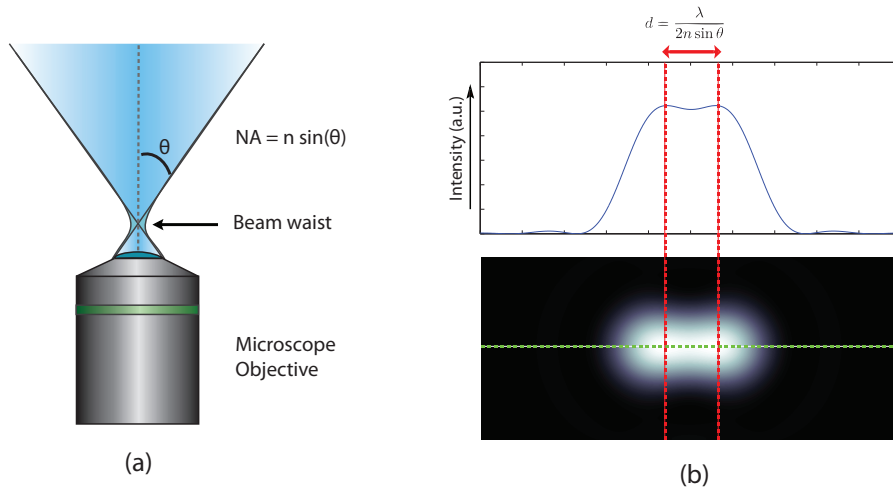


Figure 8.3: (a) Illustration of the numerical aperture (NA) of a microscope objective, (b) Two points are blurred by diffraction, which results in a limited resolution. The smallest resolvable distance between two points with an optical technique is limited by $d = \frac{\lambda}{2n \sin \theta}$.

8.3 Super-resolution imaging with Stimulated Emission Depletion

In the last two decades some very successful techniques have been developed to circumvent the first seemingly unbreakable diffraction limit. The most promising optical super resolution technique is based on the concept of stimulated emission depletion (STED) as first described in theory by Stefan Hell [34]. The idea presented in this paper is based on depleting fluorophores in the outer region of the diffraction limited spot with a second laser, the STED-laser, which has a red-shifted wavelength (λ_{STED}) and a small spatial offset with respect to the excitation laser. In the region where both lasers overlap, the fluorophores are excited by the excitation laser but are stimulated to emit at the wavelength of the second laser (λ_{STED}). If the stimulated emission rate is high enough, the fluorophores in the overlapping region will emit photons with wavelength λ_{STED} due to stimulated emission rather than emitting fluorescent photons with wavelength λ_{F} (spontaneous emission). The process of stimulated emission effectively depletes the fluorophores in the overlapping region leaving only the fluorophores in the non-overlapping region able to fluoresce. The fluorophores in the overlapping region are thus not switched into an 'off-state' by the STED beam, but are merely stimulated to emit photons with the same wavelength as the STED laser. The photons that arise from stimulated emission are suppressed in the emission path with an appropriate filter, while the fluorescent photons are able to reach the detector. This filtering ultimately leads to a size reduction of the effective fluorescent spot as is illustrated in figure 8.4 (b).

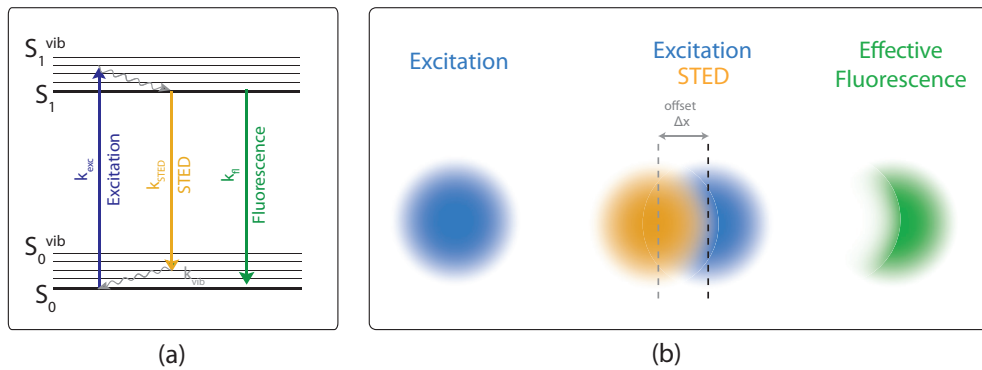


Figure 8.4: (a) Jablonski diagram illustrating the process of excitation, stimulated emission and fluorescence. (b) When two diffraction limited STED spots are overlapped with a diffraction limited excitation spot with offset Δx and when the STED intensity is high enough, the fluorophores in the outer region of the excitation spot are effectively depleted to the ground state by stimulated emission. In the region where there is no STED field present, the fluorophores are still able to fluoresce. As a result, the effective fluorescence spot is reduced to below the diffraction limit, but only in the direction of the offset.

8.3.1 STED beam shaping

The offset method as described in the previous section allows resolution increase only in the lateral direction of the offset. This limitation could be partially solved by using four offset beams. However, this requires either multiple STED lasers or splitting a single high intensity STED beam into four separate beams. Both options are experimentally challenging, since it requires very precise alignment of multiple beams. A more delicate solution would be to shape a single STED beam in such a way that it creates a symmetrical high intensity profile around a zero intensity center in the focus. This doughnut-like shape (figure 8.5 (c)) allows efficient and symmetrical confinement of the depleted region. To create a perfect null intensity in the focus of a high NA lens, it is quite intuitive that the phase front of the incoming beam must be shaped such that the focused light interferes destructively in the focus center. Over the last decade, different options have been implemented to create such a focal spot, and the development is still ongoing.

One way to create a perfect null intensity in the focus is by using an annular phase plate [44]. This plate consists of two rings, where the center ring is slightly thicker than the outer ring such that the light passing through the inner ring receives a phase shift of π with respect to the light passing through the outer ring (figure 8.5 (b) top figure). The two rings can be thought to create two different point spread functions in the focus [45]. The small inner ring has a small effective NA, and will therefore lead to a large PSF. The outer ring has a larger effective NA and will result in a smaller effective PSF. Because the latter has a phase shift of π with respect to the effective PSF created by the inner ring, the PSF created by the outer ring interferes destructively with the larger PSF and effectively creates a hole in the center of the focus. This principle of destructive interference will only work if the photon flux passing through the inner ring equals the photon flux through the outer ring, therefore the diameter of the inner ring is related to the STED beam diameter. Moreover, the polarization must be circular to make sure that the fields in all directions cancel out. With a MATLAB simulation (Appendix F) based on the equations given by Hao *et al.* [46], we can simulate the shape of the focus in multiple planes after phase modulation and with different polarizations. Simulation of different planes in the focal area with circular polarization and no phase modulation is shown in figure 8.5 (a). When the beam is phase modulated with an annular phase plate (figure 8.5 (b)), a doughnut-like shape will be formed in the YX-plane in the focus center. In ZX- and ZY-plane it can be observed that a hole is cut in the focus center as a result of destructive interference.

In 2004, Torok *et al.* [47] proposed that a doughnut-shaped focus can also be obtained from a class of vector beams called Gauss-Laguerre beams. The fundamental Gauss-Laguerre mode has a perfect doughnut shape after high NA lens focusing, and can be created by shaping a fundamental Gaussian mode with circular polarization and by spatially modifying the phase distribution. This phase distribution must have a helical shape and must be oriented properly with respect to the handedness of the circular polarization. This shape modification can be realized with a vortex phase plate (figure 8.5 (c) top figure), which is basically a thin helical ramped layer with varying thickness such that it leads to a spatial phase-adjustment of the beam as given by the vortex function:

$$A(r, \Phi) = e^{i\Phi}, \Phi = [0 \dots 2\pi] \quad (8.2)$$

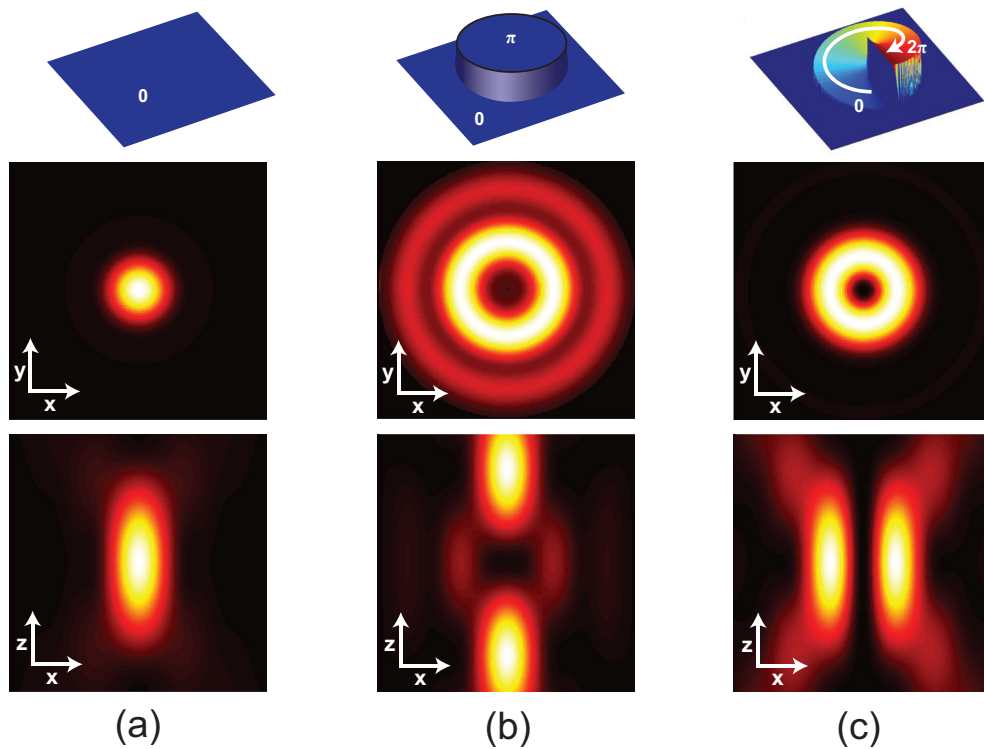


Figure 8.5: MATLAB simulation results of the normalized intensity in XY and XZ planes in the focus of the objective with perfect circularly polarized light. As a result of the symmetry, the ZY plane is similar to the ZX plane and is therefore not shown here. Black represents a normalized intensity of zero, while white represents a normalized intensity of one. The simulations are performed in a $800 \text{ nm} \times 800 \text{ nm}$ area for each plane with 10 nm step size. The top illustrations show the type of phase adjustment that was used. (a) When the incoming beam is not spatially phase-adjusted, the focus is a diffraction limited spot in XY plane and has a cigar shape in ZX and ZY planes. (b) When an annular phase plate is used to spatially adjust the phase of the beam, the focus in XY plane will have a doughnut shape. ZX and ZY plane will contain two cigars aligned in Z with a null intensity in the center. (c) A vortex phase plate will also lead to a doughnut in XY plane, but with much higher absolute intensity compared to the doughnut formed by the annular phase plate. In ZX and ZY plane the focus shows two cigar shapes aligned in respectively X and Y direction.

Simulations of the focus obtained with a vortex phase plate are presented in figure 8.5 (b). When comparing both the results of the annular and vortex phase plate, it can be seen that the lateral resolution would benefit from using a vortex phase plate, while the axial resolution would mostly benefit from using an annular phase plate. By using a combination of both types of phase plates, resolution in both lateral and axial directions can be increased. This however would require either two STED lasers, or splitting a single high power beam, phase adjust them separately and then recombine them before being directed into the microscope. These options are more challenging since it requires an additional path that needs to be aligned perfectly. Furthermore the additional optics leads to power loss. Despite these challenges, a combination of both an annular and vortex plate in a single setup have been demonstrated [48].

There are also alternative methods to obtain a suitable STED focus, such as using a spatial light modulator (SLM) or by using other types of phase-plates or phase modulators [45, 49]. However, the annular and vortex phase plates are most widely used in STED.

8.3.2 Obtainable resolution

Figure 8.6 illustrates how the overlap of a doughnut shaped STED beam leads to an increase in resolution. In this figure, two thin wire like structures are labeled with fluorophores and are in close vicinity of each other ($<$ diffraction limit). In conventional fluorescent microscopy the two wires cannot be spatially separated due to the diffraction limit as a large area of fluorophores is excited and therefore able to fluoresce. When STED is applied, the overlapping STED doughnut results in depletion of the fluorophores in the outer region of the excitation spot. This depletion results in a confinement of the area in which the fluorophores are still allowed to fluoresce. When the sample is raster scanned, the reduced size of the effective fluorescent spot enables the spatial separation of the two closely spaced wires in the resulting image.

The increase in spatial resolution is dependent on the STED excitation intensity and can be described mathematically. With a doughnut-shaped STED focus, the FWHM Δr of the effective fluorescent spot can be described by:

$$\Delta r \approx \frac{0.5\lambda}{n \sin \theta \sqrt{I_{\text{STED}}^{\text{max}}/I_{\text{sat}} + 1}} = \frac{\lambda}{2\text{NA}} \frac{1}{\sqrt{I_{\text{STED}}^{\text{max}}/I_{\text{sat}} + 1}} \quad (8.3)$$

Equation 8.3 is the familiar inverse square root intensity law for STED: the FWHM resolution approximately scales with the inverse square root of the STED intensity. The definition of Δr is also illustrated in figure 8.7. Also note that the first part of the right hand of equation 8.3 is the conventional diffraction limit (equation 8.1), i.e., when the STED intensity $I_{\text{STED}}^{\text{max}} = 0$ equation 8.3 reduces to Abbe's diffraction limit. The full derivation of this equation can be found in appendix D. In theory, the maximum obtainable resolution as stated by equation 8.3 would be infinitely small. In practice however, the extreme intensities required to reach extreme high resolutions would lead to unwanted effects such as photobleaching, optical trapping, multi-photon absorption, sample heating or even sample destruction. However the setup would most likely be practically limited due to stage drift or become dark noise limited due to the decreasing intensity that inevitably comes with increasing resolution. Moreover in the ultimate environment where STED is to be used, i.e. in biological samples, other processes such as diffusion play an important role. Lee and Boller [50] recently showed in a theoretical paper that there is a significant trade-off between the signal to noise ratio, which depends on the pixel dwell time, and the time it takes for a particle to diffuse out of the null of the STED doughnut. As a result they showed that STED resolution is most likely to be limited by diffusion processes in biological samples.

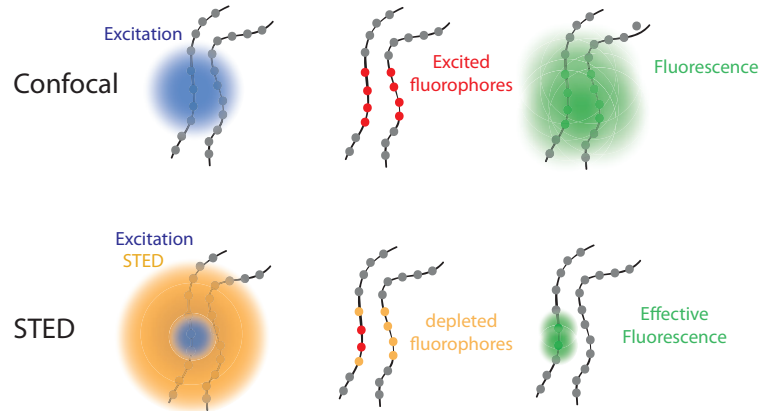


Figure 8.6: Cartoon illustrating the spatial resolution increase by STED. Two thin wire-like structures are labeled with fluorophores (gray dots). In conventional confocal microscopy most of the fluorophores in the focal region are excited (red) and are able to fluoresce, resulting in a large blob in the image. When STED is applied, a doughnut-shaped beam is overlapped with the excitation spot in the focal region. This leads to depletion of most of the excited fluorophores in the overlapping region (yellow dots), leaving only the fluorophores in the center of the doughnut to fluoresce (green).

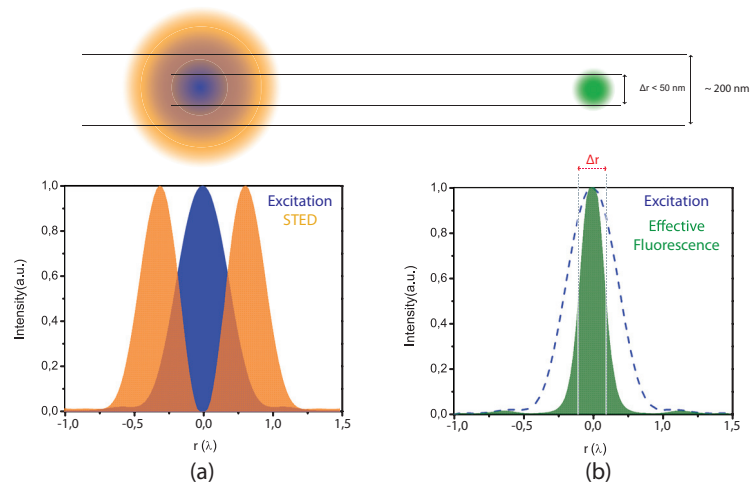


Figure 8.7: Top: overlapping a doughnut-shaped STED spot with a diffraction limited excitation spot will result in a confinement of the area in which fluorophores are able to fluoresce. Bottom: (a) Graph illustrating the overlap of the intensity of the STED donut shaped spot $I_{\text{STED}}(r)$ (orange) and excitation spot (blue) in one dimension. (b) Graph illustrating the decrease in the width of the effective fluorescence probability $h(r)$ (green) as a result of STED. Δr is the FWHM of the effective fluorescence probability (equation 8.3.)

Setup design

The objective of this project was to design and realize an easy-to-use, robust STED microscope for biophysical research done in the Nanbiophysics group. In this chapter, the design and the specific choices made to realize this setup will be discussed in detail. Furthermore, the main practical difficulties of realizing this setup are presented and discussed.

9.1 Fluorescence confocal microscopy

Biological systems are typically three dimensional structures. When the fluorophore labeled sample is flooded with excitation laser light like in conventional widefield microscopy, the resulting image is usually highly disturbed by out-of-focus fluorescent light. This leads to blurring of the image and results in a significant decrease in contrast. Confocal microscopy is a technique to reduce this unwanted out of focus light. In this technique, the excitation light is tightly focused in the sample. The emission light from the focus is collected by the same objective, after which it is focused through a small pinhole and directed towards a photodetector (Figure 9.1 (a)). The out of focus emission light will be largely blocked by the pinhole (Figure 9.1 (b)). The result of this method is that only the light from the focal volume is able to reach the detector. The drawback is that also light from other locations in the focal plane is blocked: confocal microscopy is pointwise excitation and pointwise detection. One solution is to raster scan the sample point by point to reconstruct a complete image in which only fluorescent signal from the focal plane is collected. This raster scanning can be repeated for different focal planes to section thick samples and reconstruct a 3D image of the sample.

STED is practically an extension of confocal microscopy. The STED beam needs to be focused in the sample to obtain the high intensity needed for stimulated emission, while pointwise detection reduces the out-of-focus light. To make STED work, the excitation focus center and STED intensity null of the doughnut shaped focus need to overlap perfectly. An image can then be obtained by raster scanning the sample, for example with a piezo scanning stage. The size of the pinhole used will determine the depth of focus of the microscope.

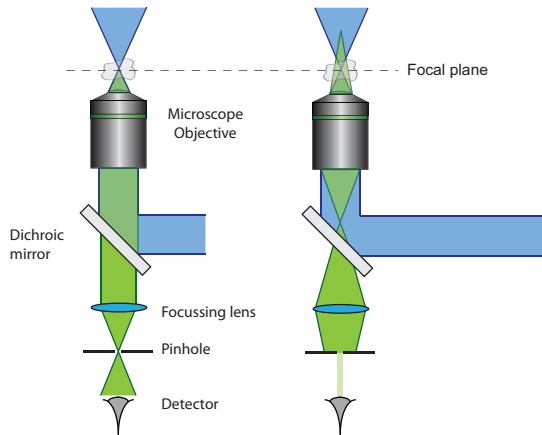


Figure 9.1: Illustration of the confocal microscope principle. A collimated beam of excitation light (blue) is tightly focused in the sample by a microscope objective. The left image shows that the emission light resulting from the focal spot will be focused through the pinhole and most light will reach the detector. The right hand side shows the case where the emitted light arises from a point that is located outside the focal volume. This light will not be focused through the pinhole and only a very small amount of light is able to reach the detector. As a result, the out of focus fluorescent light is mainly blocked by the pinhole and therefore the background signal is significantly reduced.

9.2 Pulsed STED vs. CW-STED

STED is most widely implemented with pulsed laser systems, but with recent advances efficient STED systems have been realized with CW laser sources as well [40, 41, 51, 52]. Pulsed STED requires tight synchronization of excitation and STED pulses. Furthermore the extremely short pulses emitted by most pulsed laser sources need to be stretched to make stimulated emission more efficient. Continuous wave STED does not suffer from these drawbacks, but it does require a higher average power laser source for efficient depletion compared with pulsed-STED.

The need for tight pulse synchronization can be illustrated with the use of a Jablonski diagram (Figure 9.2 a) and the rates at which different energy transitions occur. An excitation pulse excites fluorophores ($L_0 \rightarrow L_1$) after which the fluorophore quickly decays (\sim ps) to L_2 by vibrational relaxation. The STED pulse directly following the excitation pulse will induce the transition $L_2 \rightarrow L_3$ and thereby depletes L_2 by stimulated emission. In order to do this most efficiently, the time between the excitation and STED pulse Δt must be well tuned. In fact, depletion is most efficient when the STED pulse arrives directly after the excitation pulse has left, since in this case the level L_2 is not longer pumped and can be efficiently depleted by the STED pulse [34]. Furthermore, it is advantageous that the laser pulse durations are significantly shorter than the fluorescent lifetime, which is in the order of 2 ns. The STED pulse should be longer than the vibrational lifetime, $\tau_{\text{vib}} \sim 1-5$ ps, to avoid absorption back to L_2 by the same pulse. Therefore, pulses in the 100 ps range are typically used.

The effect of STED pulse duration t_s on the resolution increase can be derived mathematically. The derivation presented here is analogue to the derivation presented by

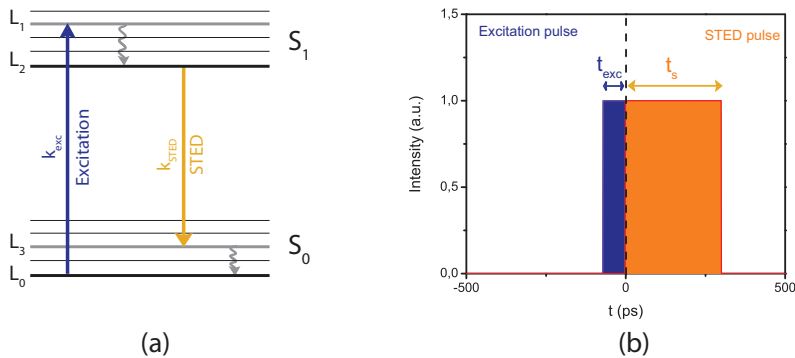


Figure 9.2: (a) Jablonski diagram illustrating stimulated emission. The fluorophore is pumped from L_0 to L_1 by the excitation pulse, after which it quickly relaxes to L_2 by vibrational relaxation. The fluorophore is then depleted to L_3 by the STED pulse. L_3 is then quickly depleted back to the ground state L_0 before re-absorption of another STED photon can take place. (b) Diagram illustrating the simplified temporal configuration of excitation and STED pulses. A rectangular excitation pulse with duration t_{exc} ends at $t = 0$ and is directly followed by a rectangular STED pulse with duration t_s .

Moffitt *et al.* [52]. We start with the simple case of a single rectangular excitation pulse that ends at $t = 0$ followed directly by a rectangular STED pulse starting at $t = 0$ as is illustrated in figure 9.2 (b). We can consider a total amount of fluorophores n_0 with stimulated emission cross-section σ and decay rate $k = 1/\tau_{\text{fl}}$, where τ_{fl} is the unstimulated fluorescent lifetime. Since excitation is absent after the excitation pulse, the total number of excited fluorophores $n(r, t)$ after $t = 0$ is decreasing due to fluorescence and stimulated emission, and can be described with the following differential equation:

$$\frac{dn(r, t)}{dt} = \begin{cases} -kn(r, t) - \sigma I(r)n(r, t) & 0 \leq t \leq t_s \\ -kn(r, t) & t > t_s \end{cases} \quad (9.1)$$

Where k is the fluorescent decay rate, $n(r, t)$ is the number of excited molecules, σ is the stimulated emission cross-section and $I(r)$ is the spatially dependent STED photon-flux (recall the doughnut shape). In equation 9.1, alternative non-radiative decay processes are neglected, since these will only change the amount of excited fluorophores and will leave the temporal dynamics unchanged [52].

For simplification the term $\sigma I(r)$ can be replaced with $K(r)$ which can be thought of as the stimulated emission rate coefficient which is dependent on the STED photon flux $I(r)$ at location r . This differential equation can be solved by integration, which gives us the number of excited molecules as a function of time:

$$n(r, t) = n_0 \begin{cases} e^{-(k+K(r))t} & 0 \leq t \leq t_s \\ e^{-K(r)t_s} e^{-kt} & t > t_s \end{cases} \quad (9.2)$$

The term $e^{-K(r)t_s}$ in the $t > t_s$ solution is a result of the fact that the number of excited molecules must be equal for both solutions at time $t = t_s$. The number of emitted fluorescent and stimulated photons will grow as time increases and can be expressed by the following equations:

$$\frac{dN_s(r, t)}{dt} = \begin{cases} \sigma I(r)n(r, t) & 0 \leq t \leq t_s \\ 0 & t > t_s \end{cases} \quad (9.3)$$

$$\frac{dN_f(r, t)}{dt} = kn(r, t) \quad (9.4)$$

With the solutions found for $n(r, t)$ (equation 9.2) we can again solve these equations by integration and by using the fact that $N_f = N_s = 0$ at $t = 0$. The total number of STED photons will first be solved:

$$N_s(r, t) = n_0 \begin{cases} \frac{K(r)}{k+K(r)} (1 - e^{-(k+K(r))t}) & 0 \leq t \leq t_s \\ \frac{K(r)}{k+K(r)} (1 - e^{-(k+K(r))t_s}) & t > t_s \end{cases} \quad (9.5)$$

The total number of fluorescent photons can now also be determined:

$$N_f(r, t) = n_0 \begin{cases} \frac{k}{k+K(r)} (1 - e^{-(k+K(r))t}) & 0 \leq t \leq t_s \\ \frac{k}{k+K(r)} + \frac{K(r)}{k+K(r)} e^{-(k+K(r))t_s} - e^{-K(r)t_s} e^{-kt} & t > t_s \end{cases} \quad (9.6)$$

To solve for the last equation, use was made of the fact that the total number of photons in time (fluorescent and stimulated emission photons) is related to the number of excited molecules by: $N_s + N_f = n_0 - n(r, t)$. When the STED intensity is zero, i.e. $I(r) \propto K(r) = 0$, equation 9.6 ($t > t_s$) reduces to $N_f = n_0 (1 - e^{-kt})$, in which e^{-kt} is the fluorescent lifetime. However, when the STED intensity is non-zero, i.e. $I(r) \propto K(r) \neq 0$, there will be a spatial dependence in the fluorescent lifetime ($e^{-K(r)t_s} e^{-kt}$) according to equation 9.6. This means that the presence of the STED light will influence the lifetime of the fluorophore. Hence there is also spatial information encoded in the lifetime signal of the fluorophores. This fact is actually used in recent developments to increase CW-STED resolution with time-gating (g-STED) [51, 52], but will not be further discussed in this report.

In this case we are only interested in the total number of photons originating from position r that arrive at the detector after a relative long time ($t \gg t_s$), since the detection time per pixel is much longer than the STED pulse duration. For this use we can take the infinite-time limit for equations 9.5 and 9.6:

$$\lim_{t \rightarrow \infty} N_s(r, t)/n_0 = \frac{K(r)}{k + K(r)} (1 - e^{-(k+K(r))t_s}) \quad (9.7)$$

and

$$\lim_{t \rightarrow \infty} N_f(r, t)/n_0 = \eta_{\text{STED}}(r) = \frac{k}{k + K(r)} + \frac{K(r)}{k + K(r)} e^{-(k+K(r))t_s} \quad (9.8)$$

The effective fluorescent spot $h_{\text{fl,eff}}(r)$ is described by the product of the spatial excitation probability $h_{\text{exc}}(r)$ with the spatially varying STED probability $\eta_{\text{STED}}(r)$:

$$h_{\text{fl,eff}}(r) = \eta_{\text{STED}}(r) h_{\text{exc}}(r) \quad (9.9)$$

The excitation probability $h_{\text{exc}}(r)$ can be described by:

$$h_{\text{exc}}(r) = \cos^2 \left(\frac{\pi r n \sin \theta}{\lambda_{\text{exc}}} \right), \quad (9.10)$$

The stimulated emission rate function $K(r)$ can be described by:

$$K(r) = k_{\text{STED}}^{\text{max}} \sin^2 \left(\frac{\pi r n \sin \theta}{\lambda_{\text{STED}}} \right) \quad (9.11)$$

Here $k_{\text{STED}}^{\text{max}} \equiv \sigma \Phi_{\text{max}} / t_s$, which is the peak STED depletion rate (number of photons per unit time) at the doughnut maximum. Here Φ_{max} stands for the number of STED photons per unit area at the doughnut maximum. With equation 9.9 simulations were performed to investigate the influence of the STED pulse duration on $h_{\text{fl,eff}}(r)$. The results of these simulations are shown in figure 9.3 (a). In this figure it can be clearly observed that an increasing STED pulse length will increase the effective spot size (FWHM). Consider a STED pulse repetition rate $f_{\text{rep}} = 1/t_r$ of 80 MHz, so that the pulses are spaced $t_r = 12.5$ ns apart. If we stretch the pulse length to 12.5 ns we effectively have a CW source. By keeping the number of photons within each pulse constant, the average power will also remain constant. However only the STED photons that fall within the fluorescent lifetime really attribute to stimulated emission [40]. If the fluorescent lifetime is 3 ns, only a fraction $\tau_{\text{fl}}/t_r \sim 1/4$ of the total amount of STED photons will attribute to depletion. To obtain a similar FWHM for the effective spot as for the pulsed case, the average power $P_{\text{avg}} \propto \Phi_{\text{max}}/t_r$, needs to be increased with a factor of 4. This is exactly what was simulated in figure 9.3 (b). When Φ was increased with a factor of four, the FWHM for the CW case was indeed almost similar to the 0.25 ns pulse case, which means a similar resolution. However, note that in the pulsed case the PSF intensity quickly reduces to zero at the base, whereas the CW PSF has a significant wider base. The FWHM of the cw-case can be further reduced by increasing the average power, however the PSF base will remain relatively broad as compared to the pulsed case.

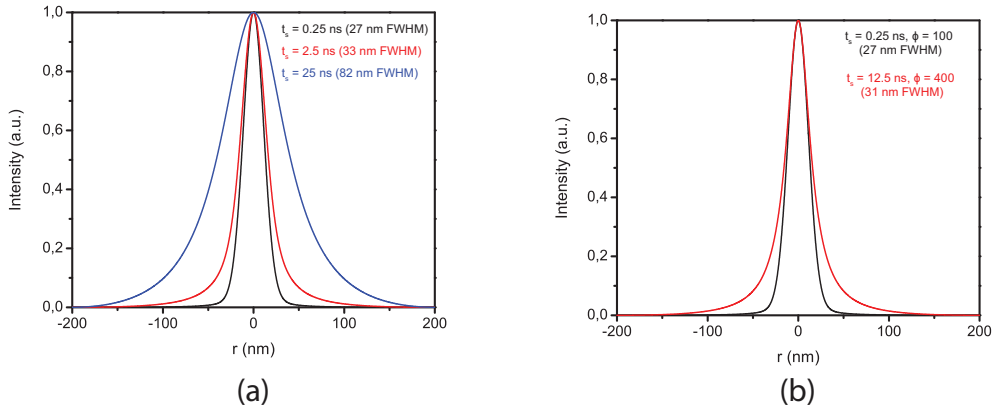


Figure 9.3: (a) Simulation results of the effect of STED pulse duration t_s on the effective fluorescent spot size $h_{\text{fl,eff}}$. When the STED pulse duration increases while the average power is kept constant, the effective spot size (FWHM) increases. Also notice that an increase in pulse duration leads to a broadening of the tails of the effective point spread function. (b) A remedy for the increasing spot size with increasing pulse duration is to increase the average power. The average power is here considered as the number of photons per pulse ϕ divided by the pulse repetition rate t_r .

9.3 Design

A schematic overview of the setup is presented in figure 9.4 and a more detailed overview is presented in Appendix E (figure E.1). The setup was built on an optical table (TMC, 780-series CleanTop II Table Top with Gimbal Piston Isolators) with pneumatic stabilization to provide damping of floor vibrations. A microscope body (aluminum) was built to provide a stable housing for the objective and piezo sample scanner. In order to discuss the design in a logical manner, this section is presented as a walk-through from excitation to detection.

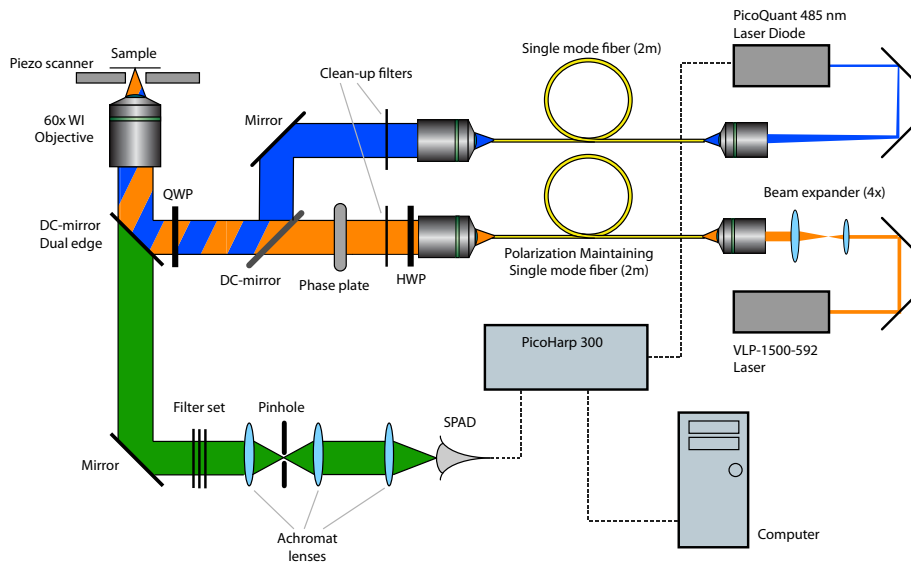


Figure 9.4: A schematic overview of the CW-STED setup. The excitation (blue) and STED (orange) light is coupled into separate single mode fibers and collimated after exiting the fibers. The STED beam is directed through a half-wave-plate (HWP), a vortex phase plate and a quarter-wave-plate (QWP) to create a fundamental Laguerre-Gaussian mode. The STED beam and excitation beam are overlapped with a dichroic (DC) mirror and directed into a microscope body where a water-immersion objective focuses both beams onto the sample. The emitted fluorescent light (green) is transmitted through a dual-edge dichroic. Out of focus fluorescence is reduced by focusing the emitted light through a pinhole. The resulting signal is obtained by focusing the light on the active area of a single photon avalanche diode (SPAD) and raster scanning the sample.

9.3.1 Laser source motivation

As discussed in the previous section, CW-STED is much easier to implement than pulsed STED, since it does not require tight pulse synchronization. However for CW-STED, the average power of the laser source needs to be ~ 4 times higher than the average power for the typical pulsed sources. The saturation power P_{sat} is given by [40]:

$$P_{\text{sat}} = A \frac{hc}{\lambda_{\text{STED}} \sigma \tau_{\text{fl}}} \quad (9.12)$$

Here A is the STED doughnut area, h the Planck constant, c the speed of light, λ_{STED} the STED wavelength, σ the stimulated emission cross section and τ_{fl} the fluorescent lifetime. For $\lambda_{\text{STED}} = 600$ nm and $\text{NA} = 1.2$, the doughnut area is approximately $A = 4 \times 10^{-9}$ cm². For typical fluorophores $\sigma = 3 \times 10^{-17}$ cm² and $\tau_{\text{fl}} = 3 \times 10^{-9}$ s. This leads to a saturation power of $P_{\text{sat}} = 14$ mW. A 5-fold resolution increase from the diffraction limit would be obtained if $P_{\text{STED}}^{\text{avg}} = 24P_{\text{sat}}$ (see equation 8.3), which shows that in this case an average power at the sample needs to be $P_{\text{STED}}^{\text{avg}} \sim 340$ mW. Considering the power losses in fiber coupling and in additional optics, high laser power sources (> 1 W) are therefore required to obtain efficient high resolution CW-STED. Fiber lasers are affordable, stable and high power CW laser sources (1 – 5 W) and are available at multiple wavelengths in the visible range. A pulsed 485 nm diode laser (LDH-P-C-485, PicoQuant) was already available in our lab and since a wide range of dyes are efficiently excited at 485 nm, we chose to use this laser for excitation. In literature it can be found that many suitable dyes that are efficiently excited around 485 nm, can be depleted with a ~ 590 nm STED wavelength. Table 9.1 shows an overview of dyes that have been successfully used for ~ 590 nm STED. Because of the easier implementation of CW-STED as compared to pulsed STED, a 1.5 W CW 592 nm fiber laser (VFL-P1500-592, MPBC, Canada) was purchased to provide the STED beam. This laser has high power stability, high degree of polarization (99%) and allows sufficient CW power.

Dye	Name	Company	Excitation peak	Emission peak
Alexa 488	Alexa Fluor 488 carboxylic acid SE	Invitrogen GmbH	500 nm	520 nm
Chromo 488	Chromo 488 NHS-Ester	Actif Motif Chromeon	488 nm	517 nm
Oregon Green 488	Oregon Green carboxylic acid	Invitrogen GmbH	498 nm	525 nm
FITC	Fluorescein-5-isothiocyanate	Invitrogen	496 nm	518 nm
DY-495	DY-495 NHS-ester	Dyomics GmbH	493 nm	521 nm
YFP	Yellow Fluorescent Protein	-	514 nm	527 nm
Citrine	Yellow Fluorescent Protein Mutant	-	516 nm	529 nm

Table 9.1: Excitation and emission wavelength peaks for fluorescent dyes that can be used for 485 nm excitation and 592 nm stimulated emission.

9.3.2 Fiber coupling and collimation

The excitation light is coupled into a single mode fiber (P1-460A-FC-2, Thorlabs) with a 10 \times microscope objective (10 \times Olympus Plan Achromat Objective, 0.25 NA),

while the STED light is coupled into a high power polarization maintaining single mode fiber (PMJ-3HPC-633-4/125-3AS-2-1-SP, OZ-Optics) with a same type 10 \times microscope objective. The single-mode fiber acts as a spatial filter and will produce a clean single-mode Gaussian beam behind the fiber. Before coupling the STED beam into the fiber, the tight beam (0.32 mm diameter) is expanded with a 4 \times beam expansion system (10 mm/40 mm lens combination) to increase incoupling efficiency (a wider beam can be focused to a smaller spot) which leads to a typical incoupling efficiency of $\sim 45\%$. For the STED beam, the fiber can be rotated around the optical axis at the incoupling site with a rotating mount. This is needed to align the slow-axis of the polarization maintaining fiber exactly with the polarization direction of the STED light to obtain a high polarization extinction ratio (PER). The PER is the ratio between the transmitted intensity of the unwanted polarization component and the transmitted intensity of the wanted polarization component through the fiber. The PER value can be checked by positioning a polarizer behind the fiber and measure the minimum power and maximum power transmitted through the polarizer by rotating the polarizer around its optical axis. We obtained a PER of 1:340 in our setup. The complete incoupling part of the setup has been boxed for safety purposes.

Both beams are collimated using a 4 \times microscope objective (4 \times Olympus Plan Achromat Objective, 0.10 NA). The outcoupler was mounted in an angle adjustment mount which was attached to a XYZ stage. This 5-axis adjustment is needed to assure that the beams pass exactly through the center of the collimation objective. The collimation objective was chosen such that the collimated beam width closely matches the back aperture of the microscope objective. A clean-up filter is used in both the excitation path (FF01-480/17-25, Semrock) and STED path (FF01-591/6-25, Semrock) to obtain a narrow laser line bandwidth.

9.3.3 Beam adjustment

The polarization direction of the STED beam can be adjusted with a half-wave plate (HWP) (Quartz for 589 nm, RZQ 2.15, B. Halle) in a rotation mount which is located directly after the collimation objective. The adjustment of polarization direction is needed to ensure correct polarization when the STED beam hits the dichroic later on. An additional half-wave plate can also be introduced in the excitation path to ensure maximal reflection at the beam-combining dichroic, but this is considered optional whereas for the STED beam this is mandatory for optimal polarization and minimizing power loss. The STED beam is directed through the center of a phase plate (VPP-1a - 596.5 nm - Vortex Phase Plate, RPC-Photonics). This phase plate gives the helical phase imprint for the beam. The position of the phase plate can be adjusted for X and Y direction to make sure the beam hits the phase plate on-center. In section 9.4 it is shown that the doughnut quality deteriorates when the phase plate is hit off-center.

The excitation beam is overlapped with the STED beam using a dichroic mirror (ZT532rdc, $\lambda/10$ RWD, Chroma). The overlapping beams passes through a quarter-wave plate (QWP) (Quartz for 589 nm, RZQ 4.15, B. Halle) which can be rotated around two axis to obtain perfect circular polarization for the STED beam. Simulations in section 9.4 show that correct circular polarization is important, since this largely determines the quality of the STED doughnut.

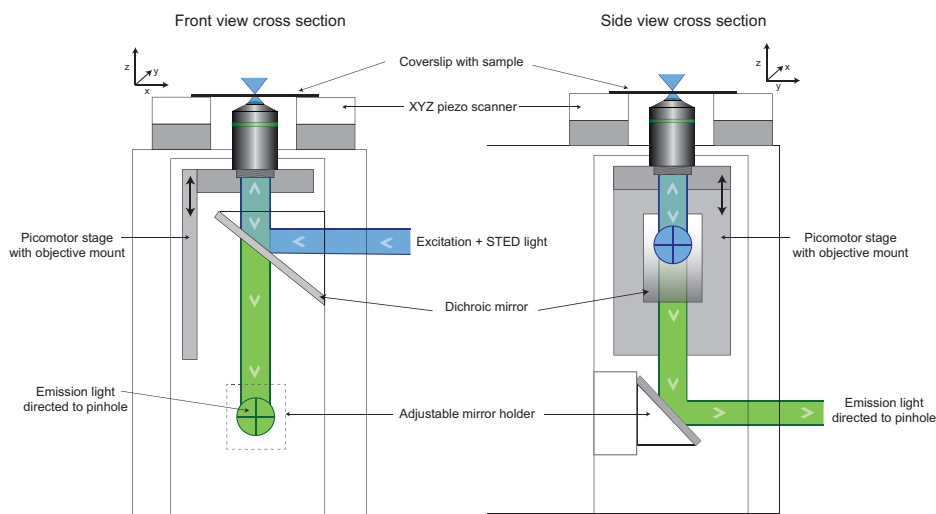


Figure 9.5: A schematic presentation of the inside of the microscope housing. Left: a cross section of the microscope as seen from the front. The dichroic reflects the excitation and STED light towards the objective which will focus the light at the sample. The emission light is collected by the same objective and is transmitted through the dichroic. Right: cross section of the microscope as seen from the light entrance side of the microscope. From this side it can be seen how the emission light is directed out of the microscope towards the pinhole.

9.3.4 Microscope body

Figure 9.5 gives a schematic representation of the inside of the custom built microscope housing. The excitation and STED beams can be directed into the microscope body with a set of two mirrors for each beam. The beams must be aligned perfectly with the optical axis of the objective in the microscope to prevent beam profile distortion. After entrance in the microscope body, the beams are reflected by a dual edge dichroic (zt488-491/594rdc, RWF of 0.08-0.17 peak-to-valley/inch, Chroma) into the back aperture of a microscope objective (60X water-immersion, 1.2 NA, Nikon) and focused onto the sample. A 3-axis piezo scanner (P-733.3CL, PI) is positioned on top of the microscope and is connected to a piezo stage controller (E-710.4CL, PI). The objective can be moved towards or away from the sample with a picomotor actuator (8302, Newport) which is controlled with a driver + hand terminal (iPico 8763-kit, iPico 8757, Newport). By moving the objective up and down with the picomotor, the z-position of the focus can be adjusted in a controlled and precise manner. The emitted light from the sample passes through the same objective as was used for excitation and is directed out of the microscope.

9.3.5 Emission path and detection

The emission light is focused through a pinhole ($15\ \mu\text{m}$) with a set of achromat lenses (50 mm, Thorlabs). The pinhole is mounted on a XYZ stage, so that the pinhole can be positioned exactly in the focal point of the two lenses. The light is then filtered

with a set of filters (NF03-488E-25, NF03-594E-25, LP02-488RS-25, Semrock) to suppress the reflected laser light and reduce other non-emission background light. The filtered emission light is ultimately focused onto the active area ($50\ \mu\text{m}$) of a Single Photon Avalanche Diode (MPD-5CTC SPAD, PicoQuant). The signal of the SPAD is routed through a 4-channel router (PHR 800, PicoQuant) and is analyzed with a Time Correlatated Single Photon Counting (TCSPC) module (PicoHarp 300 with TTTR hardware mode option, PicoQuant) in combination with SymPhoTime software (PicoQuant). The software also controls the piezo scanner via its controller, so that images can be obtained by raster scanning the sample and recording the photon counts for each pixel. The emission and detection path is completely boxed to reduce the detection of stray light to a minimum.

9.4 Practical difficulties

9.4.1 Dichroic flatness

One of the main problems we came across when building the setup concerned the dichroic mirrors. When dichroic mirrors are not of high quality (high flatness) or if the mirrors are under very light stress, the reflected wavefront will be distorted due to astigmatism. This distorted beam cannot be focused into a clean diffraction limited spot. The beam quality was checked with the use of a telescope (FR 500/65/14.7, Möller-Wedel), and the collimation was adjusted by adjusting the z-axis of the beam outcoupler. When a collimated beam is focused by a slightly curved lens or mirror, two distinct focal planes – called the tangential and sagittal planes – are existent (figure 9.6 (top row)). The focused spot in each plane is asymmetric, as if it is focused along only one axis of the plane, but is out of focus along the other axis. Between these two planes is a third plane that contains the smallest circular focused spot, commonly called the “circle of least confusion”. This spot is symmetric, but is larger than the spot that would be obtained in the absence of astigmatism in the focusing lens or mirror, thus resulting in blurring of the image. Furthermore, because the light is not nicely distributed into a diffraction limited focal volume, the laser power is not optimally used and additional background fluorescence can occur. Astigmatism is a result of the unwanted curvature of the dichroic mirror which can be induced by stress after the coating process, or due to artifacts on the the reflective surface. When the laser beam diameter is large, the effect of astigmatism will be larger, since the beam will hit a larger area on the dichroic surface. So one way to get around astigmatism is to reduce the beam width. In order to obtain a diffraction limited spot, which is an obvious requirement for obtaining high resolution, the beam width has to match the back aperture of the microscope objective, which is usually around 10 mm. By reducing the beam width, the resolution will also decrease. The large beam-width required to fill the back aperture of the imaging objective sets high flatness requirements on mirrors and dichroic mirrors in particular in our setup. To have a neglectable effect of astigmatism, a flatness of at least $\lambda/4$ over the beam area is required for the (dichroic) mirrors used in the setup. Additionally we found that the method of mounting the dichroic has a large effect on the reflected wavefront (RWF). A very small amount of stress already leads to significant RWF distortion, as was also the case in the top row of figure 9.6. When there is neglectable stress, the best focus spot is much smaller than in the astigmatism case and there are no tangential and sagittal planes present (bottom row in figure 9.6).

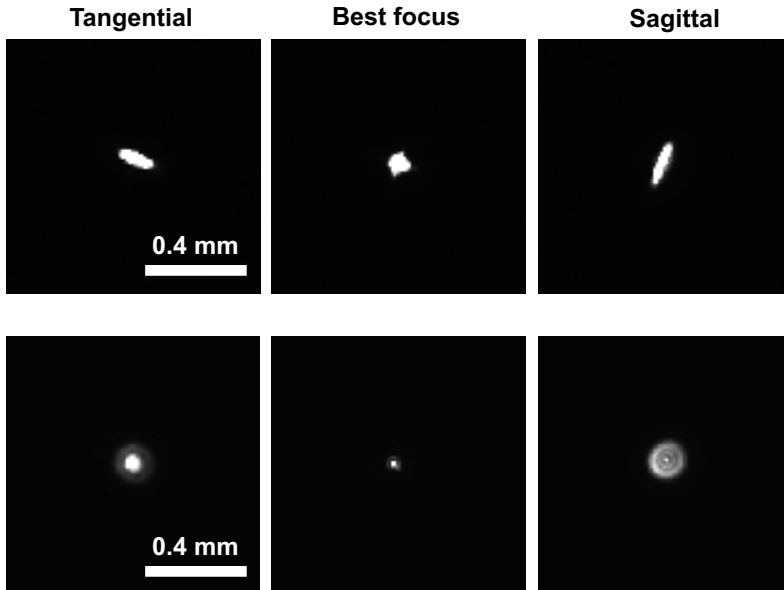


Figure 9.6: The different focal planes as a result of astigmatism resulting from a dichroic mirror mounted with induced surface stress (top row) and a high dichroic mirror mounted with no surface stress (bottom row). The images were obtained by focusing the reflected light from the dichroic mirror with a 200 mm lens onto the CCD chip of a beam-profiler (Thorlabs).

9.4.2 Polarization problems

To obtain a high quality STED doughnut in the focus, the polarization of the the STED beam needs to have perfect circular polarization of the correct handedness. Simulations based on the equations given by Hao *et al.* [46] were performed in MATLAB (Appendix F) to look into the effect of polarization on the quality of the STED focus. These simulations are presented in figure 9.7 and clearly show that when linear polarization is used without a phase plate, the focus is elongated in the polarization direction. The combination of linear polarization and a vortex plate results in a non-symmetrical doughnut with non-zero intensity at the center. When the circular polarization is of the wrong handedness, this will have a large effect on the doughnut quality: a high remaining intensity in the focus center is the result.

Investigating the quality of circular polarization can be a laborious task. For this reason a polarization-tool was constructed (figure 9.8). This device consists of a rotating polarizing prism that is driven by a rotation motor at ~ 3 Hz. The transmitted light reaches a photo-diode detector and its signal is visualized with an oscilloscope. This tool was put together with a cage construction and lens tubes so that it could be easily mounted in the objective holder. When the STED beam is not perfectly circularly polarized, the signal on the oscilloscope will oscillate with the rotation frequency of the polarizing prism. The half wave plate that is positioned directly after the collimation objective can be rotated around the optical axis in order to adjust for the polarization direction, which is important for hitting the beam combining dichroic on the correct axis. The quarter wave plate (QWP) will change the incoming linear polarized light into circular polarized light. In order to do so,

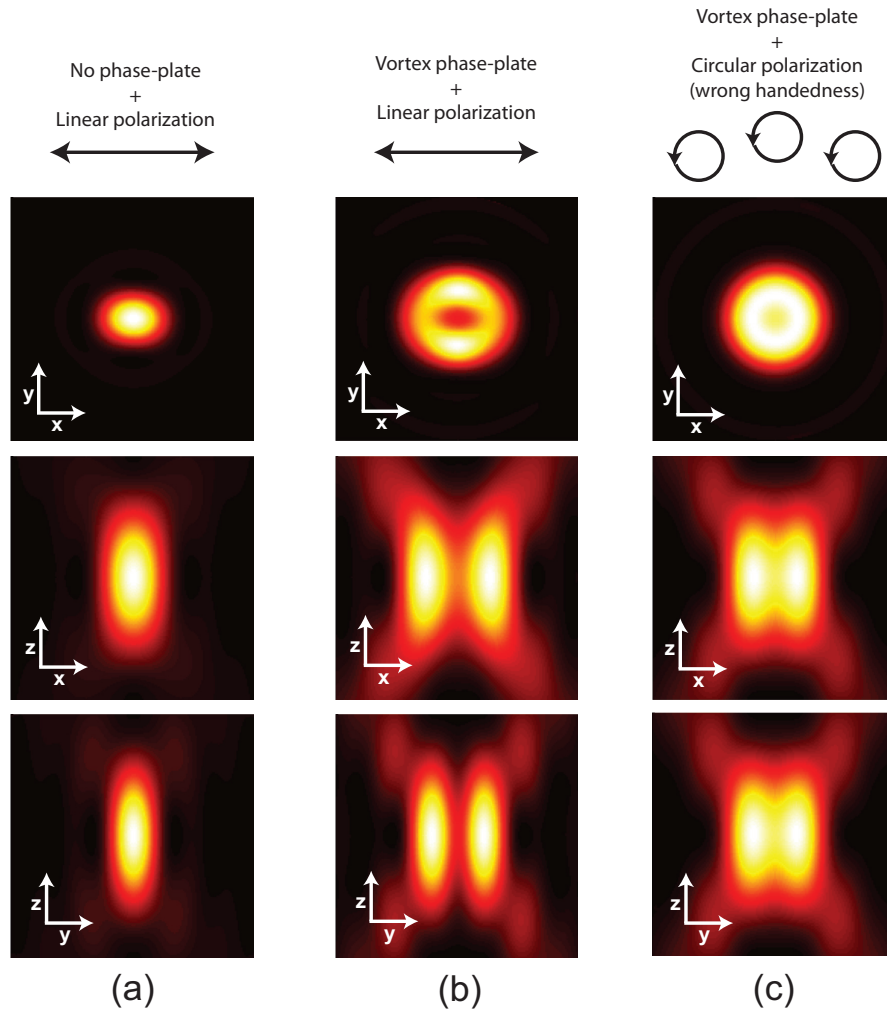


Figure 9.7: Simulation results of the effect of polarization on the focus spots. (a) No phase plate with linear polarization: the focus is elongated in the polarization direction. (b) A vortex phase plate with linear polarization results in a non-symmetrical doughnut with non-zero intensity at the center. (c) Wrong handedness of circular polarization results in a low quality but symmetrical doughnut with a high remaining intensity in the focus center. Simulated images are intensity normalized and have a size of $800 \text{ nm} \times 800 \text{ nm}$ with 10 nm pixel size. The parameters used for simulation are equal to our experimental parameters.

the direction of the linear polarization must agree with either the slow- or fast-axis of the QWP, depending on whether right-handed or left-handed circular polarization is needed (this depends on the vortex direction of the phase plate). The QWP is made for 589 nm , while our STED wavelength is 592 nm . We can correct for this small wavelength difference by adjusting the tilt of the quarter wave plate which will induce a slight difference in optical path length through the QWP. By slightly rotating the HWP, QWP and the tilt of the QWP iteratively, the signal appearing on the oscilloscope can be flattened. For perfect circular polarization the sum of the

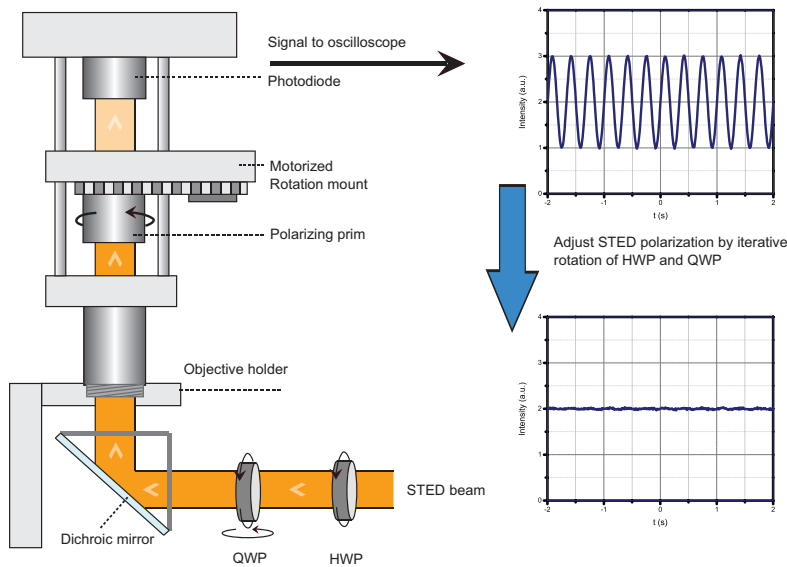


Figure 9.8: A polarization tool was built to efficiently check the degree of circular polarization. The tool could be easily mounted on the objective holder and basically consist of an automatic rotating polarization prism, with a photodiode detector which is read out by an oscilloscope. When the polarization is not perfectly circular, the detector will register a sinusoidal signal, since the the rotating prism blocks one polarization component, while transmitting the other component. The polarization of the STED beam is adjusted by iterative rotation of the tilt angle of the quarter-wave plate and rotation around the optical axis and by rotation of the half-wave plate. For perfect circularly polarized light, both polarization components are equal, and as a result the transmitted signal is flat.

transmitted horizontal and vertical polarization components through the prism are constant. As a result the rotating polarizing prism has no net effect on the transmitted intensity. Thus a completely flat signal (noise limited) indicates circular polarization. However, the polarization can still be of the wrong handedness. This can be checked by measuring the STED point spread function with a small point source (fluorescent nanobead, gold nanobead, quantum dot, etc.). When the handedness is correct, the minimum of the doughnut should only be a few % of the maximum intensity. For the wrong handedness, this intensity is much higher, which would result in depletion of fluorophores in the doughnut center. The handedness can be changed by rotating the QWP 90 degrees around the optical axis. Of course the quality of the circular polarization must be checked again and previous steps may have to be repeated.

9.4.3 Phase plate hit off-center

With the same simulation script as used for the polarization, we can also look into what happens when the vortex phase-plate is hit off-center. Since we are working with a relatively large beam size ($d \sim 10$ mm), the relative position of the phase plate center with respect to the beam center can be off tens of microns without noticing a significant change in the doughnut quality. However when the vortex plate is off-center with the beam in the order of ~ 500 μm , the doughnut quality deteriorates significantly. Figure 9.9 (a) and (b) show the simulation results of in the situation

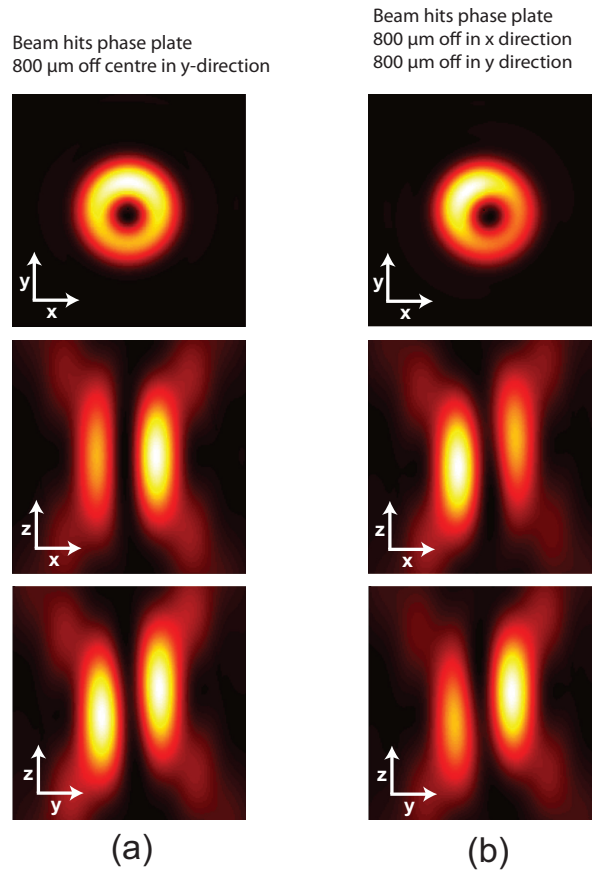


Figure 9.9: Simulation results of the spatial distribution of the STED focus intensity when the phase plate is hit off-center in one lateral direction (a), or in both lateral directions (b). Simulated images are intensity normalized and have a size of $800 \text{ nm} \times 800 \text{ nm}$ with 10 nm pixel size. The parameters used for the simulations are equal to our experimental parameters.

where the vortex plate is hit off-center $800 \mu\text{m}$ in X direction and $800 \mu\text{m}$ in both X and Y direction respectively. When the phase plate is hit off center in only one direction (X or Y), the cross section (ZX or ZY) shows a relative shift in Z of the two cigar shapes. The other cross section is still aligned in Z, but the relative intensities of both cigars are different. This intensity shift towards one direction in the doughnut is also clearly visible in the XY cross-section. When the phase plate is hit off center in both X and Y, the cigars show a combination of a difference in intensity and a relative shift in Z. This occurs for both ZX and ZY cross-sections. In our setup we can tune the XY position of the phase plate with an XY stage. The only way to check the quality of the doughnut focus is to measure the point spread function (PSF) in the different planes (XY, ZX and ZY) with small gold nanobeads or nanorods. The quality of the doughnut can then be tuned by iteratively adjusting the X and Y position of the phase plate.

Chapter 10

Setup characterization

Fluorescent nanobeads are ideal for initial testing of the setup and obtainable resolution. Figure 10.1 (a) shows the image obtained for a sample with single 20 nm yellow-green fluorescent beads. The diffraction limited image of three beads are clearly visible. Figure (b) presents an intensity profile of a diffraction limited spot in the image, presenting a FWHM (obtained from Gaussian fit) of ~ 300 nm. This is slightly larger than the diffraction limit expected for our experimental conditions. This is most likely due to the active area of the detector being slightly out-of-focus.

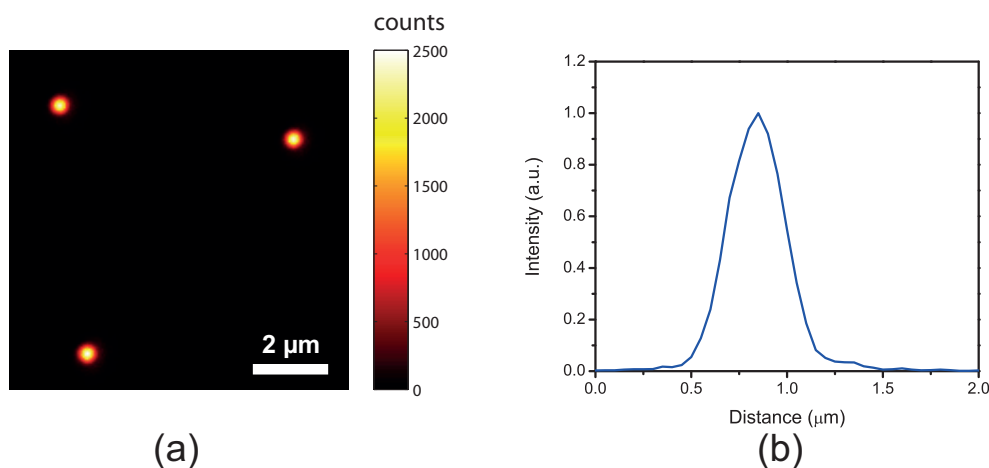


Figure 10.1: (a) Image showing three 20 nm yellow-green fluorescent beads imaged with the excitation beam. (b) A cross section of a spot in the image.

The next step in characterizing the setup is to show single-emitter sensitivity. This was done by imaging a sample of single quantum dots (Carboxyl-Functionalized eFluor® 650NC) on a coverslip. Samples were prepared by diluting the quantum dots (Carboxyl-Functionalized eFluor® 650NC, eBioscience) from stock solution to a concentration of 0.2 nM in 2% Polyvinyl Alcohol (PVA) solution. 50 μ l of the solution was spin-coated at 6000 rpm on a clean glass coverslip. The glass coverslip was cleaned in nitric-acid (65%) and extensively rinsed with HPLC grade water and subsequently with HPLC grade methanol and passively dried before spin-coating.

Figure 10.2 (a) shows an image that was obtained by scanning a sample with single quantum dots. The sample was scanned by the STED beam without the vortex phase plate (orange) and subsequently by the excitation beam (blue). Both individually obtained images were overlapped to compare the positions of the single quantum dots in the images. Figure 10.2 (b) shows the intensity profile along the dotted line and shows that the intensity peaks from the three quantum dots along the line overlap quite well, thereby demonstrating that with this initial alignment, the focus of the excitation beam can be overlapped with the STED focus with an accuracy of at least 200 nm, which is the the distance between two pixels in this image.

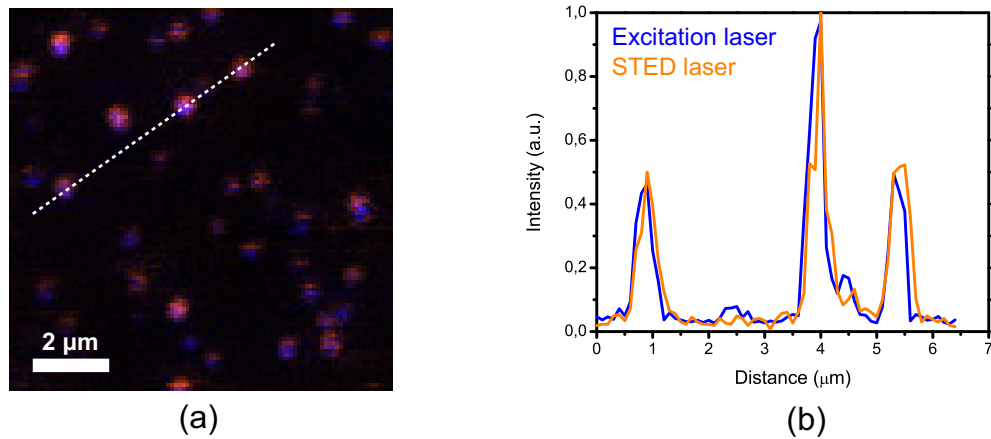


Figure 10.2: (a) Raster scanned image of a sample with single quantum dots, subsequently scanned by the STED beam without the vortex phase plate (orange) and the excitation beam (blue). For positional comparison, both images were artificially colored and overlapped, (b) The profile along the dotted line shows that the three quantum dots along the line are at the same location in the STED and excitation image with an accuracy of at least 200 nm.

By introducing the vortex phase plate in the STED beam-path, we can create a doughnut in the STED focus. For this purpose, the correct vortex ($0 \rightarrow 2\pi$ for 596.5 nm) on the plate was located and positioned such that its center aligned with the STED beam center. Directly behind the vortex plate, a small singularity in the the beam profile could be observed by eye. By adjusting the X/Y position of the phase plate, this singularity was directed to the approximate center of the beam. Almost perfect circular polarization was obtained with the method presented in section 9.4.2. By looking at the beam profile (highly attenuated) through the telescope after reflection by the dichroic mirror in the microscope, the singularity in the beam profile could be observed more clearly. By slightly adjusting the X/Y position of the phase plate, the position of the singularity can be directed to the center of the beam in a precise manner.

When observing the reflection of the laser beams from the upper surface of a glass coverslip, the relative positions of the excitation and STED focus could determined. The position of the excitation focus was slightly adjusted by fine-tuning the two angles of the beam-combining dichroic mirror directly in front of the microscope. The position was adjusted such that the the reflected excitation spot overlapped with the null-intensity of the STED doughnut. In the next step, a sample with single quantum dots was scanned with the excitation beam and subsequently with the phase-shaped

STED beam to determine if the focus of both beams were overlapping correctly. The result of three averaged scans on a single quantum dot is shown in figure 10.3, where (a) presents the overlapped images and (b) presents the intensity profile cross section of the quantum dot image. Both the scan image and the intensity profile show that the excitation maximum overlaps quite well with the doughnut minimum. This demonstrates that the designed setup allows relative easy overlapping alignment of the STED and excitation focus.

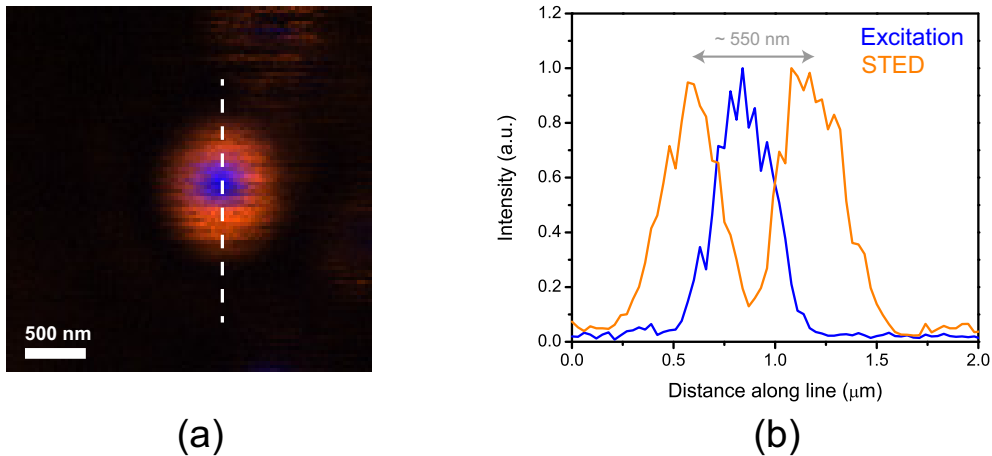


Figure 10.3: (a) Overlay of a single quantum dot image obtained with the phase-shaped STED beam (orange) and excitation beam (blue). To reduce photobleaching artifacts, the image shown here is obtained by scanning the quantum dot three times with the STED beam and subsequently three times with the excitation beam, (b) the normalized intensity profile along the dotted line shows that the null of the STED doughnut overlaps well with the excitation maximum.

Due to photobleaching, it is a very difficult task to optimize the STED doughnut on single quantum dots. Therefore we switched to use gold-nanorods (GNR's) drop-casted on the surface of a coverslip. These particles cannot bleach or blink, since the emission is based on surface plasmon resonance scattering and are therefore ideal emitters to obtain nice point-spread functions. A typical image obtained from the gold-nanorod sample is shown in figure 10.4 (a), where the two top images are obtained by scanning the same region subsequently with the excitation and STED beam. The larger image shows an overlay image of these two. Interesting to note is that some nanorods are only imaged by the excitation beam (blue), but not by the STED beam (orange). This is probably the result of these particles being off-resonance with the STED wavelength as a result of the different particle size. The spots obtained with the excitation beam showed a FWHM of ~ 280 nm, demonstrating the diffraction limit of the confocal detection modus. The image in figure 10.4 (a) shows that the excitation spots are slightly off-center with the STED doughnuts. This shift can be observed even more clearly in figure 10.4 (b), where the intensity profile along line 1 is shown. The intensity profile along line 2 (figure 10.4 (c)) shows that the excitation and STED doughnuts are almost perfectly aligned in the vertical direction of the image. The STED doughnut intensity profiles show a remaining intensity of $\sim 5\%$ in the doughnut center. Note that the doughnut intensity profiles show a higher intensity

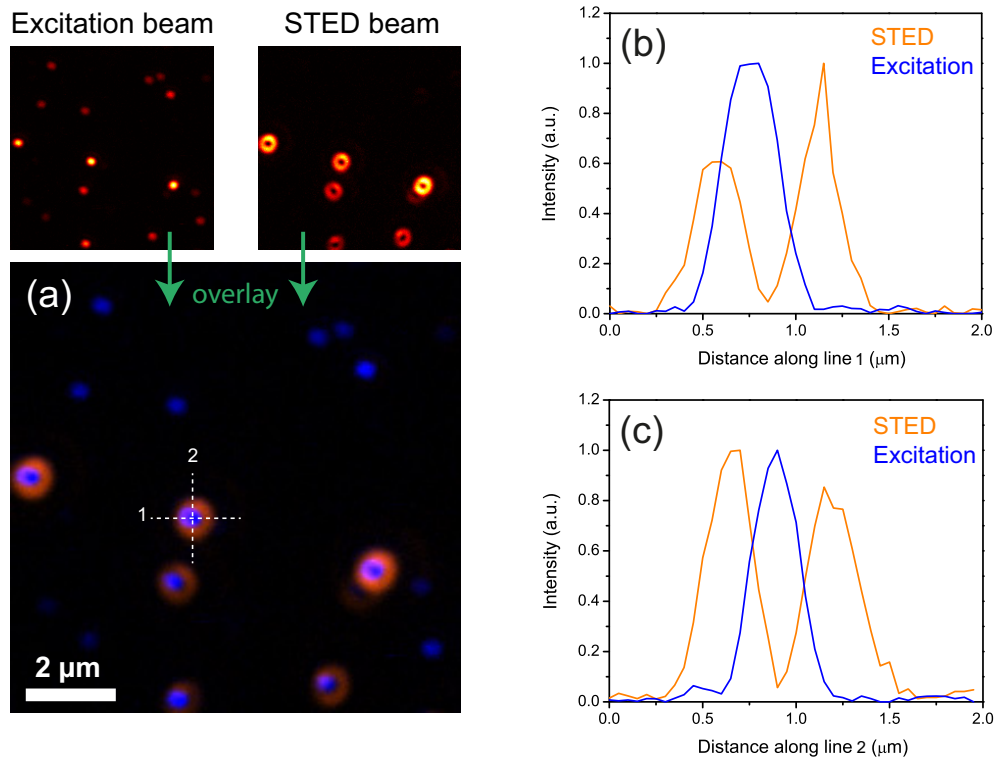


Figure 10.4: (a) An overlay image of a gold nanorod sample scanned subsequently with the excitation beam (blue) and STED beam (orange). The top images present the channels separately, (b) Intensity profile (background-subtracted and normalized) along line 1 in (a). Clearly visible is the shift of the excitation PSF with respect to the STED doughnut-PSF in this direction and the intensity difference between the two peaks in the STED doughnut, (c) Intensity profile (background-subtracted and normalized) along line 2 in (a). In this direction the excitation and STED PSF's overlap much better. Again notice the intensity difference of the STED doughnut peaks.

on one side of the doughnut. This is probably the result of a slight misalignment of the vortex phase plate (also see section 9.4.3). The doughnut quality can be tuned by adjusting the X and/or Y position of the phase plate as is illustrated in figure 10.5 (a). In this figure, the STED beam initially hits the vortex completely off-center in X and Y direction. The doughnut is again optimized by adjusting the phase-plate position iteratively. Note that the type of distortion caused by the phase-plate misalignment agrees well with the simulations shown in section 9.4.3.

Figure 10.5 (b) shows two optimized STED doughnuts. The distance between the two intensity peaks of the STED doughnut is about 500 nm. The simulations shown in section 8.3.1 were obtained with similar experimental parameters, and showed a peak-to-peak distance of ~ 415 nm. Considering that the latter is in the ideal situation with the microscope objective as the only optics, the experimentally obtained peak-to-peak distance in the STED point-spread functions seems to be quite good. The remaining 5% at the doughnut-null is probably due to some small polarization imperfections.

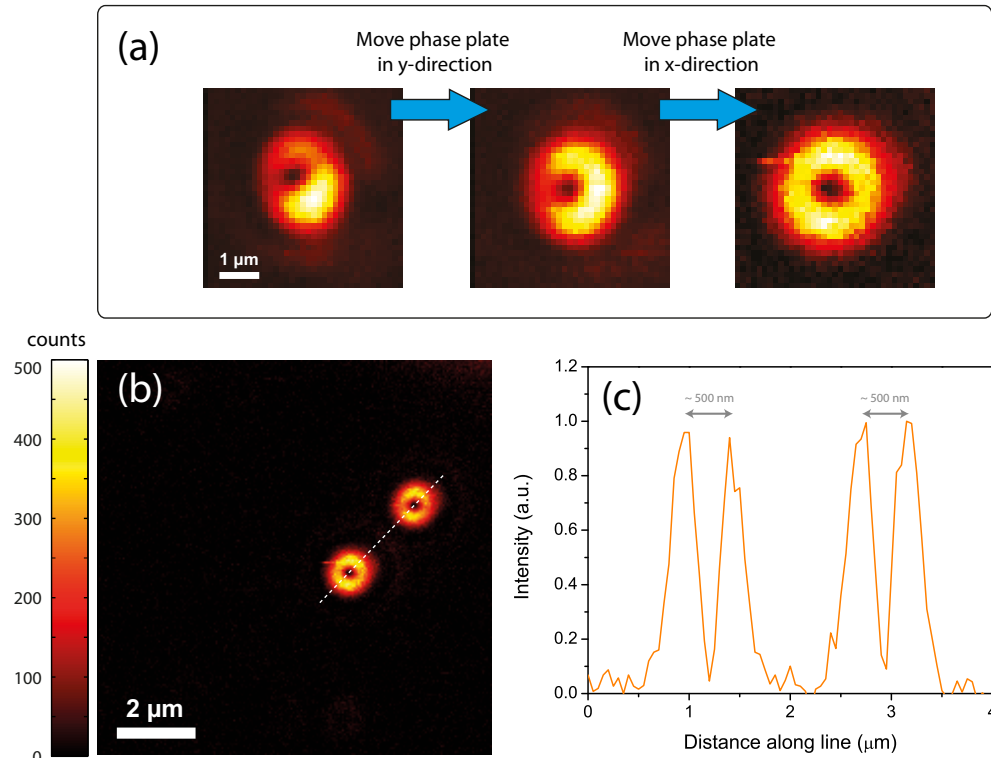


Figure 10.5: This figure demonstrates the capability of doughnut quality optimization with the setup. (a) If the phase plate is misaligned in both x- and y-direction, the doughnut obtained by scanning a gold-nanorod shows a high intensity blob in a diagonal direction of the doughnut image. By moving the phase plate in the correct direction (here mentioned as y), the high intensity blob can be positioned to the side of the doughnut and by subsequently moving the phase plate in the complementary direction (in this example called x), the doughnut shape can be further optimized. Note that x and y are used arbitrarily here. (b) Image of two gold-nanorods, obtained with an optimized STED beam, (c) the intensity profile (background-subtracted and normalized) along the dotted line in (b) shows that the doughnuts are of high quality with $\sim 5\%$ remaining intensity in the doughnut-center.

Chapter 11

Conclusions

The objective of this project was to design and realize an easy-to-use and robust single molecule sensitive microscope setup with additional Stimulated Emission Depletion (STED) super-resolution capability.

The designed and realized setup allows imaging through raster scanning a sample and collecting the fluorescent signal pixel-by-pixel with a Single Photon Avalanche Diode. Imaging and signal acquisition is performed by sensitive hardware to allow single molecule sensitivity, while the easy-to-use commercially available software allows easy image acquisition, time-trace, lifetime, and FCS measurements and analysis. Moreover, the designed setup allows easy and robust alignment through the implementation of highly stable adjustment mounts and stages, while the high quality optics ensure high beam profile quality throughout the setup.

By imaging small fluorescent beads and gold-nanorods, the obtainable resolution in confocal-mode was shown to be diffraction limited (~ 280 nm FWHM). By imaging single quantum dots it was shown that the designed setup is single-emitter sensitive.

Simulations showed that incorrect polarization has a large effect on the doughnut quality. For this reason, the setup allows efficient polarization fine-tuning to obtain the high degree of circular polarization that is needed for STED.

Incorrect alignment of the vortex phase plate leads to significant distortion of the STED doughnut. The distortion observed experimentally agrees well with simulations performed in MATLAB. In the realized setup the doughnut quality can be optimized by adjusting the X/Y position of the phase plate. By imaging a single quantum-dot and single gold-nanorods with the phase-shaped STED beam, it was shown that a high quality doughnut shaped STED PSF can be obtained. The excitation PSF can be initially aligned with the intensity-null of the STED doughnut PSF with an accuracy of at least ~ 100 nm, but can be improved by fine-tuning the direction of excitation beam entering the microscope.

Chapter 12

Future outlook

The next step in characterizing the setup is measuring the PSF of the STED doughnut and excitation in the Z-plane and optimizing these. Z-alignment of both PSF's is important to obtain efficient super-resolution. Furthermore, the stability of the overlap-alignment needs to be checked, since correct overlapping of excitation and STED PSF's is crucial for obtaining super-resolution. Small fluorescent beads (20 nm) that are efficiently excited at 485 nm are suggested for the initial testing of super-resolution.

When completely optimized, the designed setup should be able to reach an imaging resolution of ~ 40 nm in the lateral plane. Resolution along the optical use could also be increased with the use of an annular phase plate as is discussed in section 8.3.1. The setup can be extended with time-gated STED (g-STED) [51, 52] to obtain even higher resolution imaging or to reduce the average STED power while maintaining similar resolution.

The setup design also allows Fluorescent Correlation Spectroscopy (FCS) measurements. In combination with STED, this type of setup is a powerful tool in diffusion characterization of single proteins as was shown by Eggeling *et al.* [42].

Additionally, since the designed microscope setup contains two lasers, the setup could also be used for Fluorescence Cross-Correlation Spectroscopy (FCCS). In this technique, one laser excites one type of fluorophore in the sample, while the second laser excites a second. An additional dichroic mirror placed in the emission path can split the two emission channels which can then be directed towards two separate detectors. These two emission channels can be cross-correlated with the TCSPC module and SymPhoTime software, which leads to insights on the diffusion correlation between the two fluorescently labeled species in the sample. Alternatively, the second detector could be used for antibunching experiments.

Part III
Appendices

Appendix A

Symbols and abbreviations

AFM	Atomic Force Microscopy
CW	Continuous Wave
DLS	Dynamic Light Scattering
FCCS	Fluorescence Cross-Correlation Spectroscopy
FCS	Fluorescence Correlation Spectroscopy
FLIP	Fluorescent Loss In Photobleaching
FRAP	Fluorescent Recovery After Photobleaching
FWHM	Full Width Half Maximum
GNR	Gold Nanorods
g-STED	Time gated STED
HWP	Half Wave Plate
NA	Numerical Aperture
ND	Neutral Density
NSOM	Near-Field Scanning Optical Microscopy
PALM	Photo-Activation Localization Microscopy
PER	Polarization Extinction Ratio
PSF	Point Spread Function
PVA	Polyvinyl Alcohol
QWP	Quarter Wave Plate
RWF	Reflected Wavefront (distortion)
SEM	Scanning Electron Microscopy
SIM	Structured Illumination Microscopy
SPAD	Single Photon Avalanche Diode
STED	Stimulated Emission Depletion
STORM	Stochastic Optical Reconstruction Microscopy
TCSPC	Time Correlated Single Photon Counting
TEM	Transmission Electron Microscopy
YFP	Yellow Fluorescent Protein

R_{MPR}	=	multiphonon relaxation rate (s^{-1})
C	=	host characteristic constant
β	=	host characteristic constant
p	=	number of phonons
$\hbar\omega_{\text{max}}$	=	effective vibrational mode (cm^{-1})
ΔE	=	energy gap (cm^{-1})
I	=	emission intensity (W/cm^{-2})
P	=	excitation power (W)
i	=	number of photons in upconversion process
w_0	=	focus spot radius (m)
λ	=	excitation wavelength (m)
n	=	refractive index
h	=	Planck constant ($6.626068 \times 10^{-34} \text{ m}^2 \cdot \text{kg}/\text{s}$)
ν	=	photon frequency (s^{-1})
k_{st}	=	stimulated emission rate (s^{-1})
σ	=	stimulated emission cross section (cm^2)
ϕ	=	number of photons per area per unit time ($\text{cm}^{-2} \cdot \text{s}^{-1}$)
λ_{STED}	=	STED wavelength (m)
λ_{fl}	=	fluorescent wavelength (m)
$I_{\text{STED}}^{\text{max}}$	=	STED intensity at doughnut maximum (W/cm^2)
I_{sat}	=	STED saturation intensity (W/cm^2)
k	=	fluorescent decay rate (s^{-1})
τ_{fl}	=	fluorescence lifetime (s)
n_0	=	total number of excited fluorophores
$n(r, t)$	=	number of excited fluorophores at position r and time t
t_s	=	STED pulse duration (s)
$I(r)$	=	spatially dependent STED photon flux ($\text{s}^{-1} \cdot \text{cm}^{-2}$)
$k(r)$	=	stimulated emission rate (s^{-1})
$N_s(r, t)$	=	total number of stimulation emitted photons
$N_f(r, t)$	=	total number of fluorescent photons
η_{STED}	=	spatially varying STED probability
$h_{\text{fl,eff}}(r)$	=	effective fluorescent spot
h_{exc}	=	excitation probability
$k_{\text{STED}}^{\text{max}}$	=	peak STED depletion rate (s^{-1})
f_{rep}	=	repetition rate (s^{-1})
t_r	=	pulse spacing (s)
P_{avg}	=	average STED power (W)
P_{sat}	=	STED saturation power (W)
A	=	doughnut area (cm^2)
c	=	speed of light ($299.792.458 \text{ m}/\text{s}$)

Upconversion nanoparticles synthesis procedure

The synthesis and TEM characterization of the upconversion nanoparticles was performed at the Anorganische Chemie group at the University of Osnabrück:

prof. dr. Markus Haase
Athira N. Raj
Anorganische Chemie I
Universität Osnabrück
Barbarastraße 7
D-49069, Osnabrück
Germany

Preparation of $\text{NaYF}_4:\text{Yb}^{3+}, \text{Er}^{3+}$ Core particles

A hot injection method was adopted for the synthesis of the hexagonal $\text{NaYF}_4:\text{Yb}^{3+}, \text{Er}^{3+}$ (core) nanoparticles. The experimental set up consists of a three-neck round bottom vessel with attached thermo sensor, reflux condenser and heating mantle. In a typical synthesis, 40 ml of oleic acid and octadecene degassed at 100 °C under vacuum for 1 h with vigorous stirring. The above mixture was heated up to 320 °C under N₂ atmosphere. In a separate set up, 0.5 mmol of precursor particles dissolve in equal volume of oleic acid and octadecene (2.5 ml each) at 100 °C with stirring and then degas at 100 °C for 1 h. The dissolved cubic $\text{NaYF}_4:\text{Yb}^{3+}, \text{Er}^{3+}$ particles took in a Syringe and injected very fastly in to the 320 °C heated solvents. The reaction was continued for 15 min after it regained the temperature 320 °C. Afterwards the solution cooled down to room temperature, precipitated by the addition of equal volume of ethanol and collected by centrifugation.

Preparation of $\text{NaYF}_4:\text{Yb}^{3+}, \text{Er}^{3+}/\text{NaYF}_4$ (Core/Shell)

For the synthesis of core shell particles opt a single pot synthesis in which hot injection of precursor core particles followed by slow dropping of shell precursor particles. The experimental set up consists of a four-neck round bottom vessel with attached thermo sensor, Miethke-type dropping funnel, reflux condenser and heating mantle. In the first step of the core/shell synthesis, core particles were prepared at 320 °C as mentioned above but without isolating the particles from the solution. After 15

min at 320 °C, 1 mmol of NaYF₄ precursor particle in hexane were dropped slowly through the dropping funnel in to the solution containing core particle. After the complete addition of shell material the core/shell particles kept 10 min at 320 °C. The procedure as above was used the separation and purification of core shell particles.

TEM characterizations

Transmission electron microscopy (TEM) images were taken with a JEOL JEM 2100 transmission electron microscope using a LaB₆-Cathode and an acceleration voltage of 200 kV.

Appendix C

Additional figures

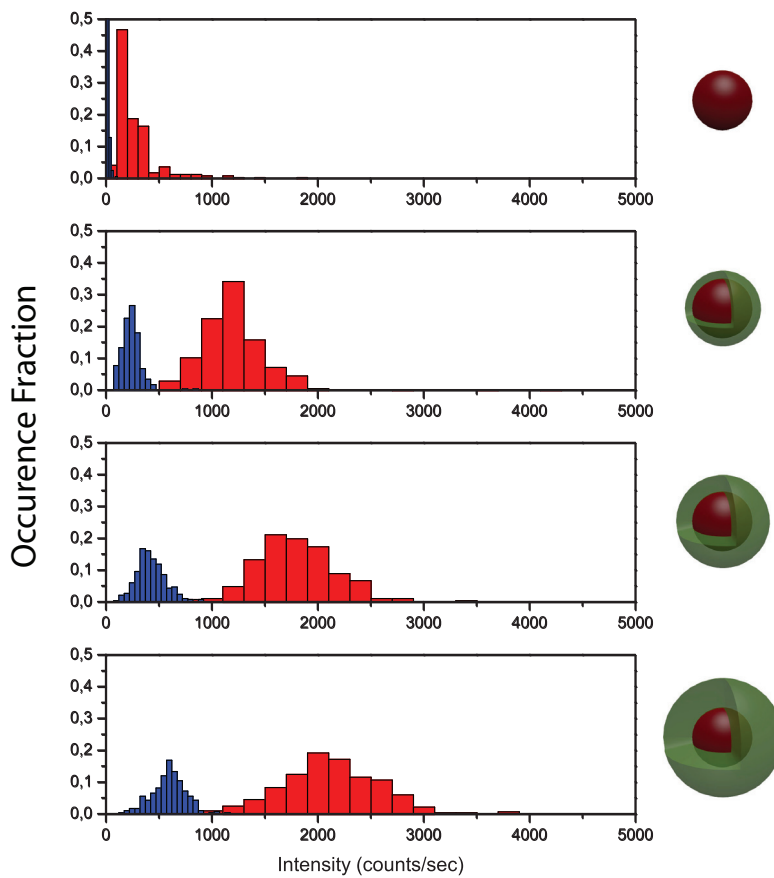


Figure C.1: Overlay representation of the brightness distributions for the different particles at power densities of $\sim 3.2 \times 10^5$ W/cm² (red) and $\sim 0.57 \times 10^5$ W/cm² (blue).

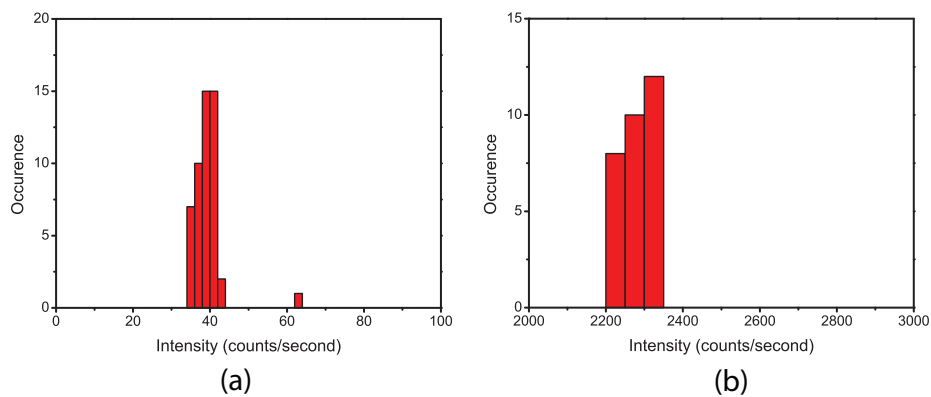


Figure C.2: (a) Background intensity histogram obtained from time traces at different positions on the coverslip where no particles were present. The histogram in (b) represents the accuracy of 'hitting' a single particle (ANR116) with our excitation focus. The excitation focus was moved away from the focus and then back to the center position of the same particle repeatedly to obtain single particle time traces from which an average intensity was obtained. All time traces were obtained at a power density of $\sim 3.2 \times 10^5 \text{ W/cm}^2$.

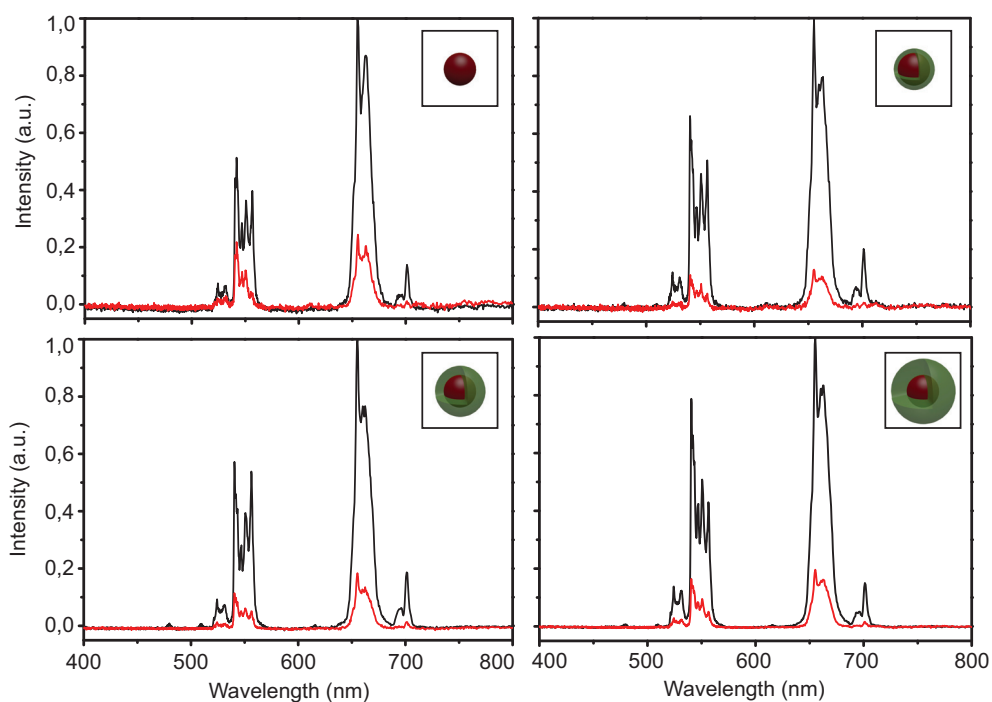


Figure C.3: Spectra obtained from high concentration samples at a power density of $\sim 3.2 \times 10^5 \text{ W/cm}^2$ (black) and $\sim 0.57 \times 10^5 \text{ W/cm}^2$ (red).

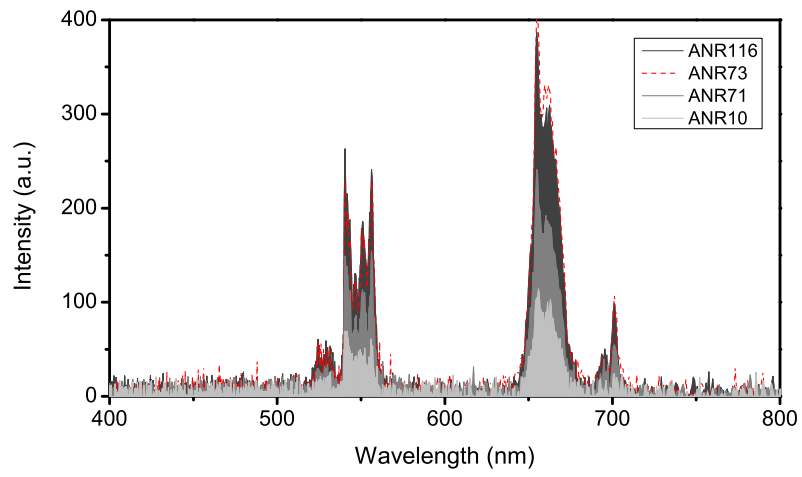


Figure C.4: Overlay representation of the average spectrum of single particles.

Appendix D

STED resolution

The increase in spatial resolution is dependent on the STED excitation intensity and can be described mathematically. Let $h_{\text{exc}}(r)$ be the normalized excitation probability in the focal plane resulting from the excitation pulse. After the passage of a STED pulse, the fluorescence probability $\eta(r)$ of a molecule has decayed to

$$\eta(r) = \exp[-\sigma t_s I_{\text{STED}}(r)], \quad (\text{D.1})$$

with σ , t_s and $I_{\text{STED}}(r)$ denoting the cross section for stimulated emission, STED pulse duration and the focal intensity of the STED pulse, respectively. Note that $I_{\text{STED}}(r)$ here is given by number of photons per unit area per unit time. As a result of the overlapping STED beam, the probability to detect a photon from location r is proportional to

$$h(r) = h_{\text{exc}}(r)\eta(r). \quad (\text{D.2})$$

Given a lens with semi aperture θ , we can describe the spatial excitation probability $h_{\text{exc}}(r)$ and the STED intensity $I_{\text{STED}}(r)$ by:

$$h_{\text{exc}}(r) = C \cos^2 \left(\frac{\pi r n \sin \theta}{\lambda_{\text{exc}}} \right) \quad (\text{D.3})$$

$$I_{\text{STED}}(r) = I_{\text{STED}}^{\text{max}} \sin^2 \left(\frac{\pi r n \sin \theta}{\lambda_{\text{STED}}} \right) \quad (\text{D.4})$$

Normalized cross sections of $h_{\text{exc}}(r)$ and $I_{\text{STED}}(r)$ are also illustrated in figure 8.7 (a) as the blue curve and yellow curve respectively. $I_{\text{STED}}^{\text{max}}$ is simply the maximum STED intensity in the doughnut shape. For further simplification we can define the constant ς as

$$\varsigma = \sigma t_s I_{\text{STED}}^{\text{max}} \quad (\text{D.5})$$

If we combine equations D.1, D.3, D.4 and D.5 with equation D.2, and use the approximation $\lambda_{\text{exc}} \approx \lambda_{\text{STED}} \equiv \lambda$, equation D.2 can be written as:

$$h(r) = C \cos^2 \left(\frac{\pi r n \sin \theta}{\lambda} \right) \exp \left[-\sigma \tau I_{\text{STED}}^{\text{max}} \sin^2 \left(\frac{\pi r n \sin \theta}{\lambda_{\text{STED}}} \right) \right] \quad (\text{D.6})$$

$$\approx C \cos^2 \left(\frac{\pi r n \sin \theta}{\lambda} \right) \exp \left[-\varsigma \sin^2 \left(\frac{\pi r n \sin \theta}{\lambda} \right) \right] \quad (\text{D.7})$$

$h(r)$ is the FWHM of the effective fluorescent spot, which cross section is also represented as the green curve in Figure 8.7 (b). We can further approximate equation D.6 with a Taylor series ($r < \lambda/2n \approx 0$) to the second order:

$$h(r) \approx 1 - \left(\frac{\pi n r \sin \theta}{\lambda} \right)^2 (\zeta + 1) \quad (\text{D.8})$$

At the FWHM we have $h(r) = 0.5$, so we can solve for r :

$$r = \pm \frac{\lambda \sqrt{1 - 0.5}}{\pi n \sin \theta \sqrt{\zeta + 1}} \quad (\text{D.9})$$

The FWHM $\Delta r = 2r$ can then be described with:

$$\Delta r = 2 \frac{\lambda \sqrt{0.5}}{\pi n \sin \theta \sqrt{\zeta + 1}} \approx \frac{0.45 \lambda}{n \sin \theta \sqrt{\zeta + 1}} = \frac{0.45 \lambda}{n \sin \theta \sqrt{\sigma t_s I_{\text{STED}}^{\text{max}} + 1}} \quad (\text{D.10})$$

From equation D.1 we can see that for $I_{\text{STED}} = 1/\sigma t_s = I_{\text{sat}}$ the fluorescence has dropped to $1/e$ of the initial value. By introducing I_{sat} in equation D.10 we obtain:

$$\Delta r = \frac{0.45 \lambda}{n \sin \theta \sqrt{I_{\text{STED}}^{\text{max}}/I_{\text{sat}} + 1}} \quad (\text{D.11})$$

Equation D.11 is the familiar inverse square root intensity law for STED: the FWHM resolution approximately scales with the inverse square root of the STED intensity.

Appendix E

Detailed overview of STED setup

	Description	Company	Part Number
1	Excitation laser	PicoQuant	LDH-P-C-485-C-485
2	Adjustable mirror holder	Fine-adjustment	Y03_122_6201
	High quality mirror	Qi-Optiq	G340783000
3	STED laser	MPBC	VFL-P1500-592
4	Fiber Launch with Microscope objective	Thorlabs Thorlabs	MBT613D/M 10X Olympus Plan Achromat Objective, 0.25 NA
5	XYZ Translation Stage	Thorlabs	PT3/M
6	Adjustable holder with fiber outcoupler	Fine-Adjustment Thorlabs	Y03_122_6201 SM1FC
7	Collimation objective	Olympus	4X Olympus Plan Achromat Objective, 0.10 NA
8	Excitation clean-up filter	Semrock	FF01-480/17-25
9	Gimbal mirror-mount High quality mirror	Thorlabs Qi-Optiq	GM100/M G340783000
10	Quartz half-wave plate for 589 nm	B. Halle	RZQ 2.15
11	STED clean-up filter	Semrock	FF01-591/6-25
12	Vortex phase-plate	RPC-Photonics	VPP-1a - 596.5 nm
13	XY-Stage	Standa	7T167-25XY, 2AB167-25
14	Beam-combining dichroic mirror	Chroma	ZT532rdc, $\lambda/10$ RWD
15	Microscope body	Custom built	
16	XYZ-piezo stage + stage controller	PI	P-733.3CL (stage), E-710.4CL (controller)
17	Dichroic mirror + Microscope objective	Chroma Nikon	zt488-491/594rdc, RWF of 0.08-0.17 peak-to-valley/inch 60X water-immersion, 1.2 NA
18	Achromat lens (50 mm)	Thorlabs	AC254-050-A-ML
19	Mounted Pinhole (15 μ m)	Thorlabs	P15S
20	XYZ-stage with differential micrometers	Thorlabs	PT3A/M
21	Multiple filters: 488 Notch, 594 Notch, 488 RazorEdge	Semrock	NF03-488E-25, NF03-594E-25, LP02-488RS-25
22	Flip-mount with mirror	Multiple	
23	Optical dichroic mirror for FCCS option		
24	Achromat lens (30 mm)	Thorlabs	AC254-030-A-ML
25	Single Photon Avalanche Diode (SPAD)	PicoQuant	MPD-5CTC SPAD
26	Achromat lens	Thorlabs	
27	Cage-plate with fiber-coupler	Thorlabs	SM1FC
28	Compact spectrometer	Thorlabs	CCS100
29	Hand-held controller for Picometer	Newport	8302 (picometer actuator), iPico 8763-kit, iPico 8757 (driver + hand terminal)
30	Multimode-fiber	Thorlabs	
31	High power polarization maintaining single-mode fiber	OZ-Optics	PMJ-3HPC-633-4/125-3AS-2-1-SP
32	Single mode fiber	Thorlabs	P1-560A-FC-2
33	two-axis high precision rotation mount	Thorlabs	PR01/M, CRM1P/M
	Quartz quarter-wave plate for 589 nm	B. Halle	RZQ 4.15
	Not shown in figure:		
	4-channel router	PicoQuant	PHR 800
	Time Correlated Single Photon Counting (TCSPC) module	PicoQuant	PicoHarp 300 with TTTR hardware mode option
	SymPhoTime software	PicoQuant	SymPhoTime

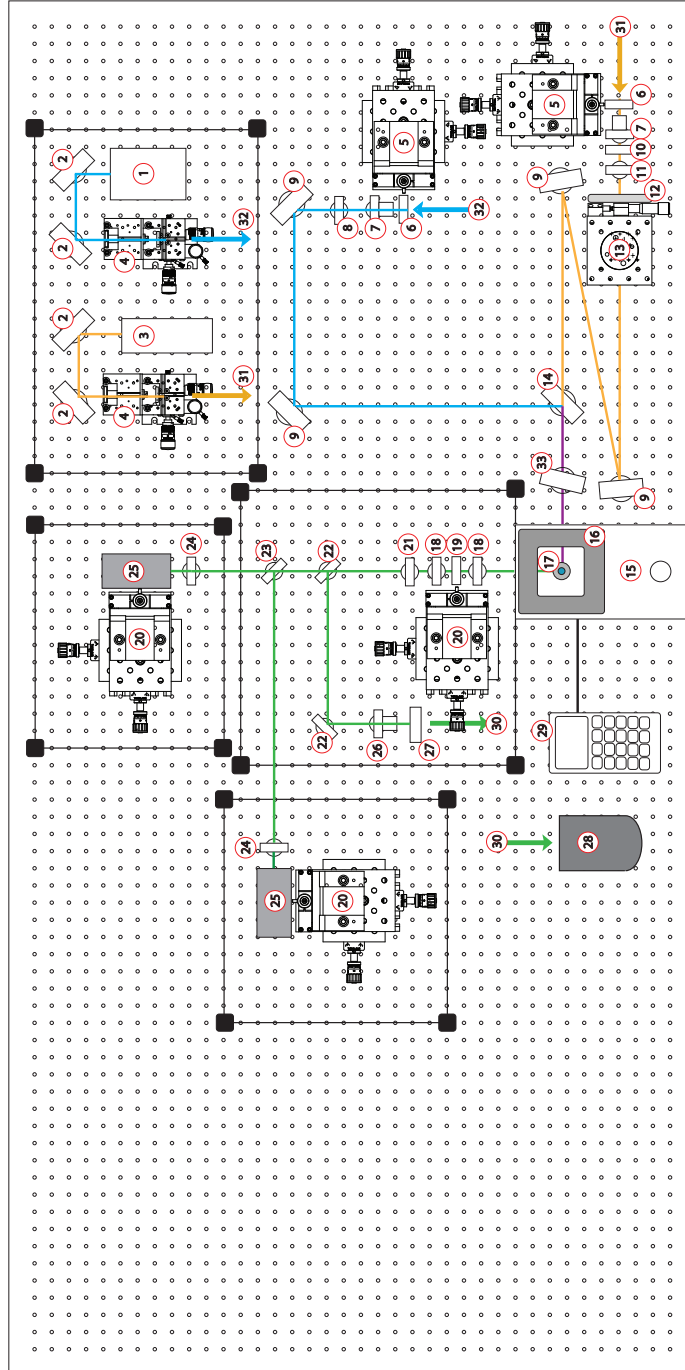


Figure E.1: Detailed overview of the setup. The arrows indicate fiber in/outcoupling. The table on the left page presents a detailed list of the numbered parts shown in this setup overview.

Appendix F

MATLAB code for focal spot simulation

These m-files (MATLAB) were created with help of the theoretical formulas given by Hao *et al.* [46]. The function vOut.m is called by the first m-file in the double integration step.

```
%close all
clear all
plane = 0; % XY-plane = 1, XZ-plane = 0
NA = 1.2/sqrt(2); % Numerical Aperture
n = 1.33; % Refractive index (water)

C = 1;
A1 = 1;
step = 10; % simulation step size
z2_max = 800; % size of z in simulated image (nm)
r2_max = 800; % size of radius r in simulated image (nm)

theta_max = asin(NA/n); % maximum opening angle of objective
z2_array = -z2_max:step:z2_max;
p2_array = 0:0.2:2*pi;

if plane == 1;
    r2_array = 0:step:r2_max;
else
    r2_array = -r2_max:step:r2_max;
end

tol = 1e-3; %integration tolerance

count = 0;
h = waitbar(0, 'Please Wait...');
%% ***** XY plane *****
if plane ==1;
    E_x = zeros(length(r2_array),length(p2_array));
    E_y = zeros(length(r2_array),length(p2_array));
    E_z = zeros(length(r2_array),length(p2_array));
    count_length = length(r2_array)*length(p2_array);
    for q = 1:length(p2_array);
        p2 = p2_array(q);
        for m = 1:length(r2_array);
            count = count+1;
            waitbar(count / count_length)
            r2 = r2_array(m);
            z2 = 0; % We want a XY cross-section at z=0
            %% Double integral calculation (calls on function vOut.m):
            E_x(m,q) = li*dblquad(@vOut,0,theta_max,0,2*pi,tol,[],z2,r2,p2,1);
            E_y(m,q) = li*dblquad(@vOut,0,theta_max,0,2*pi,tol,[],z2,r2,p2,2);
            E_z(m,q) = li*dblquad(@vOut,0,theta_max,0,2*pi,tol,[],z2,r2,p2,3);
        end
    end
end
close(h);

I = abs(E_x).^2+abs(E_y).^2+abs(E_z).^2; % Intensity profile

% for XY plane, the image is simulated as radius-vs-phi(angle), so we need
% to do a polar-to-cartesian transform on the image to obtain an XY image:
[N M] = size(I);
Z = 0;
L = length(r2_array);
X = (-L:1:L);
Y = (-L:1:L);
[X,Y] = meshgrid(X,Y);
[THETA,RHO] = cart2pol(Y,X);
THETA = (THETA)*(M-1)/(2*pi) + (M+1)/2;
new = interp2(I, THETA, RHO);
```

```

new(isnan(new)) = 0;
new(L+1,L+1) = I(1,1); % solution for singularity due to polar-cartesian transform

x = -r2_max:r2_max/(length(r2_array)):r2_max;
y = -r2_max:r2_max/(length(r2_array)):r2_max;
%%%%%%%%%%%%%%%%%%%%%%%%%%%%%%%%%%%%%%%%%%%%%%%%%%%%%%%%%%%%%%%%%%%%%%%%%
figure
    surface(y,x,new,'LineStyle','none');
    title('XY','FontSize',18);
    colormap hot
    set(gca,'XTick',-r2_max:r2_max/2:r2_max,'FontSize',14)
    set(gca,'YTick',-r2_max:r2_max/2:r2_max,'FontSize',14)
    axis square
    axis tight
    axis([-r2_max,r2_max,-r2_max,r2_max])
end;

%% %%%%%%%%%%%%%%%%%%%%%%%%%%%%%%%%%%%%%%%%%%%%%%%%%%%%%%%%%%%%%%%%%%%%%%%%% XZ/YZ plane %%%%%%%%%%%%%%%%%%%%%%%%%%%%%%%%%%%%%%%%%%%%%%%%%%%%%%%%%%%%%%%%%%%%%%%%%
if plane == 0
    EZ_x = zeros(length(z2_array),length(r2_array));
    EZ_y = zeros(length(z2_array),length(r2_array));
    EZ_z = zeros(length(z2_array),length(r2_array));
    count_length = length(r2_array)*length(z2_array);
    p2 = pi; % for XZ plane, use p2 = pi*3/2, for YZ plane, use p2 = pi
    for m = 1:length(r2_array);
        r2 = r2_array(m);
        for k = 1:length(z2_array);
            count = count+1;
            waitbar(count / count_length)
            z2 = z2_array(k);
            %% Double integral calculation (calls on function vOut.m):
            EZ_x(k,m) = 1i*dblquad(@vOut,0,theta_max,0,2*pi,tol,[],z2,r2,p2,1);
            EZ_y(k,m) = 1i*dblquad(@vOut,0,theta_max,0,2*pi,tol,[],z2,r2,p2,2);
            EZ_z(k,m) = 1i*dblquad(@vOut,0,theta_max,0,2*pi,tol,[],z2,r2,p2,3);
        end;
    end;
    close(h);
    IZ = abs(EZ_x).^2+abs(EZ_y).^2+abs(EZ_z).^2;
    [x,z] = meshgrid(r2_array,z2_array);
    %%%%%%%%%%%%%%%%%%%%%%%%%%%%%%%%%%%%%%%%%%%%%%%%%%%%%%%%%%%%%%%%%%%%%%%%%
    figure
    surface(x,z,IZ,'LineStyle','none');
    title('XZ','FontSize',18);
    colormap hot
    set(gca,'XTick',-r2_max:r2_max/2:r2_max,'FontSize',14)
    set(gca,'YTick',-z2_max:z2_max/2:z2_max,'FontSize',14)
    axis square
    axis tight
    axis([-r2_max,r2_max,-z2_max,z2_max])
end;

function f = vOut(t, phi, z2, r2, p2, v)
NA = 1.2; % Numerical Aperture of objective
n = 1.33; % Refractive index (water)
h_max = 5e6; % Max. height of incoming beam (radius of beam) here 5 mm
A1 = 0.8;
lambda = 592; % STED wavelength (nm)
theta_max = asin(NA/n); % maximum opening angle of objective
foc = h_max/sin(theta_max); % effective focal length of objective
k = (2*pi)/lambda;
a = sqrt(cos(t));
pol = 1/sqrt(2)*[1, 1i, 0]; % right-circular polarization
% pol = [0, 1, 0]; % linear-y polarization
% for other type of polarizations, see Hao et. al - effects of polarization
% on the de-excitation dark focal spot in STED (2010)
Vx = (1+(cos(t)-1)*cos(phi)^2)*pol(1) + ((cos(t)-1)*cos(phi)*sin(phi))*pol(2) - (sin(t)*cos(phi))*pol(3);
Vy = ((cos(t)-1)*cos(phi)*sin(phi))*pol(1) + (1+(cos(t)-1)*sin(phi)^2)*pol(2) - (sin(t)*sin(phi))*pol(3);
Vz = (sin(t)*cos(phi))*pol(1) + (sin(t)*sin(phi))*pol(2) + (cos(t))*pol(3);
R = h_max/sqrt(2);
f = 1;
xShift = 0; % phase plate shift in x-direction
yShift = 0; % phase plate shift in y-direction
h = foc*sin(t);
% For no phase plate, use:
% d_alpha = 0;
% For a vortex phase plate (no shift), use:
d_alpha = phi;
% For an annular phase plate, use:
% if abs(h)<R;
%     d_alpha = pi;
% else
%     d_alpha = 0;
% end;
% For a vortex phase plate d_alpha = phi = atan2(y,x). If the center of the vortex plate
% is shifted with respect to the beam center, the new coordinates where the light ray

```

```

% will hit the plate is xNew and yNew.
% xNew = -xShift - h*cos(phi);
% yNew = -yShift - h*sin(phi);
% alphaShift = atan2(yNew,xNew);
% d_alpha = alphaShift;
b = k*n*(z2*cos(t)+r2*sin(t)*cos(phi-p2));
switch v
case 1
    f = sin(t).*A1.*a.*Vx.*exp(1i*d_alpha).*exp(1i*b);
case 2
    f = sin(t).*A1.*a.*Vy.*exp(1i*d_alpha).*exp(1i*b);
case 3
    f = sin(t).*A1.*a.*Vz.*exp(1i*d_alpha).*exp(1i*b);
end;

```

Bibliography

- [1] Shuang Fang Lim, William S. Ryu, and Robert H. Austin. Particle size dependence of the dynamic photophysical properties of $\text{NaYF}_4\text{:Yb, Er}$ nanocrystals. *Opt. Express*, 18(3):2309–2316, Feb 2010.
- [2] Shiwei Wu, Gang Han, Delia J. Milliron, Shaul Aloni, Virginia Altoe, Dmitri V. Talapin, Bruce E. Cohen, and P. James Schuck. Non-blinking and photostable upconverted luminescence from single lanthanide-doped nanocrystals. *Proceedings of the National Academy of Sciences*, 106(27):10917–10921, July 2009.
- [3] Yu Wang, Langping Tu, Junwei Zhao, Yajuan Sun, Xianggui Kong, and Hong Zhang. Upconversion luminescence of $\beta\text{-NaYF}_4\text{: Yb}^{3+}, \text{Er}^{3+}$ core/shell nanoparticles: Excitation power density and surface dependence. *The Journal of Physical Chemistry C*, 113(17):7164–7169, 2009.
- [4] Markus Haase and Helmut Schäfer. Upconverting nanoparticles. *Angewandte Chemie International Edition*, 50(26):5808–5829, 2011.
- [5] Li Peng Qian, Du Yuan, Guang Shun Yi, and Gan Moog Chow. Critical shell thickness and emission enhancement of $\text{NaYF}_4\text{:Yb,Er}/\text{NaYF}_4/\text{silica}$ core/shell/shell nanoparticles. *Journal of Materials Research*, 24(12):3559–3568, 2009.
- [6] Feng Wang, Juan Wang, and Xiaogang Liu. Direct evidence of a surface quenching effect on size-dependent luminescence of upconversion nanoparticles. *Angewandte Chemie International Edition*, 49(41):7456–7460, 2010.
- [7] Feng Wang, Renren Deng, Juan Wang, Qingxiao Wang, Yu Han, Haomiao Zhu, Xueyuan Chen, and Xiaogang Liu. Tuning upconversion through energy migration in core–shell nanoparticles. *Nat Mater*, advance online publication, October 2011.
- [8] Cuikun Lin, Mary T. Berry, Robert Anderson, Steve Smith, and P. Stanley May. Highly luminescent nir-to-visible upconversion thin films and monoliths requiring no high-temperature treatment. *Chemistry of Materials*, 21(14):3406–3413, 2009.
- [9] A Bednarkiewicz, D Wawrzynczyk, A Gagor, L Kepinski, M Kurnatowska, L Krajczyk, M Nyk, M Samoc, and W Strek. Giant enhancement of upconversion in ultra-small $\text{Er}^{3+}/\text{Yb}^{3+}\text{:NaYF}_4$ nanoparticles via laser annealing. *Nanotechnology*, 23(14):145705, 2012.
- [10] Feng Wang and Xiaogang Liu. Recent advances in the chemistry of lanthanide-doped upconversion nanocrystals. *Chem. Soc. Rev.*, 38:976–989, 2009.

- [11] Helmut Schäfer, Pavel Ptacek, Henning Eickmeier, and Markus Haase. Synthesis of hexagonal $\text{Yb}^{3+}, \text{Er}^{3+}$ -doped NaYF_4 nanocrystals at low temperature. *Advanced Functional Materials*, 19(19):3091–3097, 2009.
- [12] M. Pollnau, D. R. Gamelin, S. R. Lüthi, H. U. Güdel, and M. P. Hehlen. Power dependence of upconversion luminescence in lanthanide and transition-metal-ion systems. *Phys. Rev. B*, 61:3337–3346, Feb 2000.
- [13] J. F. Suyver, A. Aebischer, S. Garcia-Revilla, P. Gerner, and H. U. Güdel. Anomalous power dependence of sensitized upconversion luminescence. *Phys. Rev. B*, 71:125123, Mar 2005.
- [14] Laura Martinez Maestro, Emma Martín Rodríguez, Fiorenzo Vetrone, Rafik Nacache, Hector Loro Ramirez, Daniel Jaque, John A. Capobianco, and José García Solé. Nanoparticles for highly efficient multiphoton fluorescence bioimaging. *Opt. Express*, 18(23):23544–23553, Nov 2010.
- [15] Guang-Shun Yi and Gan-Moog Chow. Water-soluble $\text{NaYF}_4:\text{Yb}, \text{Er}(\text{Tm})/\text{NaYF}_4/\text{polymer}$ core/shell/shell nanoparticles with significant enhancement of upconversion fluorescence. *Chemistry of Materials*, 19(3):341–343, 2007.
- [16] Rajesh Kombar, Johann P. Klare, Benjamin Voss, Jörg Nordmann, Heinz-Jürgen Steinhoff, and Markus Haase. An electron paramagnetic resonance spectroscopic investigation on the growth mechanism of $\text{NaYF}_4:\text{Gd}$ nanocrystals. *Angewandte Chemie International Edition*, 51(26):6506–6510, 2012.
- [17] N.J.J. Johnson, A. Korinek, C. Dong, and F.C.J.M. van Veggel. Self-focusing by ostwald ripening: A strategy for layer-by-layer epitaxial growth on upconverting nanocrystals. *J Am Chem Soc*, 2012.
- [18] Stefan Schietinger, Leonardo de S Menezes, Bjorn Lauritzen, and Oliver Benson. Observation of size dependence in multicolor upconversion in single $\text{Yb}^{3+}, \text{Er}^{3+}$ codoped NaYF_4 nanocrystals. *Nano Lett*, 9(6):2477–81, 2009.
- [19] J. de Wild, J.K. Rath, A. Meijerink, W.G.J.H.M. van Sark, and R.E.I. Schropp. Enhanced near-infrared response of a-Si:H solar cells with $\beta\text{-NaYF}_4:\text{Yb}^{3+}$ (18%), Er^{3+} (2%) upconversion phosphors. *Solar Energy Materials and Solar Cells*, 94(12):2395 – 2398, 2010.
- [20] Christian F. Gainer, Gihan S. Joshua, Channa R. De Silva, and Marek Romanowski. Control of green and red upconversion in $\text{NaYF}_4:\text{Yb}^{3+}, \text{Er}^{3+}$ nanoparticles by excitation modulation. *J. Mater. Chem.*, 21:18530–18533, 2011.
- [21] Ruoxue. Yan and Yadong. Li. Down/up conversion in Ln^{3+} -doped YF_3 nanocrystals. *Advanced Functional Materials*, 15(5):763–770, 2005.
- [22] Jia Liu, Xiaomin Liu, Xiangui Kong, and Hong Zhang. Controlled synthesis, formation mechanism and upconversion luminescence of $\text{NaYF}_4:\text{Yb}, \text{Er}$ nano/submicrocrystals via ionothermal approach. *Journal of Solid State Chemistry*, 190(0):98 – 103, 2012.
- [23] Darayas N. Patel, Lauren A. Hardy, Tabatha J. Smith, Eva S. Smith, Donald M. Wright III, and Sergey Sarkisov. Novel laser nanomaterials based on rare-earth compounds. *Journal of Luminescence*, (0):–, 2011.

- [24] A. H. Li and Q. Lü. Power-dependent upconversion luminescence intensity in NaYF_4 , Yb^{3+} , Er^{3+} nanoparticles. *EPL (Europhysics Letters)*, 96(1):18001, 2011.
- [25] S. Heer, K. Kömpe, H.-U. Güdel, and M. Haase. Highly efficient multicolour up-conversion emission in transparent colloids of lanthanide-doped NaYF_4 nanocrystals. *Advanced Materials*, 16(23-24):2102–2105, 2004.
- [26] G.S. Yi and G.M. Chow. Synthesis of hexagonal-phase NaYF_4 :Yb,Er and NaYF_4 :Yb,Tm nanocrystals with efficient up-conversion fluorescence. *Advanced Functional Materials*, 16(18):2324–2329, 2006.
- [27] E. Abbe. Beiträge zur theorie des mikroskops und der mikroskopischen wahrnehmung. *Archiv für Mikroskopische Anatomie*, 9:413–418, 1873. 10.1007/BF02956173.
- [28] Anedore Punge, Silvio O. Rizzoli, Reinhard Jahn, Jan D. Wildanger, Lars Meyer, Andreas Schönle, Lars Kastrop, and Stefan W. Hell. 3D reconstruction of high-resolution STED microscope images. *Microsc. Res. Tech.*, 71(9):644–650, May 2008.
- [29] Katrin I. Willig, Silvio O. Rizzoli, Volker Westphal, Reinhard Jahn, and Stefan W. Hell. STED microscopy reveals that synaptotagmin remains clustered after synaptic vesicle exocytosis. *Nature*, 440(7086):935–939, April 2006.
- [30] Samuel T. Hess, Thanu P. K. Girirajan, and Michael D. Mason. Ultra-High Resolution Imaging by Fluorescence Photoactivation Localization Microscopy. *Biophysical Journal*, 91(11):4258–4272, 2006.
- [31] Michael J. Rust, Mark Bates, and Xiaowei Zhuang. Sub-diffraction-limit imaging by stochastic optical reconstruction microscopy (STORM). *Nature Methods*, 3(10):793–796, August 2006.
- [32] U. Dürig, D. W. Pohl, and F. Rohner. Near-field optical-scanning microscopy. *Journal of Applied Physics*, 59(10):3318–3327, 1986.
- [33] S. W. Hell, M. Schrader, and H. T. M. van der Voort. Far-field fluorescence microscopy with three-dimensional resolution in the 100-nm range. *Journal of Microscopy*, 187(1):1–7, 1997.
- [34] Stefan W. Hell and Jan Wichmann. Breaking the diffraction resolution limit by stimulated emission: stimulated-emission-depletion fluorescence microscopy. *Opt. Lett.*, 19(11):780–782, Jun 1994.
- [35] Mats G. L. Gustafsson. Nonlinear structured-illumination microscopy: Wide-field fluorescence imaging with theoretically unlimited resolution. *Proceedings of the National Academy of Sciences of the United States of America*, 102(37):13081–13086, September 2005.
- [36] Thomas A. Klar and Stefan W. Hell. Subdiffraction resolution in far-field fluorescence microscopy. *Opt. Lett.*, 24(14):954–956, Jul 1999.

- [37] G. Donnert, J. Keller, R. Medda, M. A. Andrei, S. O. Rizzoli, R. Lührmann, R. Jahn, C. Eggeling, and S. W. Hell. Macromolecular-scale resolution in biological fluorescence microscopy. *Proceedings of the National Academy of Sciences of the United States of America*, 103(31):11440–11445, August 2006.
- [38] Katrin I. Willig, Lars Kastrop, U. Valentin Nägerl, and Stefan W. Hell. STED microscopy: Different approaches and applications. Unpublished, 2009.
- [39] Eva Rittweger, Kyu Young Han, Scott E. Irvine, Christian Eggeling, and Stefan W. Hell. STED microscopy reveals crystal colour centres with nanometric resolution. *Nat Photon*, 3(3):144–147, 2009.
- [40] Katrin I. Willig, Benjamin Harke, Rebecca Medda, and Stefan W. Hell. STED microscopy with continuous wave beams. *Nature Methods*, 4(11):915–918, October 2007.
- [41] Gael Moneron, Rebecca Medda, Birka Hein, Arnold Giske, Volker Westphal, and Stefan W. Hell. Fast STED microscopy with continuous wave fiber lasers. *Opt. Express*, 18(2):1302–1309, Jan 2010.
- [42] Christian Eggeling, Christian Ringemann, Rebecca Medda, Gunter Schwarzmann, Konrad Sandhoff, Svetlana Polyakova, Vladimir N. Belov, Birka Hein, Claas von Middendorff, Andreas Schönle, and Stefan W. Hell. Direct observation of the nanoscale dynamics of membrane lipids in a living cell. *Nature*, 457(7233):1159–1162, December 2008.
- [43] A. Einstein. Zur Quantentheorie der Strahlung. *Physikalische Zeitschrift*, 18:121+, 1917.
- [44] Thomas A. Klar, Stefan Jakobs, Marcus Dyba, Alexander Egner, and Stefan W. Hell. Fluorescence microscopy with diffraction resolution barrier broken by stimulated emission. *Proceedings of the National Academy of Sciences*, 97(15):8206–8210, July 2000.
- [45] Matthias Reuss. *Simpler STED setups*. PhD thesis, Combined Faculties for the Natural Sciences and for Mathematics of the Ruperto-Carola University of Heidelberg, Germany, December 2010.
- [46] Xiang Hao, Cuifang Kuang, Tingting Wang, and Xu Liu. Effects of polarization on the de-excitation dark focal spot in STED microscopy. *Journal of Optics*, 12(11):115707, 2010.
- [47] P. Török and P. Munro. The use of Gauss-Laguerre vector beams in STED microscopy. *Opt. Express*, 12(15):3605–3617, Jul 2004.
- [48] D. Wildanger, R. Medda, L. Kastrop, and S.W. Hell. A compact STED microscope providing 3D nanoscale resolution. *Journal of Microscopy*, 236(1):35–43, 2009.
- [49] Matthias Reuss, Johann Engelhardt, and Stefan W. Hell. Birefringent device converts a standard scanning microscope into a STED microscope that also maps molecular orientation. *Opt. Express*, 18(2):1049–1058, Jan 2010.

- [50] Chris J. Lee and Klaus J. Boller. The noise-limited-resolution for stimulated emission depletion microscopy of diffusing particles. *Opt. Express*, 20(12):12793–12798, Jun 2012.
- [51] Giuseppe Vicidomini, Gael Moneron, Kyu Y. Han, Volker Westphal, Haisen Ta, Matthias Reuss, Johann Engelhardt, Christian Eggeling, and Stefan W. Hell. Sharper low-power STED nanoscopy by time gating. *Nat Meth*, 8(7):571–573, July 2011.
- [52] Jeffrey R. Moffitt, Christian Osseforth, and Jens Michaelis. Time-gating improves the spatial resolution of STED microscopy. *Opt. Express*, 19(5):4242–4254, February 2011.